



UiO : **University of Oslo**

MSC THESIS

PLASMA AND SPACE PHYSICS

RPC-LAP Electric Field Signatures at the Diamagnetic Cavity of Comet 67P/Churyumov-Gerasimenko



Author:

Birgitte Madsen

Supervisors:

Cyril Simon Wedlund

Wojciech J. Miloch

May 2017



UiO : University of Oslo

Department of Physics

University of Oslo

Sem Sælands vei 24

0371 Oslo, Norway

+47 22 85 64 28

<http://www.mn.uio.no/fysikk/english/>

Abstract:

Degree:

MSc Thesis
Plasma and Space Physics
University of Oslo
Norway

Completed:

May 29, 2017

Author:

Birgitte Madsen

Supervisors:

Cyril Simon Wedlund
Wojciech J. Miloch

Page count: 121

Appendices: 6

In the comet - solar wind interaction region, the region closest to the comet is the diamagnetic cavity into which the solar wind cannot penetrate. The Rosetta mission to comet 67P/ChuryumovGerasimenko has provided diamagnetic cavity observations more than 600 times. This work presents the first study of the electric field signatures of three of these crossings on May 28, 2015 (M15) and February 17, 2016 (F16). The electric field is estimated from the probe potentials of the Langmuir probes (LAP) instrument of the Rosetta Plasma Consortium (RPC). By qualitatively relating the LAP findings to the observations by the RPC magnetometer (MAG) instrument, it is found that the electric field fluctuation level follows the magnetic field magnitude well throughout the studied events. Inside the M15 cavity, the LAP electric field estimate picks up puzzling time-localized low-frequency electric field wave signatures at 3.5 and 8 Hz. These are suggested to be related to waves in the lower hybrid frequency range in the plasma surrounding the cavity. The LAP potentials, additionally, give information about the spacecraft potential, that can be related to plasma electron density and temperature. Through a comparative study of the LAP probe potentials with the electron density estimate of the RPC Mutual Impedance Probe (MIP) instrument, it is found that the outbound boundary of the F16 cavities are characterized by increased electron density and, possibly, electron heating.



ACKNOWLEDGEMENTS

This work was carried out in the time period from March 2016 to May 2017 in the 4DSpace group at UiO under supervision of Wojciech J. Miloch and Cyril Simon Wedlund. I am forever thankful to my supervisors for their valuable support and encouragement. I truly treasure their effort to obtaining financial support for travels and inspiration to join collaborative meetings. A special thanks to Arne Pedersen for sharing his immense knowledge on Langmuir probing and the workings of the LAP instrument. Moreover, I would like to thank Andres Spicher, who devoted his precious time to share priceless insight into the Fourier and Morlet wavelet analysis methods.

I am thankful to the staff of the plasma and space physics group, and I would especially like to express my sincere gratitude to Bjørn Lybekk for always bringing a good mood, even though, I might have required translations of words once in a while. I would also like to thank my study colleague Sigve Harang for discussions on thesis-relevant problems and exemplifying that I was not the only one working weekends and holidays.

To my family and friends in Denmark, I am eternally grateful for your support, enthusiasm, and understanding when I have been too focussed on my thesis to give you the attention you deserve. I cannot wait to spend more time with you in the future. Moreover, thanks to my friend Kine Hanssen for our weekly morning and afternoon coffee breaks, without which my body would have craved for caffeine and laughter. And to my international and world-exploring friends, thank you for inspiring me to go abroad and pursue a Master's degree in plasma and space physics at UiO. This experience is something I will treasure forever.

Acknowledgements to science teams

Without the help of the RPC and ROSINA-COPS teams, this work would not have been possible. I would like to express a special thanks to the entire LAP team, of which Dr. Anders Eriksson (IRFU, Uppsala, Sweden) is principal investigator, for providing exemplified electric field estimates, and for discussions on the physical understanding of signatures in the estimates obtained by the LAP instrument. Additionally, I would like to thank Prof. Tomas Karlsson (KTH, Stockholm, Sweden) of the LAP team for providing data from his recent paper for the validation of my methods. The 4DSpace group at UiO has access to the LAP database through co-investigatorship, and I acknowledge Dr. Bjørn Lybekk (UiO, Oslo, Norway) for arranging the local LAP archive.

Moreover, thanks to Prof. Karl-Heinz Glassmeier, Dr. Ingo Richter and Charlotte Götz (TU Braunschweig, Germany) of the MAG team for kindly providing temperature-corrected magnetic field data, and to float the idea of possible interference from the spacecraft reaction wheels in the electric field data.

The presented MIP electron densities are made available by Dr. Pierre Henri (LPC2E, Orléans, France) of the MIP team, and the ICA data is provided and analysed by Dr. Hans Nilsson (IRF, Kiruna, Sweden) and Dr. Herbert Gunell (BIRA-IASB, Brussels, Belgium).

I would like also to acknowledge Prof. James L. Burch, Dr. Kathleen Mandt, and Dr. Thomas Broiles (SwRI, San Antonio, USA) from the IES team, and Prof. Kathrin Altwegg (Universität Bern, Switzerland) of the ROSINA-COPS team for providing IES and ROSINA-COPS data for my thesis.

This work makes use of Quicklook dataplots, the AMDA science analysis system provided by the Centre de Données de la Physique des Plasmas (CDPP) supported by CNRS (CNES, Observatoire de Paris and Université Paul Sabatier, Toulouse), and the European Space Agency's Planetary Science Archive (PSA, <https://archives.esac.esa.int/psa/>), where data obtained from the plasma and field instruments of the RPC is now available.



LIST OF ABBREVIATIONS

Abbreviation	Description
--------------	-------------

AMPTE	Active Magnetospheric Particle Tracer Explorers
BS	Bow Shock
CIV	Critical ionization velocity
CP	Cometopause
CS	Contact Surface
CSEQ	Comet-centered Solar Equatorial
DCBL	Diamagnetic Cavity Boundary Layer
ICA	Ion Composition Analyser
IES	Ion and Electron Sensor
IP	Ion Pile-up
LAP	Langmuir Probes
LH(F)	Lower Hybrid (Frequency)
MAG	Magnetometer
MB	Mystery Boundary
MIP	Mutual Impedance Probe
MHD	Magnetohydrodynamics
MP	Magnetic Pile-up
MVA	Minimum Variance Analysis
PSA	Planetary Science Archive
PSD	Power Spectral Density
RPC	Rosetta Plasma Consortium
RPC0	RPC electronics box

SAA	Solar Aspect Angle
s/c	Spacecraft
SSP	Surface Science Package
SW	Solar Wind
1P/H	1P/Halley
19P/B	19P/Borrelly
21P/G-Z	21P/Giacobini–Zinner
26P/G-S	26P/Grigg–Skjellerup
67P	67P/Churyumov–Gerasimenko

LIST OF SYMBOLS

Symbol	Description	Unit
a	Probe radius	m
amu	Atomic mass unit	1.661×10^{-27} kg
$A_e, A_i, A_{s/c}$	Surface area (spherical probe, flow direction, spacecraft)	m ²
\mathbf{B}, B	Magnetic field (vector, strength)	T
c_s	Sound speed	m/s
C_K	Kolmogorov constant	arb. unit
d_h	Heliocentric distance	AU
d_{12}	Probe separation distance	m
e	Elementary charge	1.602×10^{-19} C
\mathbf{E}, E	Electric field (3D and 1D)	Vm ⁻¹
E_{ph}, E_i	Energy (photon, drifting ions)	J
E_{ionize}	Ionization energy	J
$E(k)$	Energy spectrum	Jm
$f_s, f_C, f_p, f_{LH}, f_{ph}$	Frequency (sampling, gyro, plasma, lower hybrid photon)	Hz
I, I_p, I_{ph}, I_i, I_e	Current (probe, photoemission, ion, electron)	A
I_{i0}, I_{e0}, I_{ph0}	Saturation current (ion, electron, photoemission)	A
I_0	Ionization frequency at 1 AU	10^{-6} s ⁻¹
\mathbf{J}	Current density	Am ⁻²
k, k_I, k_D	Wavenumber (injection, dissipation)	m ⁻¹
k_B	Boltzmann's constant	1.38×10^{-23} m ² kg s ⁻² K ⁻¹
k_{in}	Ion-neutral collision frequency	m ³ s ⁻¹
L_i	Ion loss due to recombination	s ⁻¹ m ⁻³

m, m_i	Mass (ion)		kg
m_e	Electron mass	9.109×10^{-31}	kg
M	Mach number		unitless
\mathbf{n}	Boundary normal vector		unitless
n_e, n_i, n_n	Number density (electrons, ions, neutrals)		m^{-3}
p	Pressure		Pa
P	Power		arb. unit
q	Electrical charge		C
Q, Q_0	Outgassing rate and constant		s^{-1}
r, r_{bs}, r_{cs}	Radial and stand-off distance (bow shock, contact surface)		m
r_L	Larmor radius		m
Re	Reynolds number		unitless
R^2	Coefficient of determination		unitless
S_i	Ion creation due to ionization		$\text{s}^{-1}\text{m}^{-3}$
S_u	Power spectral density		arb. unit
T	Period		s
T_e, T_{ph}	Temperature (electron, thermal)		K
\mathbf{u}, \mathbf{u}_d	Velocity, drift velocity		m/s
u_n, u_{th}, u_d	Speed (neutrals, thermal, drift)		m/s
u_c	Critical ionization velocity		m/s
V	Electric potential		V
$V_p, V_1, V_2, V_f, V_s, V_{s/c}$	Potential (probes, floating, plasma/space, spacecraft)		V
W_{loss}	Windowing power loss		unitless
Z	Mutual impedance		Ω
α	Power-law exponent		unitless
γ	Recombination reaction rate	$1.21 \times 10^{-5} / \sqrt{T_e}$	cm^3s^{-1}
ε	Energy transfer rate		J/s
ε_0	Vacuum permittivity	8.854×10^{-12}	Fm^{-1}
λ	Lagrange multiplier		unitless
λ_D	Debye length		m
μ_0	Vacuum permeability	$4\pi \times 10^{-7}$	NA^{-2}
ν	Kinematic viscosity		m^2s^{-1}
ν_d	Photodestruction rate		s^{-1}
ν_{in}	Ion - neutral momentum transfer collision frequency		s^{-1}

ω_p	Angular plasma frequency	rad^{-1}
ω_0	Morlet wavelet frequency	Hz
Ω_L	Lower hybrid frequency	rad^{-1}
Ω_o	Oblique Langmuir wave frequency	rad^{-1}
$\Omega, \Omega_{ci}, \Omega_{ce}$	Angular gyrofrequency (ion. electron)	rad^{-1}
ρ	Mass density	kg m^{-3}
ρ_e	Charge density	C m^{-3}
σ	Standard deviation	arb. unit
σ_E	Electrical conductivity	S m^{-1}
τ	Eddy lifetime	s
ψ_0, ψ_{sn}	Morlet wavelet (mother and daughter)	unitless

TABLE OF CONTENTS

Chapter 1	Introduction	1
Chapter 2	The comet - solar wind interaction region	3
2.1	Principles of cometary plasma physics	3
2.2	Generation of cometary boundaries	8
2.3	Earth-based observations	9
2.4	Cometary boundaries based on in-situ studies	11
2.4.1	Bow shock (BS)	12
2.4.2	Cometosheath (CS)	13
2.4.3	Diamagnetic cavity (DC)	15
2.5	Observed wave-activity during in-situ measurements	18
2.5.1	Low-frequency waves caused by gyration of ions	19
2.5.2	Lower hybrid (LH) waves in the inner coma	20
2.6	Plasma turbulence	22
2.6.1	Kolmogorov turbulence	23
2.7	Summary of signatures in the cometary environment	25
Chapter 3	Instrumentation and data Processing	27
3.1	Spacecraft sheath	28
3.2	Instruments description	30
3.2.1	Coordinate systems	31
3.2.2	Langmuir Probes (LAP)	31
3.2.3	Fluxgate Magnetometer (MAG)	39
3.2.4	Supporting instruments: ICA, IES, MIP and ROSINA-COPS	43
3.3	Power spectrum	44
3.3.1	The Fourier method	45
3.3.2	Morlet wavelet analysis	52
3.3.3	Reproduction of electric field signatures observed in the vicinity of comet 67P . .	55
3.4	Summary of the electric and magnetic field data analysis methods	57
Chapter 4	Results and discussion	59
4.1	Event characteristics	59

4.1.1	Event parameters	61
4.1.2	Orientation of the diamagnetic cavity boundary layers (DCBL)	62
4.1.3	The plasma environment	64
4.1.4	Electric field signatures	67
4.2	Spectral signatures of the electric and magnetic fields	72
4.2.1	Turbulent-like behaviour of the electric and magnetic fields	79
4.2.2	Low-frequency wave peaks	83
4.3	Summary of the cavity signatures	87
Chapter 5	Conclusion and perspectives	89
	Bibliography	93
Appendix A	MATLAB scripts	103
Appendix B	Probe calibration	111
Appendix C	IES ion and electron energy spectrograms	113
Appendix D	Defining cavity boundaries from electric field estimates	115
Appendix E	Zoom-ins on Cavities	117
Appendix F	Horizontal line signatures	119

INTRODUCTION

In the solar system, comets orbit the Sun in highly eccentric elliptical trajectories, as illustrated in Figure 1.1. This leads to a greatly varying cometocentric solar distance. Solar radiation and the solar wind constituents interact with the cometary neutrals and ions, causing, e.g., the comet tails that might be periodically visible from Earth. The activity level of the comet depends on the composition of the comet, its surface heating caused by solar irradiation, and the conditions of the solar wind plasma and associated electromagnetic fields. Since the solar radiation flux, the interplanetary magnetic field magnitude, and the plasma density of the solar wind reduce with radial distance from the Sun, the comet undergoes several stages of activity during its orbit. Perihelion marks the closest approach to the Sun, and it is hence at about this point that the comet is the most active.

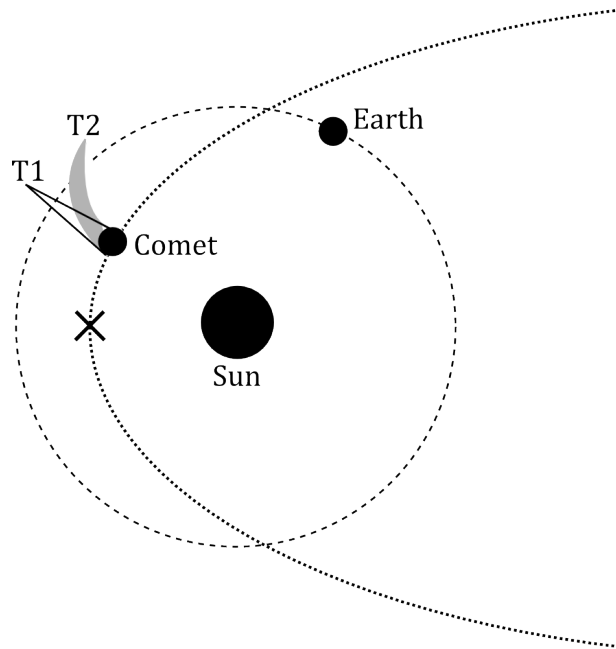


Figure 1.1. Simple illustration of the Sun - Earth - comet system projected into the orbital plane of the Earth. The dashed line indicates the orbit of the Earth, whilst the dotted line is the elongated elliptical orbit of the comet, with the cross marking perihelion. The plasma tail (T1) of the comet points radially away from the Sun, whilst the dust tail (T2) is more diffuse and bends slightly towards the Sun. Illustration is not to scale.

At aphelion the comet is its farthest from the Sun and is, hence, in its quietest phase. As the comet approaches the Sun, solar illumination sublimates ice (mainly H_2O , CO , and CO_2) from the comet surface layers, making the comet outgas neutrals that are affected by only a weak gravitational force (Nilsson et al., 2015a). The cometary neutrals move radially away from the nucleus with speeds of about 1 km/s (Cravens, 1987) and mix undisturbedly with the solar wind until being ionized. The newly ionized cometary species interact with the solar wind (composed of mostly H^+ and He^{2+} ions). This interaction generates the plasma tail on the comet nightside, and cometary boundaries that mark the transition between plasma regions of different compositions and characteristics in the environment surrounding the comet.

The comet in Figure 1.1 is depicted with its dust and plasma tails that may extend millions of kilometres from the comet nucleus (Coates and Jones, 2009). The plasma tail is directed radially away from the Sun, whilst the dust tail is more diffuse and bends towards the Sun such that there is an angular difference between the pointing directions of the two tails. This is due to the fact that the plasma tail direction is determined by the solar wind flow, whilst the dust tail direction is the result of photon pressure and weak solar gravitational pull on the dust particles (Schmude, 2010).

In the middle of the 20th century, it was the pointing direction of the comet tails that made Ludwig Biermann and Hannes Alfvén conclude for the existence of the solar wind and its intrinsic magnetic field (Ip, 2004). However, even though the comet - solar wind interaction has played a key role in the understanding of the solar wind, only little is known about the plasma environment on the dayside of the comet nucleus. Only few spacecraft flybys of comets have provided in-situ plasma and electromagnetic field measurements of this region. The knowledge of the dayside plasma environment of comets has recently been greatly enhanced by the European Space Agency Rosetta mission to comet 67P/Churyumov-Gerasimenko (67P). The spacecraft started orbiting the comet in August, 2014, and was crash-landed on the comet surface on September 30, 2016 (Dickeli, 2016, 2016). Hence, the mission has supplied 2 years of nearly continuous plasma and field measurements with the Rosetta Plasma Consortium instruments (RPC), as the evolutionary state of the plasma environment around comet 67P changed (Carr et al., 2007). The RPC findings supplement the pre-Rosetta cometary flyby observations and has brought new information about the evolution of the cometary plasma environment.

Several comet - solar wind interaction-induced boundary crossings have been mapped by instruments of the RPC (see Mandt et al. (2016), Goetz et al. (2016b)). However, only few studies on the electric field estimated by the Langmuir probes of the RPC have been carried out (see Karlsson et al. (2017)), and none of these focus on boundary crossings near the comet. This study is the first work on the LAP electric field signatures during crossings of the innermost cometary region, the *diamagnetic cavity*, that is characterized by a depletion of the solar wind and its associated magnetic field.

The first part of this report provides an introduction to basic plasma physical principles, followed by a review of the current understanding of the plasma environment caused by the interaction between the comet and the solar wind. Chapter 3 describes and discusses the RPC instruments and the method used for the data analysis of Chapter 4. The MATLAB scripts implemented for the data analysis can be found in Appendix A. In the data analysis the electric fingerprints of the studied cavity crossings are unravelled and related to observations by other instruments aboard the Rosetta spacecraft. The main aim is to investigate whether the electric field supports other RPC instrument findings during cavity crossings, and additionally to discover what priorly unobserved features might be hiding in the electric field estimations.

THE COMET - SOLAR WIND INTERACTION REGION

The physics of the cometary environment induced by the effect of the solar wind and radiation on the comet constituents, have multiple times been investigated by in-situ measurements. Prior to any spacecraft missions to comets, Earth based observations proposed theories about the cometary interaction with the solar wind. These theories have been tested and extended by several cometary flybys in the late 1980s and beginning of the 21st century, and latest by the Rosetta mission to comet 67P/Churyumov-Gerasimenko (67P).

This chapter is dedicated to give a description of the large-scale structures and wave observations in the comet - solar wind interaction region based on cometary flybys and preliminary findings from the Rosetta mission. A brief introduction to relevant plasma physical principles leading to the formation and development of boundaries and wave activity in the cometary environment is given in Section 2.1 and 2.2 along with a description of the "life" of cometary neutrals as they are outgassed from the cometary surface, become ionized, and start interacting with the solar wind. Section 2.3 gives a brief introduction to pre-flyby theories, whilst Section 2.4 gives a qualitative description of the present understanding of cometary regions and boundaries. Sections 2.5 and 2.6 give an introduction to wave and turbulence observations in cometary environments, whilst Section 2.7 summarises the chapter.

2.1 Principles of cometary plasma physics

Plasmas consist of free negatively and positively charged particles. The species have similar charge densities on scales much larger than the characteristic length scale, the "Debye length", defined later in Eq. (2.11). Therefore, on large scales the charge density is

$$\rho_e = en_e + \sum_i q_i n_i = 0 \quad (2.1)$$

for a plasma of electron number density n_e and charge e , and i ion species of charge q_i and number density n_i (Langmuir, 1928). This property is called quasi-neutrality. Plasmas show collective behaviour that results in natural frequencies and length scales defined by the particle species (Pécseli), and in the case of negligible resistivity the plasma is "frozen-in" to the magnetic fields. The frozen-in condition states that through a surface in the plasma, the flux of magnetic field lines is constant (Boyd and Sanderson, 2003). Hence, a perfectly conducting plasma is forced to follow the flow of the magnetic field lines and vice versa, meaning that if the magnetic field locally slows down and stagnates, so does the plasma.

Several theories to describe the dynamics of a plasma have been proposed, one of which is the magnetohydrodynamics (MHD) model (Alfvén, 1942). In the MHD model, plasma is described as one electrically conducting medium, which behaviour can be described by the continuity and momentum equations as well as Newton's second law and Maxwell's equations (Pécsele). Hence, MHD combines fluid flows and electromagnetic properties. The continuity and momentum equations are given below for a plasma of mass density $\rho = nm$ and bulk velocity \mathbf{u} .

$$\frac{\partial \rho}{\partial t} + \nabla \cdot (\rho \mathbf{u}) = 0, \quad \text{continuity eq.} \quad (2.2)$$

$$\rho \left(\frac{\partial \mathbf{u}}{\partial t} + (\mathbf{u} \cdot \nabla) \mathbf{u} \right) = -\nabla p + \mathbf{J} \times \mathbf{B}, \quad \text{momentum eq.} \quad (2.3)$$

In Eq. (2.3), p is the pressure, $\mathbf{J} = qn\mathbf{u}$ is the current density and \mathbf{B} is the magnetic field, such that $\mathbf{J} \times \mathbf{B}$ is the Lorentz force term. Other forces can be introduced in Eq. (2.3). However, for a plasma in an interplanetary environment, the most important terms are indeed the pressure gradient and the Lorentz force. To complete the set of MHD equations, the relevant Maxwell equations (Reitz et al., 2008, 2008) are given below, as

$$\nabla \cdot \mathbf{B} = 0 \quad (2.4)$$

$$\nabla \times \mathbf{B} = \mu_0 \left(\mathbf{J} + \epsilon_0 \frac{\partial \mathbf{E}}{\partial t} \right), \quad \text{Ampère's law} \quad (2.5)$$

$$\nabla \times \mathbf{E} = -\frac{\partial \mathbf{B}}{\partial t}, \quad \text{Faraday's law} \quad (2.6)$$

where μ_0 and ϵ_0 are the vacuum permeability and permittivity, respectively. The Gauss's law $\nabla \cdot \mathbf{E} = \rho_e / \epsilon_0$ in the set of Maxwell's equations is omitted. This is due to the fact that, on large scales, the effect of this is already covered by the principle of quasi-neutrality, i.e. the total charge density ρ_e is insignificant (Davidson, 2001). For a plasma of electric conductivity σ_E , Ohm's law states that the current density is related to the electromagnetic fields and plasma flow by

$$\mathbf{J} = \sigma_E (\mathbf{E} + \mathbf{u} \times \mathbf{B}), \quad \text{Ohm's law} \quad (2.7)$$

In the case of ideal MHD, the plasma is collisionless enough to assume that the plasma is a perfect conductor, i.e. $\sigma_E \rightarrow \infty$ (Hopcraft, 1993). This ultimately causes Ohm's law to reduce to $\mathbf{E} = -\mathbf{u} \times \mathbf{B}$, which in turn results in the before-mentioned frozen-in condition of the magnetic field (Davidson, 2001). The fact that an infinite conductivity results in the frozen-in condition, is seen by the effect of $\sigma_E \rightarrow \infty$ on Eq. (2.7) in (2.6), which gives

$$\frac{\partial \mathbf{B}}{\partial t} = \nabla \times (\mathbf{u} \times \mathbf{B}) \quad (2.8)$$

Consider now a magnetic field through a surface S bounded by a closed contour C . The temporal change of magnetic flux through the surface is

$$\frac{d}{dt} \int_S \mathbf{B} \cdot d\mathbf{S} = \int_S \frac{\partial \mathbf{B}}{\partial t} \cdot d\mathbf{S} + \oint_C \mathbf{B} \cdot \mathbf{u} \times d\mathbf{l} \quad (2.9)$$

where \mathbf{u} is the velocity of the line element $d\mathbf{l}$. The right-hand side originates from the two-dimensional Liebnitz theorem (Boyd and Sanderson, 2003, p. 50). Switching the dot- and cross-product in the last

term of the right-hand side and using Stoke's theorem (Spiegel et al., 2009, p. 126) to convert the contour integral to a surface integral, give

$$\frac{d}{dt} \int_S \mathbf{B} \cdot d\mathbf{S} = \int_S \left(\frac{\partial \mathbf{B}}{\partial t} - \nabla \times (\mathbf{u} \times \mathbf{B}) \right) \cdot d\mathbf{S} = 0 \quad (2.10)$$

The last equality stems from Eq. (2.8). Hence, for ideal MHD with $\mathbf{E} = -\mathbf{u} \times \mathbf{B}$, the magnetic flux through a surface does not change with time, which is indeed the frozen-in condition, originally stated by Alfvén (Boyd and Sanderson, 2003).

Collective plasma behaviour

The natural parameters of a plasma are the plasma frequency ω_p and the Debye length λ_D . The Debye length is the length scale at which the potential difference caused by a surplus of negative or positive charge has been shielded by a factor of $\exp[1]$ compared to the related value in a vacuum (Hastie, 1993). Hence, plasma considered at length scales shorter than the Debye length are not necessarily neutral. This is why plasmas are termed "quasi-neutral" and not strictly neutral, even though Eq. (2.1) is true on scales significantly larger than λ_D .

To illustrate the principles behind the shielding, consider a neutral plasma. An intruding ion will cause a localized surplus of positive charge that attracts electrons. The electrons move towards the ion, where the negative charge of the particles shields the positive surplus until no more electrons are attracted by the intruder. The shielding Debye length is given by

$$\lambda_D = \sqrt{\frac{\epsilon_0 k_B T_e}{n_e e^2}} \quad (2.11)$$

where $k_B T_e$ is the thermal energy of the electrons of number density n_e and charge e (Sturrock, 1994). Eq. (2.11) states that an increase in thermal energy of the electrons causes a greater shielding length. This is due to the fact that greater thermal energies result in greater random motion. Conversely, an increase in n_e yields a greater charge density to shield the intruder, leading to a shorter Debye length.

The Debye length is often short in Earth based experiments but might be several meters in tenuous space plasmas (Blandford and Thorne, 2013). This ultimately means that instruments carrying out scientific measurements in space plasmas might be relatively close to the spacecraft body in Debye length scale, and might therefore not be experiencing the quasi-neutrality of the plasma. The consequences of this are further discussed in Sections 3.1 and 3.2.

The plasma frequency is the natural frequency of a plasma. It is given by

$$\omega_p = \sqrt{\frac{n_e e^2}{m_e \epsilon_0}} \quad (2.12)$$

where m_e is the electron mass. The plasma frequency can be derived from electrons being displaced relative to the ions that are too heavy to move. The attractive forces between the bulk electrons and the stationary ions accelerate the electrons towards the ions. The electrons will, however, overshoot the ions and be displaced on the opposite side of the ion bulk, from where they will again be accelerated toward the

surplus of positively charged particles. This leads to a collective oscillation of the electrons (Baumjohann and Treumann, 1996). The relation between the plasma frequency and the electron density in Eq. (2.12) is then sensible, since an increase in n_e causes a greater difference in charge density between the ions and electrons, leading to a stronger attractive force, and hence faster oscillation.

Single particle motion

Several other waves and characteristic frequencies of a plasma can be described by the motion of charged particles in the light of Newton's and Maxwell's equations. Consider a particle of charge q and mass m placed in a stationary and uniform external magnetic field of magnitude $B = \sqrt{B_x^2 + B_y^2 + B_z^2}$ and no electric field. The Lorentz force causes the charged particle to gyrate around the field line in such a manner that the resultant magnetic field induced by the gyration opposes the external field. This means that ions and electrons will gyrate in different directions (Bittencourt, 2004).

Consider a particle of charge q and mass m placed in a uniform magnetic field in the z -direction such that $\mathbf{B} = B\hat{\mathbf{z}}$. The equation of motion is then

$$m \frac{d\mathbf{u}}{dt} = q(\mathbf{u} \times \mathbf{B}) \quad (2.13)$$

Taking the scalar product with \mathbf{u} on each side of the equation, yields that the change in kinetic energy is zero, and hence that the speed is constant. To determine the motion of the particle, consider the three relations of Eq. (2.13):

$$m \frac{d}{dt} \begin{pmatrix} u_x \\ u_y \\ u_z \end{pmatrix} = qB \begin{pmatrix} u_y \\ -u_x \\ 0 \end{pmatrix} \quad (2.14)$$

It is evident from the last equation that $u_z || \mathbf{B}$ is constant. Rearranging the first two equations of Eq. (2.14) yields

$$\frac{du_x}{dt} = -\Omega u_y \quad (2.15)$$

$$\frac{du_y}{dt} = \Omega u_x \quad (2.16)$$

which is a circular motion in the $x - y$ -plane of angular gyrofrequency

$$\Omega = \frac{|q|B}{m} \quad (2.17)$$

Hence, the angular gyrofrequency increases with larger charges and stronger magnetic fields (i.e. stronger forces between the charge and the magnetic field), and decreases with increasing mass.

Since the circumference of a gyration of radius r_L is $2\pi r_L$, the gyroradius can be determined from the gyrofrequency $f_G = \Omega/2\pi$ in Hertz through the period $T = 2\pi r_L / u_\perp$, where $u_\perp = \sqrt{u_x^2 + u_y^2}$. This gives

$$r_L = \frac{1}{2\pi} T u_\perp = \frac{u_\perp}{\Omega} = \frac{m u_\perp}{|q|B} \quad (2.18)$$

Often, the gyroradius is termed the Larmor radius, hence the subscript. The result is that a charged particle in a uniform magnetic field and no electric field possibly moves along the magnetic field lines

with a constant speed and gyrates around the magnetic field with a frequency given by Eq. (2.17) and radius given by Eq. (2.18).

If, however, the electric field is non-zero, the motion of the charged particle will differ from the previous case. As an example, set $\mathbf{E} = E\hat{\mathbf{x}}$ and $\mathbf{B} = B\hat{\mathbf{z}}$ such that $\mathbf{E} \perp \mathbf{B}$. Solving the equation of motion

$$m \frac{d\mathbf{u}}{dt} = q(\mathbf{E} + \mathbf{u} \times \mathbf{B}) \quad (2.19)$$

gives a gyromotion altered by a drift perpendicular to both the electric and magnetic field. This drift is

$$\mathbf{u}_d = \frac{\mathbf{E} \times \mathbf{B}}{|\mathbf{B}|^2} \quad (2.20)$$

from similar arguments as in the previous case. Figure 2.1 schematically illustrates the gyromotion and $\mathbf{E} \times \mathbf{B}$ -drift of positively and negatively charged particles. These are shown together with the motion of charged particles in a magnetic field with a gradient in its magnitude. Phenomenologically, the gradient in the magnetic field magnitude gives rise to a particle drift perpendicular to both the magnetic field and its gradient due to the magnetic field magnitude dependence of the gyroradii of a charged particle. The $\mathbf{E} \times \mathbf{B}$ -drift does not give rise to any current, since electrons and ions are drifting in the same direction. However, so does the $\nabla \mathbf{B}$ -drift.

For magnetized plasmas, one can derive hybrid oscillations (Pécseli) such as the electrostatic lower hybrid wave that is a hybrid between the ion and electron dynamics. In cometary environments, waves in the frequency range of the lower hybrid frequency have been observed a number of times. This is further discussed in Section 2.5.2 and in the results and discussion chapter of this work.

The basic plasma physics principles introduced in this section are essential in the generation of the comet - solar wind interaction region, and serve as theoretical background in the understanding of observed physical features in this region. The following section uses the introduced phenomena in a brief description of the general principles behind cometary boundary generation, whereas the subsequent sections make use of this section to build the understanding of specific features in the cometary environment.

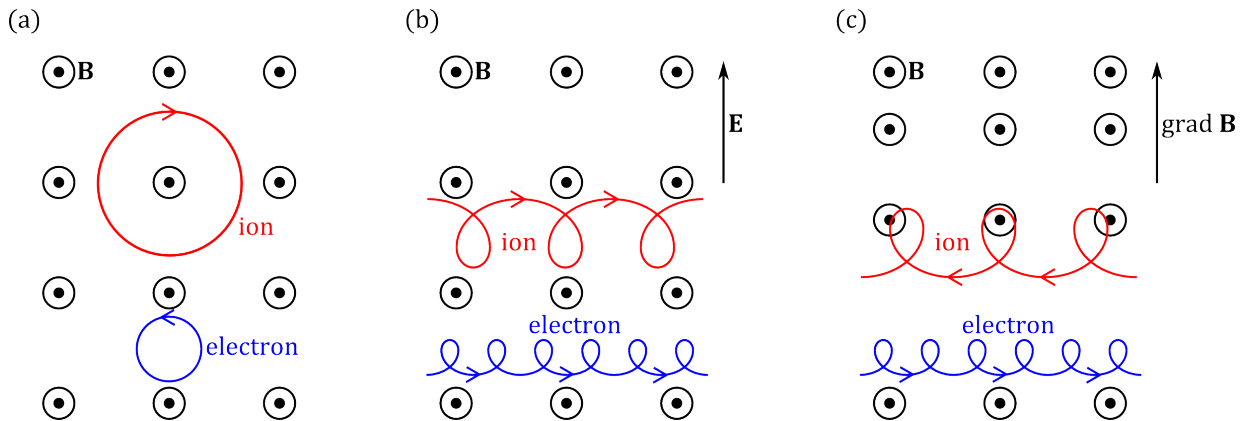


Figure 2.1. Single particle motion. (a) Uniform magnetic field, no electric field. (b) Perpendicular magnetic and electric field ($\mathbf{E} \perp \mathbf{B}$). (c) Magnetic field gradient ($\nabla \mathbf{B} \perp \mathbf{B}$).

2.2 Generation of cometary boundaries

When illuminated by the Sun, energy from the solar radiation causes sublimation of ice from the comet surface. The amount of sublimated ice per time unit is described by the cometary outgassing rate Q , on which the activity level of a comet and the extent of the comet - solar wind interaction region depend on. It is, therefore, highly relevant to estimate Q when doing in-situ observations of the cometary environment. By assuming spherical symmetry and negligible gravitational pull on the cometary neutrals, the observed neutral number density n_n at a distance r from the comet nucleus is related to the outgassing rate Q by

$$n_n(r) = \frac{Q}{4\pi r^2 u_n} \quad (2.21)$$

where u_n is the mean speed of neutrals radially from the comet. This is only true if no neutrals are lost to ionization on their travel from the comet to the distance r . Taking into account the photodestruction losses of neutrals, Eq. (2.21) is altered by an exponential decrease with time (Haser, 1957). That is

$$n_n(r) = \frac{Q}{4\pi r^2 u_n} \exp\left[-\frac{v_d r}{u_n}\right] \quad (2.22)$$

where v_d is the photodestruction rate and includes the ionization rate. Crovisier (1994) reviews studies on the photodestruction rates at 1 AU, and finds typical values of the order of 10^{-5} s^{-1} for water-group ions. Cravens (1989a) mentions that the typical ionization frequency of neutrals at 1 AU is 10^{-6} s^{-1} . Since the cometary neutrals travel at a speed of about 1 km/s, the characteristic ionization length scale of cometary neutrals at 1 AU is $10^5 - 10^7 \text{ km}$ in a cometary environment (Gombosi, 2015). Hence, a great part of the neutrals can extend far from the comet nucleus before being subject to ionization.

Rearranging Eq. (2.22) provides an estimate of the outgassing rate as seen by a spacecraft in the vicinity of a comet:

$$Q = 4\pi u_n r^2 n_n \exp\left[\frac{v_d r}{u_n}\right] \quad (2.23)$$

This model has often been used as a proxy of the comet outgassing rate from in-situ measurements of the neutral density (see e.g. Goetz et al. (2016a), Behar et al. (2016), Wyckoff et al. (1988), Simon Wedlund et al. (2016)), but gives an estimate of Q that is inaccurate if the outgassing is not spherically symmetric.

The neutral particles sublimated from the comet surface undergo ionization by either solar radiation, electron impact or charge exchange (Nilsson et al., 2015b). An example of photoionization or electron impact ionization of a water molecule is shown in Eq. (2.24) where E_{ph} is the photon energy, whilst Eq. (2.25) gives an example of charge exchange between a solar wind proton and a cometary water molecule.



Cravens (1989a) mentions that in the inner coma photoionization is the dominant ionization process. More precisely, Simon Wedlund et al. (2017) found by using a three-dimensional hybrid model of the cometary plasma environment at perihelion that whilst photoionization is indeed the primary process close to the

comet, charge exchange and ionization by electron impact are important contributors farther from the comet nucleus, and dominate beyond the cometopause boundary.

Charge exchange substitutes light solar wind ions with heavy cometary ions, whilst photo- and electron impact ionization add new heavy ions to the solar wind. Hence, all three processes result in a greater mass density of the solar wind. Due to the conservation of momentum and energy, the mass addition ultimately leads to a slowing of the solar wind flow (Gombosi, 2015). The cometary ions are then said to be "picked-up" by the solar wind that is hereby "mass-loaded" (Coates, 1997).

Cometary ion pickup and solar wind mass-loading

The motion of a newly-born cometary ion is determined by the interaction between the ion and the solar wind magnetic field \mathbf{B}_{SW} and convectional electric field $\mathbf{E}_{SW} = -\mathbf{u}_{SW} \times \mathbf{B}_{SW}$ in the comet frame, where the particle is nearly at rest compared to the solar wind, i.e. $u_i \approx 1 \text{ km/s} \ll u_{SW} \approx 400 \text{ km/s}$ far from the comet (Cravens and Gombosi, 2004). Since the convectional electric field of the solar wind depends on the direction of the magnetic field relative to the flow, the resulting motion of the ion depends on the angle $\varphi \in [0; \pi/2]$ between the magnetic field and the solar wind flow direction (Ip, 2004).

The ion speed u in the solar wind frame can be split into a component parallel to the magnetic field $u_{\parallel} = u \cos(\varphi)$ and one perpendicular to the field, i.e. $u_{\perp} = u \sin(\varphi)$. Consider now the resultant cometary ion speed for the two extreme cases of magnetic field \mathbf{B}_{SW} versus flow velocity \mathbf{u}_{SW} configurations. For $\mathbf{B}_{SW} \perp \mathbf{u}_{SW}$, i.e. $\varphi = \pi/2$, the motion of the ion in the solar wind frame is purely in the plane perpendicular to the magnetic field. In the comet frame, the resultant motion of the picked-up ion is a gyration around the magnetic field and an $\mathbf{E}_{SW} \times \mathbf{B}_{SW}$ drift in the the solar wind flow direction due to the finite convectional electric field (as is the situation in Figure 2.1(b)). For $\mathbf{B}_{SW} \parallel \mathbf{u}_{SW}$, i.e. $\varphi = 0$, the motion of the newly created cometary ion in the solar wind frame is purely parallel to the magnetic field and solar wind flow direction since $v_{\perp} = 0$. The particle's resultant speed in the solar wind frame is $\mathbf{u} = -\mathbf{u}_{SW}$, and hence the ion is stationary in the comet frame (Ip, 2004). In the former case, the resulting ion velocity distribution in the solar wind frame is a ring distribution and in the latter an ion beam distribution, whilst other intermediate magnetic field configurations yield a ring-beam distribution (Gombosi, 1991). Glassmeier (2017) points out that these ion distributions are unstable and lead to plasma waves and turbulence.

The ion pickup, mass-loading, and slowing-down of the solar wind flow, together with an outward pressure caused by the outgassed cometary particles, result in a stagnation of the solar wind upstream of the comet nucleus. The continued motion of the solar wind on the flanks of the comet, creates the cometary tails, and several global permanent boundaries and transient small-scale features are induced in the comet - solar wind interaction region in front of the comet (Mandt et al., 2016).

2.3 Earth-based observations

Even before sending spacecrafts into the interplanetary environment, ground-based observations on cometary ion tails gave information about the existence and components of the solar wind and the interplanetary magnetic field. Some of the great breakthroughs on the subject of comet - solar wind interactions came from Hannes Alfvén and Ludwig Biermann in the late 1950s and 1960s (Ip, 2004).

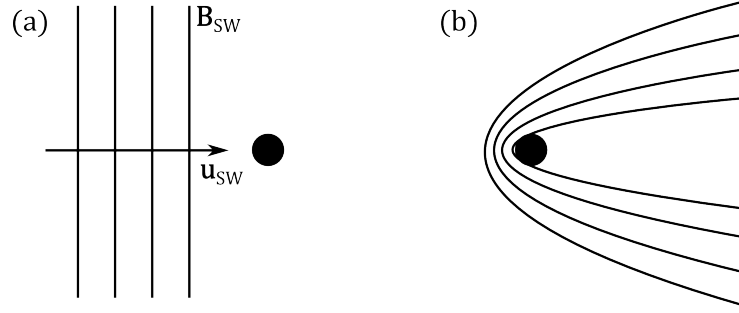


Figure 2.2. Alfvén's draping model. When a solar wind beam with a frozen-in magnetic field interacts with cometary ions, the field lines pile up in front of the comet nucleus. Since the field lines are still frozen into the moving solar wind on the flanks, they drape around the comet obstacle, forming the comet plasma tail.

Alfvén (1957) pointed out that earlier difficulties in explaining features of the plasma tails of comets, observable from Earth, could be overcome by considering the draping of a solar wind frozen-in magnetic field around the comet. The principle behind Alfvén's draping model is illustrated in Figure 2.2.

Alfvén (1957) explains that when a solar wind beam moving radially from the Sun (see Figure 4 in the referred article) arrives at the comet, the cometary neutrals will be subject to a heating due to a shock wave produced at the collision between the solar beam and comet. This results in increased ionization of the particles. The newly generated ions are within the solar wind beam and, hence, start interacting with the magnetic field. The interaction freezes the solar wind plasma and magnetic field into the cometary plasma in front of the comet nucleus. As a result, the magnetic field lines stagnate and pile-up in front of the comet. With time, the solar wind beam moves past the comet, draping its magnetic field lines around the comet as illustrated in Figure 2.2(b) (Ip, 2004). Alfvén (1957) additionally suggests that the draping of the magnetic field lines around the comet nucleus might be subject to magnetohydrodynamic waves.

From a hydrodynamical model of the comet - solar wind interaction region of an active comet, Biermann et al. (1967) found that this region consists of at least two boundaries, i.e. a distant bow shock ($r_{bs} \sim 10^6 - 10^7$ km from nucleus) and a contact surface ($r_{cs} \sim 10^4$ km from nucleus). The structure of the interaction region was found to depend strongly on the solar wind conditions and cometary outgassing rates. However, Biermann's model found consistent similarities between the model solutions. Some of these are summarized in Figure 2.3. The transition region between the bow shock and contact surface was thought to contain both cometary particles and solar wind ions, whilst the contact surface separates the transition region from a region closest to the comet containing only particles of cometary origin.

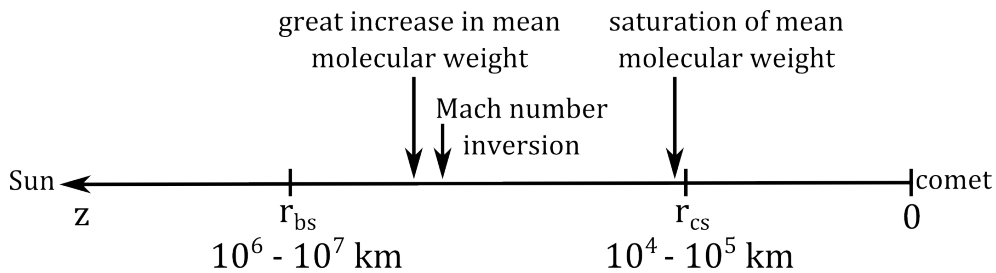


Figure 2.3. A selection of features in the cometary environment modelled by Biermann et al. (1967) for an active comet of outgassing rate $Q \sim 10^{30} \text{ s}^{-1}$, and fixed parameters estimated to fit the real life situations in the solar wind.

At the bowshock r_{bs} , the solar wind undergoes a shock and goes from being super- to subsonic. A shock in a fluid is characterized by its Mach number. The Mach number gives the ratio of the flow velocity u_d to the local sound speed c_s , i.e.

$$M = \frac{u_d}{c_s} \quad (2.26)$$

yielding that a flow of $M < 1$ is subsonic, whilst a flow with $M > 1$ is supersonic (Pröls, 2010). The shock in the Biermann et al. (1967) model is characterized by a sharp decrease in the solar wind Mach number (from 10 to 0.5) and a corresponding increase in the solar wind pressure. Downstream of the bow shock the Mach number continuously decreases due to mass-loading until a point where the Mach number undergoes an inversion. This inversion is caused by a sudden increase in the mean molecular weight due to pickup of heavy cometary ions (see Section 2.2). The inversion is overcome by a divergence in the flow before going to zero at the contact surface. At the contact surface, the mean molecular weight is saturated due to a low share of initial light solar wind ions relative to heavy cometary ions at this point.

The existence of the cometary bow shock and the development of a solar wind free cavity separated by a large transition region, as well as the draping of the solar wind magnetic field around the comet nucleus, have been validated by several in-situ measurements.

2.4 Cometary boundaries based on in-situ studies

Since the late 20th century, several spacecraft flybys of comets have enhanced the understanding of comet - solar wind interaction and the existence of resulting cometary boundaries. As pointed out in Section 2.3, two cometary boundaries, i.e. the bow shock and the contact surface, were predicted before the first cometary encounters in 1985. Spacecraft flybys of comets have verified the presence of these theoretically expected boundaries (see e.g. Neubauer et al. (1986), Balsiger et al. (1986), Young et al. (2003) and Goetz et al. (2016b)), and have, in addition, shown the existence of several non-expected cometary regions (see e.g. Fuselier et al. (1988) and Neubauer (1987)). The unexpected boundaries include the mystery boundary, cometopause, magnetic pile-up layer, and ion pile-up layer (see Mandt et al. (2016) for a recent review).

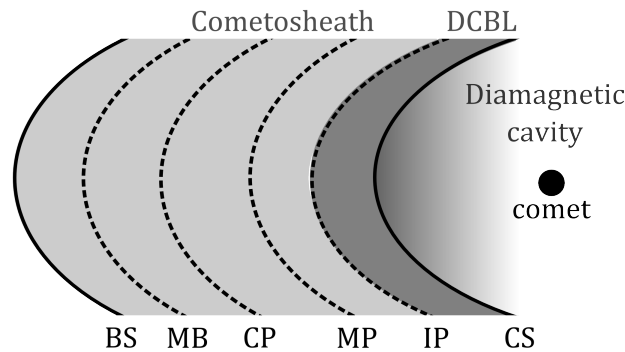


Figure 2.4. Extended model of cometary boundaries achieved by simulations and spacecraft flybys of comets. The cometary environment consists of three major regions bound by the bow shock (BS) and the contact surface (CS). These are the region upstream of the bow shock, the cometosheath between the bow shock and the contact surface, and the diamagnetic cavity between the contact surface and the comet nucleus. The cometosheath consists of the mystery boundary (MB), cometopause (CP), magnetic pile-up region (MP), and ion pile-up region (IP) that marks the beginning of the diamagnetic cavity boundary layer (DCBL). Inspired by Mandt et al. (2016).

Table 2.1. Summary of observations made by pre-Rosetta spacecraft flybys of comets. Dates (format DD/MM/YY), heliocentric distances d_h , and outgassing rates Q , shown together with rough estimates of cometocentric distances to boundaries observed during the flybys. ^(a) Grard et al. (1989), ^(b) Cravens and Gombosi (2004), ^(c) Mandt et al. (2016), ^(d) Balsiger et al. (1986), ^(e) Krankowsky et al. (1986), ^(f) Young et al. (2003)

	<i>ICE</i>	<i>Vega 1</i>	<i>Vega 2</i>	<i>Giotto</i>		<i>DS1</i>
Comet	21P/G-Z	1P/H	1P/H	1P/H	26P/G-S	19P/B
Flyby date	11/09/85	06/03/86	09/03/86	14/03/86	10/07/92	21/09/01
d_h [AU]	1.03	0.792	0.834	0.902	1.01	1
Q [s^{-1}]	$3 \cdot 10^{28}$ ^(b)	$1.5 \cdot 10^{30}$	$5 \cdot 10^{29}$	$6.9 \cdot 10^{29}$ ^(e)	$7 \cdot 10^{27}$	$3.5 \cdot 10^{28}$ ^(f)
<i>Approximated cometocentric distances to observed boundaries [km]</i>						
Bow shock	$1.3 \cdot 10^5$ ^(b)	$1.02 \cdot 10^6$ ^(a)	$1.3 \cdot 10^6$ ^(a)	$1.16 \cdot 10^6$ ^(b)	$2 \cdot 10^4$ ^(b)	10^5 ^(f)
Cometopause	n/a	$1.67 \cdot 10^5$ ^(a)	$1.66 \cdot 10^5$ ^(a)	n/a	n/a	n/a
Ion pile-up	n/a	$1.1 \cdot 10^4$ ^(c)	$1.1 \cdot 10^4$ ^(c)	10^4 ^(d)	n/a	n/a
Contact surface	n/a	n/a	n/a	$4.6 \cdot 10^3$ ^(d)	n/a	n/a

Figure 2.4 summarizes the pre-Rosetta understanding of the macroscopic features in the interaction region achieved by cometary flybys, simulations, and early theories, whilst Table 2.1 gives an overview of boundary observations during some of the cometary flybys prior to the Rosetta mission. The table shows approximated data from the flybys of the comets 21P/Giacobini-Zinner (21P/G-Z), 1P/Halley (1P/H), 26P/Grigg-Skjellerup (26P/G-S), and 19P/Borrelly (19P/B).

Note that the cometocentric distances of the characteristic boundaries displayed in Table 2.1 are not necessarily on the comet - Sun line. Since the boundaries are probably not spherically symmetric around the comet nucleus, the cometary longitudinal and latitudinal orientations of the spacecrafts influence the observed boundary distances. By assuming a static boundary with a parabolic shape, the cometocentric distances on the comet - Sun line of the boundaries can be estimated. This is shown in e.g. Table 1 in Mandt et al. (2016) for the Vega 1 and 2 flybys of comet 1P/H and Giotto flyby of 1P/H and 26P/G-S.

The fact that all boundaries are not observed during all of the cometary flybys might be caused by the achieved cometocentric distances. It is, however, important to keep in mind that comets differ from each other and changes activity stage throughout their orbit around the Sun. Hence, all boundaries might not exist at all comets and throughout all evolutionary states of the comet. In the following sections, the characteristics of different boundaries and regions of the cometary environment are described.

2.4.1 Bow shock (BS)

The bow shock has been observed for all cometary flybys (see Table 2.1). As predicted by Biermann et al. (1967), observations have shown that when entering the vicinity of a comet, the first comet-related phenomenon a spacecraft encounters is the slowing of the supersonic solar wind (Galeev et al., 1986). This eventually leads to subsonic solar wind speeds and a cometary bow shock. The slowing down of the solar wind is caused by ion pickup and the related mass-loading (Ip, 2004). Since the outgassing and ionization rates allow a significant part of the cometary neutrals to move far from the nucleus before being lost to ionization, the solar wind is gradually slowed down upstream of the bow shock. Cravens and Gombosi (2004) emphasise that this leads to a weak bow shock with a Mach number of about 2 at large cometocentric distances.

From the data displayed in Table 2.1, it is evident that there is a clear link between the stand-off distance of the bow shock and the gas production rate of the comet. That is, the greater the gas production rate Q , the greater the distance to the bow shock. This is further investigated by Koenders et al. (2013) who estimate the stand-off distances of the bow shock at comet 67P during the evolutionary states monitored by the Rosetta spacecraft.

2.4.2 Cometosheath (CS)

In the cometosheath between the bow shock and the contact surface, an increasing number of cometary ions are picked up by the solar wind. Hence, the dominant species of the plasma changes from being initially solar wind ions to heavy cometary ions. The point at which the switch of dominant ion species happens is termed the cometopause (see Galeev et al. (1988)). This more or less continuous ion pickup and mass-loading lead to a further slowing of the shocked solar wind, as also predicted by Alfvén and Biermann (see Section 2.3). Mandt et al. (2016) remark that the cometosheath is now considered a permanent feature of the interaction region.

During the Giotto mission to comet 1P/H, a "mystery" region was observed prior to the cometopause within the cometosheath (see e.g. Fuselier et al. (1988)). As the name suggests, the origin of this region is still unknown, and it is not predicted by any models (Coates and Jones, 2009). Fuselier et al. (1988) report on a clear bifurcation of the increased ion densities within the region during the inbound leg of the Giotto mission to comet 1P/H, whilst Coates (1997) describes the region as consisting of large densities of hot electrons and an enhancement of the solar wind velocity and density without any related signatures in the magnetic field.

The magnetic pile-up region is subject to a sharp increase in the magnetic field magnitude. This was observed in the inbound leg of Giotto's flyby of comet 1P/H, and possibly as a less pronounced feature at the outbound leg (Neubauer, 1987). Mandt et al. (2016) conclude that the magnetic pile-up might be a transient region, and that the magnetic field might as well go through a gradual increase throughout the cometosheath before dropping to zero at the contact surface. This is consistent with what was expected from Alfvén's draping model in Figure 2.2 and seen in hybrid simulations of the plasma environment around comet 67P (Simon Wedlund et al., 2017), where a gradual slowdown of the solar wind flow leads to a gradual increase in the magnetic field magnitude until stagnation at the contact surface.

Diamagnetic cavity boundary layer (DCBL)

In the diamagnetic cavity boundary layer (DCBL) just outside the contact surface, the ions pile up to form the ion pile-up region or recombination layer. Goldstein et al. (1989) report on a roughly 50 km wide ion pile-up layer observed by the Giotto flyby of comet 1P/H. Within the DCBL the ion density is estimated to have increased with at least a factor 3.5 compared to the density outside the layer. Ip (2004) mentions that the ion density increase might be related to a decrease in recombination of ions, which is also reflected in the sudden decrease in electron temperature to which recombination is strongly related.

In addition to the presence of the plasma density spike close to the outer edge of the DCBL, the appearance of the density distribution changes at this feature (Mandt et al., 2016). The Giotto heavy ion measurements of the ion pile-up region are shown in the plot of Figure 2.5. In the figure, *A* marks the position of the ion pile-up region at 10^4 km, *B* is the ion density minimum, whilst *C* is the contact surface at 4.6×10^3 km (see Table 2.1).

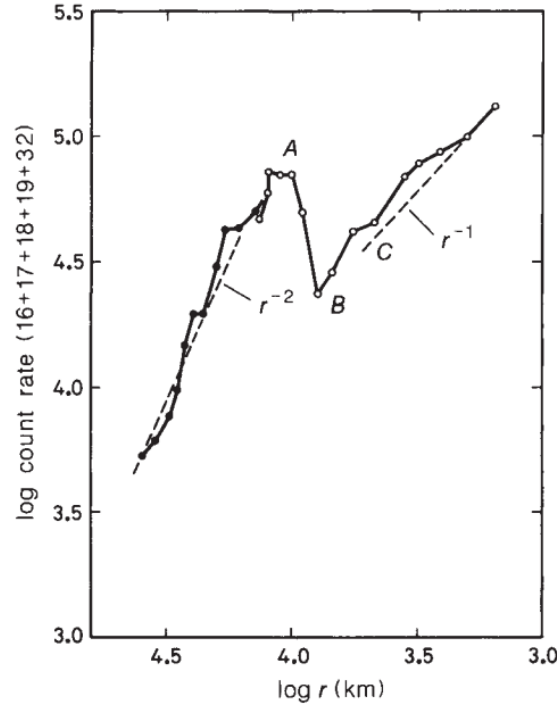


Figure 2.5. Radial evolution of the ion count rate measured aboard the Giotto flyby of comet 1P/H. The numbers on the y-axis represent the masses of the considered ions in amu. Source: Balsiger et al. (1986).

At the Giotto flyby of comet Halley, the plasma density was seen to decrease with cometocentric distance as r^{-1} inside the cavity, whilst the decay in plasma density went as r^{-2} outside the ion pile-up layer (Balsiger et al., 1986). The $n_i \propto r^{-1}$ dependence inside the contact surface can be obtained theoretically by considering the coupling between ion and neutral velocity ($u_i \approx u_n = \text{const.}$) that arises due to the exclusion of the solar wind within the contact surface (Gombosi, 2015): Consider a non-disturbed radially expanding cometary atmosphere consisting of neutrals and ions of density n_n and n_i , respectively. Within the cavity, the neutrals and ions move with similar speeds, since ions are mostly generated by photoionization of the neutrals (Cravens, 1989a). Ions are then lost by recombination and created by ionization of the neutrals. The former is described by the ion loss rate $L_i = \gamma n_i^2$, where $\gamma = 1.21 \times 10^{-5} / \sqrt{T_e} \text{ cm}^3 \text{ s}^{-1}$ is the reaction rate determining the recombination, whilst the latter is described by the ionization frequency at 1 AU, $I_0 \approx 10^{-6} \text{ s}^{-1}$, and the heliocentric distance d_h in AU by $S_i = I_0 n_n / d_h^2$ (see Gombosi (2015) and Cravens (1989b)). The ionization rate is hence slightly smaller than the photodestruction rate ν_d of Eq. (2.22), as would be expected since I_0 is contributing to ν_d . Including these source terms on the right-hand side of the continuity equation (2.2), gives that for steady state conditions with $u_i = u_n = \text{const.}$, the ions behave spherically symmetric as

$$\frac{1}{r^2} \frac{\partial}{\partial r} (r^2 u_n n_i) = S_i - L_i \quad (2.27)$$

This ultimately results in the differential equation

$$\frac{\partial}{\partial r} (r^2 n_i) = \frac{I_0}{d_h^2} \frac{Q}{4\pi u_n^2} - \frac{\gamma}{u_n} r^2 n_i^2 \quad (2.28)$$

where Q is related to n_n by Eq. (2.21). By defining $Q_0 = \pi d_h^2 u_n^3 / \gamma I_0$ and assuming that only n_i and r itself

are dependent on the radial distance, the solution to Eq. (2.28) becomes

$$n_i = \left[\sqrt{1 + \frac{Q}{Q_0}} - 1 \right] \left(\frac{u_n}{2\gamma} \right) \frac{1}{r} \quad (2.29)$$

which gives the $n_i \propto r^{-1}$ dependence observed during the cavity crossing of the Giotto flyby of comet 1P/H seen in Figure 2.5. Gombosi (2015) estimates that for an active comet $Q \gg Q_0$, and hence Eq. (2.29) can be rewritten to

$$n_i \approx \sqrt{\frac{Q}{Q_0}} \left(\frac{u_n}{2\gamma} \right) \frac{1}{r} \quad (2.30)$$

Galand et al. (2016) elaborate that the difference in cometocentric distance-dependence of the ion and neutral density of Eq. (2.22) stems from the fact that in addition to the radial motion in the inner regions of the coma, ions are created by photoionization of neutrals. Outside of the ion pile-up layer, the ion density goes as r^{-2} Balsiger et al. (1986). Gombosi (2015) mentions this is a result of neglectable electron recombination this far from the comet.

2.4.3 Diamagnetic cavity (DC)

The diamagnetic cavity is thought to be the innermost region of the cometary coma and is characterized by an exclusion of the solar wind magnetic field. It is separated from the cometsheath by the contact surface at the point where the magnetic field magnitude reaches zero. The gradual decrease in the magnetic field magnitude happens within the DCBL just outside the contact surface. Prior to the Rosetta mission, the cavity has been observed only once, i.e. during the Giotto flyby of comet 1P/H (Neubauer et al., 1986). The relatively small cometocentric distances of orbits close to perihelion has made the Rosetta spacecraft cross the contact surface of comet 67P more than 600 times, giving the possibility of further studies on the dynamical features related to this region (Goetz et al., 2016b).

As mentioned, when the comet surface is illuminated by solar radiation, ice from the comet surface layers is sublimation, causing the comet to outgas heavy neutral. These accelerated to velocities of the order of 1 km/s, as measured within the cavity of comet Halley during the Giotto flyby (Cravens, 1986). Some of these cometary neutrals will be ionized when still inside the diamagnetic cavity, and travel with speeds strongly coupled to the neutral speeds. This coupling is the dominant factor in the ion speed until reaching the contact surface. Here the ions will be slowed down to (almost) stagnation due to coupling to the solar wind magnetic field outside the cavity (Cravens and Gombosi, 2004). Ultimately, this creates a sudden ion velocity shear near the contact surface.

In a somewhat static picture, the cavity boundary exists due to a balancing of the inward magnetic pressure force from the slowed down solar wind and the outward ion-neutral drag, described by the equation

$$-\frac{\partial}{\partial r} \left(\frac{B^2}{2\mu_0} \right) = n_i m_i v_{in} (u_i - u_n) \quad (2.31)$$

The magnetic pressure is given in terms of the solar wind magnetic field magnitude B , whilst the ion-neutral drag is given by the cometary ion density n_i and mass m_i , and the ion-neutral momentum transfer collision frequency $v_{in} = k_{in} n_n$ with $k_{in} \approx 2 \times 10^{-9} \text{ cm}^3 \text{ s}^{-1}$ (Cravens, 1987). Close to the boundary, the ions are almost stagnant ($u_i \approx 0$) due to interaction with the stagnant solar wind (Cravens and Gombosi, 2004).

Hence, the velocity difference between the cometary ions and neutrals is approximately $(u_i - u_n) \approx -u_n$. By integrating Eq. (2.31), Cravens (1987) suggests that the cometocentric stand-off distance of the contact surface r_{cs} varies linearly with $Q^{3/4}$ and inversely with the undisturbed magnetic field magnitude of the solar wind. This is derived by applying the radial expressions of n_i and n_n inside the cavity (Eq. (2.30) and (2.21)) to Eq. (2.31), i.e.

$$\frac{\partial}{\partial r} \left(\frac{B^2}{2\mu_0} \right) = C_1 \frac{Q^{3/2}}{r^3} \quad (2.32)$$

where $C_1 = (u_n m_i k_{in}) / (8\pi\gamma\sqrt{Q_0})$ is assumed constant. Eq. (2.32) is then integrated from the piled up magnetic field at $r = \infty$, where $B(\infty) = B_0$, to the cometocentric distance r . This gives

$$B^2(r) - B_0^2 = -\mu_0 C_1 \frac{Q^{3/2}}{r^2} \quad (2.33)$$

and hence the radial dependence of the magnetic field magnitude is

$$B(r) = B_0 \sqrt{1 - \mu_0 C_1 \frac{Q^{3/2}}{B_0^2 r^2}} \quad (2.34)$$

At the contact surface the magnetic field goes to zero, that is $B(r_{cs}) = 0$. Hence, the stand-off distance r_{cs} of the contact surface is

$$r_{cs} = \sqrt{\mu_0 C_1} \frac{Q^{3/4}}{B_0} \quad (2.35)$$

which gives the $r_{cs} \propto Q^{3/4}/B_0$ dependence mentioned above.

The magnetic field magnitude profile of Eq. (2.34) and estimated contact surface position of Eq. (2.35) of a 1P/H-like comet during the Giotto flyby in 1986 are shown in Figure 2.6. The model uses the heliocentric distance and outgassing rate of Table 2.1, and assumes a magnetic field magnitude of $B_0 = 50$ nT in the pile-up region and an electron temperature of $T_e = 1000$ K (Cravens, 1986). Comparing the modelled contact surface stand-off distance of 4.7×10^3 km to the observed one indicates that diamagnetic cavity can to some extent be explained by the suggested model. Note, however, that the model only shows the inner coma and hence does not illustrate the ion pickup, mass-loading and flow of the solar wind. Thus, no gradual increase or magnetic field pile-up appear upstream of the contact surface.

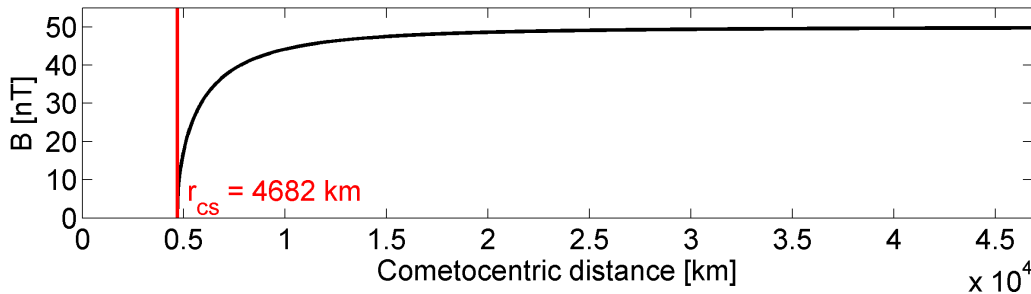


Figure 2.6. Modelled cometocentric profile of the solar wind magnetic field magnitude and contact surface stand-off distance using Eq. (2.34) and (2.35) for a 1P/H-like comet with an outgassing rate $Q = 6.9 \times 10^{29} \text{ s}^{-1}$ at a heliocentric distance $d_h = 0.902$ AU. The electron temperature and piled up solar wind magnetic field magnitude are set to $T_e = 1000$ K and $B_0 = 50$ nT, respectively, following the values in Cravens (1986).

During the Rosetta mission to comet 67P, observations of the diamagnetic cavity have been made several times. Goetz et al. (2016a) provides the first study of a diamagnetic cavity crossing as observed at a cometocentric distance of 170 km by the magnetometer onboard the Rosetta spacecraft on July 26, 2015 (see Section 3.2.3 for the magnetic field structure and boundary analysis of this cavity). On this day, the Haser model of Eq. (2.23) gives an estimate of the outgassing rate of $Q = 4 \times 10^{27} \text{ s}^{-1}$. However, Goetz et al. (2016a) argue that in the pre-Rosetta understanding of the diamagnetic cavity and its boundary reviewed by Cravens (1987), the observed contact surface stand-off distance of 170 km requires an outgassing rate of one order of magnitude greater than the estimated one. The difference in the theoretically expected and observed cometary distance of the contact surface is, in Goetz et al. (2016a), explained by Kelvin-Helmholtz instabilities developed on the global cavity boundary and triggered by an asymmetric cometary outgassing. The Kelvin-Helmholtz instability on the border between two fluids originates from a velocity shear (Pécsele). Hence, it is not unlikely that this instability can live in the contact surface where possibly asymmetrically distributed cavity plasma meets the stagnant DCBL plasma.

The statistical study of cavities at comet 67P observed by the magnetometer onboard the Rosetta spacecraft by Goetz et al. (2016b) supports the claim that the observed cavities are not the global cometocentric ellipse-shaped cavity with a sharp boundary observed around comet 1P/H, but more likely small elliptical pockets that might be explained by the boundary instabilities proposed by Goetz et al. (2016a).

Israelevich and Ershkovich (1994), in addition, suggested that an ion gyration-generated electric current is associated with the DCBL. This current is caused by the interaction between cometary ions and the piled-up magnetic field outside the cavity as illustrated in Figure 2.7.

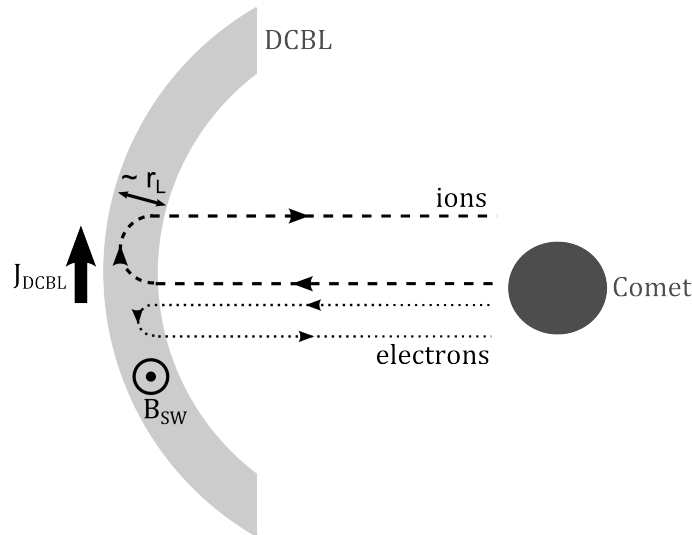


Figure 2.7. Simplified illustration of the generation of the DCBL electric current J_{DCBL} . Ionized cometary particles move outwards in the magnetic field-free cavity. In the DCBL, they start gyrating (the ions with a gyroradius of r_L) perpendicular to the solar wind magnetic field B_{SW} , until re-entering the cavity. Inspired by Israelevich et al. (2003).

When ions moving with a finite speed radially from the comet penetrate into the boundary layer, the movement of the ions will be disturbed by the presence of the solar wind magnetic field B_{SW} . This leads to an ion gyration of gyroradius r_L perpendicular to the magnetic field lines. After half a gyration, the ions have returned to the magnetic field free cavity, continuing their motion radially towards to comet. This gives rise to a current J_{DCBL} within the boundary, but no current in the cavity itself, as illustrated in Figure 2.7 (Israelevich and Ershkovich, 1994). Similarly, the free electrons produced by the ionization of cometary neutrals in the cavity will be affected by the presence of the magnetic field at the boundary layer. The gyration of the electrons is in the opposite direction of the ion gyration, due to the difference in the sign of their charges. Hence, both species add up to the same effective current in the cavity boundary. Since the gyroradius is proportional to the mass of the gyrating particle (see Eq. (2.18)), the electron and ion gyroradii will differ from each other. Ions will therefore penetrate deeper into the boundary than the electrons, leading to a charge separation within the boundary layer. This results in a polarization electric field, in addition to the DCBL current.

From variations in the magnetic field components during several hundred crossings of the diamagnetic cavity around comet 67P, Goetz et al. (2016b) estimate the current density in the boundary layer of the cavities to be of the order of $1 \mu A/m^2$. Until recently, no electric field was thought to be present inside the diamagnetic cavity itself, leaving open the question about the closure of the current. Gunell et al. (2017), however, investigates the presence of ion acoustic waves inside the cavity and finds that the signatures might be explained by a closure of the DCBL current in the outer regions of the diamagnetic cavity itself. Wave observations in the cometary environment can, hence, increase the understanding of the large-scale structures of the interaction region. The subsequent sections briefly discuss some of the several wave phenomena observed in cometary plasma and their implications for the physics of the environments.

2.5 Observed wave-activity during in-situ measurements

Whenever the solar wind plasma is disturbed by a local plasma of a different charge density and flow speed, it is likely that waves will be excited. Recently, magnetic field observations done on-board the Rosetta spacecraft showed puzzling low-frequency oscillations at about 40 mHz for a low-activity phase at a cometocentric distance of 30 – 100 km (Richter et al., 2015). These are now known as the *singing comet* feature of comet 67P at a low-activity state and were not predicted before the Rosetta mission (Deca et al., 2017).

As mentioned, Gunell et al. (2017) report on observations of water ion acoustic waves near 200Hz during a diamagnetic cavity crossing at comet 67P on August 3, 2015. These are interpreted as being excited by the closure of the DCBL current (see Figure 2.7 for an illustration of the generation of a DCBL current), picked up by the Rosetta spacecraft because it did not go sufficiently deep into the cavity to lose this signal. The observed frequency is interpreted as a signature of ion acoustic waves with (cold) electrons moving relative to the ions using a set of dispersion relations valid in a magnetic field-free plasma environment. The differential movement of charged particles results in a current in the density range of 50 – 700 nAm⁻² inside the cavity (Gunell et al., 2017), which is close to the 10³ nAm⁻² DCBL current observed by Goetz et al. (2016b).

Other wave phenomena, e.g. in the frequency range near the water-group ion gyration frequency, and near the lower hybrid frequency (LHF), have been observed during more than one cometary encounter. This

section provides an introduction to some of the wave observations done at pre-Rosetta cometary flybys and during the two years of continuous measurements of the plasma environment of comet 67P.

2.5.1 Low-frequency waves caused by gyration of ions

Upstream of the bow shock, in the comet - solar wind interaction region of comet 21P/G-Z, 26P/G-S, and 1P/H low-frequency waves near the local water-group ion gyrofrequency have been detected (see e.g. Glassmeier et al. (1997) for a review). The waves are thought to be caused by pickup of newly ionized cometary ions (Lee, 1989). Hence, they are expected to live in regions where the cometary neutrals have just undergone ionization. With a characteristic ionization length scale of $10^5 - 10^7$ km (Gombosi, 2015), this is acquired both upstream of the bow shock and in the cometosheath (see Table 2.1 for observed boundary extends at comets). Since the cometary ions, e.g. water-group ions, are relatively heavy, the gyrofrequencies given by Eq. (2.17) are low. In Table 2.2, the theoretically computed water-group ion gyrofrequencies and -radii are given for the comet flybys assuming H_2O^+ -ions of mass 18 amu travelling with a speed of $u_{SW} = 400$ km/s (assuming $\mathbf{B}_{SW} \perp \mathbf{u}_{SW}$) perpendicular to the magnetic field in the solar wind frame. These are shown together with the observations done on these low-frequency waves upstream of the bow shocks during the ICE and Giotto flybys of comets.

In relation to the ICE observations at 21P/G-Z, Tsurutani and Smith (1986) argue that the cometocentric observation distance is on the order of the characteristic ionization length scale. This is, together with the similarity between the theoretically computed ion gyrofrequency and the observed wave, a good indicator that the observed waves are indeed a signature of cometary ion-pickup upstream of the bow shock.

A phenomenological illustration of the electric part of the electromagnetic waves generated due to the gyration of a charged particle in a constant magnetic field is given in Figure 2.8. Here the observer is stationary relative to the solar wind. The observer measures the varying potential from a fixed location as the charged particle, with a radially symmetric potential field, moves closer to and further away from the observer during one gyration. The measured potential at the observer caused by the ion is depicted in Figure 2.8(b). From the observed potential, the electric field is deduced using Poisson's equation $E = -\nabla V$. The electric field shows clear periodical wave signature with a frequency equal to the gyrofrequency of the ion. The magnetic field induced at the observer due to the gyration of the ion varies periodically in time in a similar way as the electric field.

Table 2.2. Parameters during low-frequency wave observations at comet 21P/G-Z, 26P/G-S, and 1P/H: Magnetic field magnitudes B , cometocentric distances during observations d_{obs} , theoretically computed water-group ion gyrofrequencies $f_{\text{H}_2\text{O}}$, observed peak frequencies f_{obs} , and estimated gyroradii r_L of the H_2O ion. More information about these cometary flybys can be found in Table 2.1. ^(a) Glassmeier et al. (1997), ^(b) Tsurutani and Smith (1986), ^(c) Glassmeier and Neubauer (1993), and ^(d) Tsurutani et al. (1995).

	21P/G-Z (ICE)	26P/G-S (Giotto)	1P/H (Giotto)
B [nT]	8 ^(a)	20 ^(a)	8 ^(a)
d_{obs} [km]	2.5×10^5 ^(b)	6×10^5 ^(c)	1.7×10^6 ^(a)
$f_{\text{H}_2\text{O}}$ [mHz]	6.8	17	6.8
f_{obs} [mHz]	6.6 ^(d)	17 ^(d)	7.4 ^(d)
r_L [km]	9.4×10^3	3.4×10^3	9.4×10^3

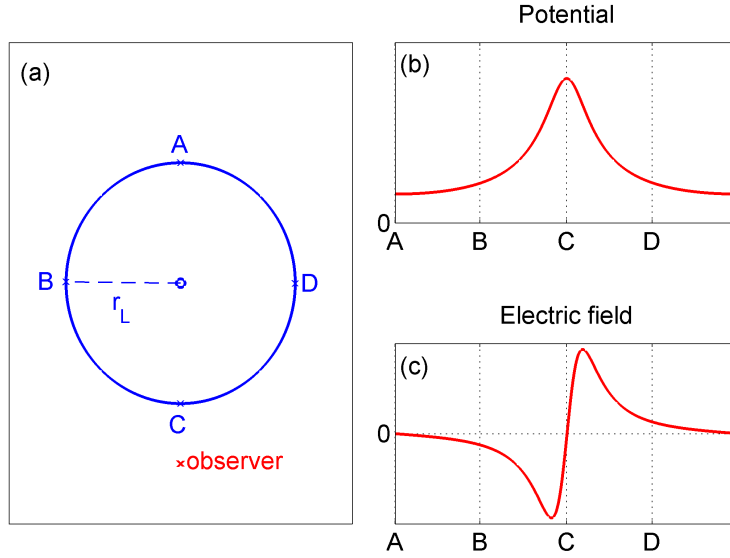


Figure 2.8. Phenomenological description of low-frequency waves generated by gyration of ions in a magnetic field. (a) Gyration of ion with Larmor radius r_L perpendicular to a magnetic field line pointing into the paper. (b) The resulting potential, and (c) electric field of the gyration experienced by a stationary observer. A, B, C and D mark points on the gyromotion.

Note, however, that the observed wave in Figure 2.8 does not take into account the $\mathbf{E} \times \mathbf{B}$ -drift of the charged particle, and nor does it include the instabilities arising from the ion pickup in a cometary environment, as briefly mentioned in Section 2.2. A more thorough study of the excitation of low-frequency waves resulting from the pickup of newly born cometary ions can be found in e.g. Lee (1989) and Thorne and Tsurutani (1987).

2.5.2 Lower hybrid (LH) waves in the inner coma

Wave activity in the LHF range has been observed in the vicinity of comet 1P/H (Savin et al., 1986), and 67P (Karlsson et al., 2017). It has in addition been observed during the AMPTE barium gas release in the Earth's magnetosphere (Bingham et al., 1991), where a diamagnetic cavity was created by the intruding neutrals in the solar wind, similarly to the generation of the cometary cavities. The LHF is a "hybrid" frequency containing a mix of ion and electron gyrofrequencies, Ω_{ci} and Ω_{ce} , and of the ion plasma frequency ω_{pi} . It is characterized by (Pécsele)

$$\Omega_L = \left[(\Omega_{ci}\Omega_{ce})^{-1} + \omega_{pi}^{-2} \right]^{-1/2} \quad (2.36)$$

Savin et al. (1986) report on the detection of low-frequency electric field waves within 15×10^4 km of comet 1P/H during the Vega 2 flyby. These are seen as a peak in the power of the electric field near 15 Hz, which is in the LHF range (Galeev et al., 1986). Increases in wave activity near this frequency are found to correlate well with regions of enhanced ion density, yielding that this wave activity might be related to the generation of cometary ions. In addition, increased wave activity in the frequency range 200-400 Hz within this region was observed. Galeev et al. (1986) explains that these high-frequency waves are oblique Langmuir waves with frequencies related to the electron cyclotron frequency Ω_{ce} by

$$\Omega_o \approx (1/5 - 1/3)\Omega_{ce} \quad (2.37)$$

where Ω_{ce} is the electron gyrofrequency. Oblique Langmuir waves are thought to be related to energy transfer from ions to electrons (Galeev, 1989). The wave detections and sudden increase in ion density makes Savin et al. (1986) conclude that the observed region is subject to so-called critical ionization velocity (CIV) events. The reason for this conclusion is explained in the following.

A CIV event is the ionization of neutrals moving with a speed greater than a critical speed ($u > u_c$) relative to a magnetized plasma (see Figure 2.9). It was originally proposed by Alfvén (1954) as an explanation to the formation of planets in the solar system, but now additionally serves as an explanation for events in the cometary environment. The process converts mechanical energy of the moving neutral gas into electrostatic energy through interaction with the plasma and its electromagnetic field. By that the density of the plasma increases. For this to happen, the required kinetic energy of the intruding neutral gas has to equal the ionization energy E_{ionize} . Hence, for neutrals of mass m , the CIV is

$$u_c = \sqrt{\frac{2E_{ionize}}{m}} \quad (2.38)$$

However, keep in mind that this is only true if the energy transfer processes are optimal. If not, an efficiency term with a value between 0 and 1 can be introduced on the right hand side of the equation. This would yield a greater critical velocity of the neutrals (Galeev et al., 1986).

The CIV mechanism is poorly understood, and several models have been proposed to explain the phenomenon. Some of the models are reviewed by Brenning (1992), who concludes that none of the proposed models fully explains the observed features in experiments and, hence, that several processes must play a role in the complex mechanism of CIV events. However, it is widely accepted that the main source of ionization of the neutrals in CIV events is impact with energetic electrons (Lai, 2001). To explain the origin of the electron energization, Alfvén (1960) suggested that the intrusion of a moving neutral gas in a plasma displaced ions causing inhomogeneities in the plasma. The magnetic field does not allow the electrons to follow the ions, and hence a voltage difference will occur. Eventually, the electrons are accelerated by this voltage difference making them energetic enough to ionize the neutral gas.

The LH instability is often mentioned as an important factor in the CIV mechanism (Formisano et al., 1982), and a peak in the spectrum corresponding to the LHF has often appeared in experiments (Brenning, 1992). In the comet - solar wind interaction region, the solar wind stagnates upstream of the contact surface. This does not influence the speed of the cometary neutrals significantly causing the neutrals to travel with a finite speed relative to the plasma, suggesting that CIV events could be accountable for some of the ionization of outgassing neutrals in the inner coma of the interaction region. Hence, an excitation of the LHF along with an ion density increase and anisotropic distributions of suprathermal electrons, as observed by Savin et al. (1986) and Galeev et al. (1986) during the Vega 2 flybys of comet 1P/H, are good indicators of the CIV process.

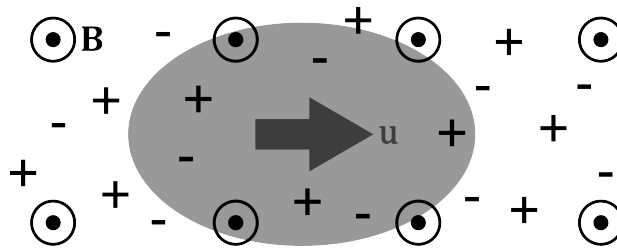


Figure 2.9. Illustration of the principle behind CIV events. The gray area indicates neutrals moving with a speed u relative to a magnetized quasi-neutral plasma at rest. Inspired by Lai (2001).

Karlsson et al. (2017), additionally, studies localized water ion LHF signatures seen in the electric field around comet 67P a few months after perihelion at cometocentric distances of 149 km and 348 km. The LH waves often correlate with intervals of great density gradient, and Karlsson et al. (2017) concludes that they might be generated by LH drift instabilities and result in a bulk heating of the electrons. The fact that the LH waves might heat electrons in comet-like environments was also deduced from the AMPTE mission (Bingham et al., 1991). Some of the wave signatures identified at the LHF in the Karlsson et al. (2017) study are reproduced in Section 3.3.3 as a validation of the analysis method implemented for this work.

2.6 Plasma turbulence

In a cometary environment with waves and possibly irregular changes in the pressure and flow velocity, the plasma might behave chaotically and turbulent-like. In this study, the phenomenological description of a turbulent-like behaviour in plasmas is used in the characterization of the studied events. However, this study does not aim to provide a thorough discussion on the observed turbulent-like features and, hence, provides only a brief introduction to the principles of fluid and plasma turbulence followed by a phenomenological description and dimensional derivation of the Kolmogorov energy cascade law.

Turbulence in a fluid can be thought of as a number of differently sized chaotic eddies coexisting and evolving in time and space (Narita, 2012). If a fluid is non-turbulent, it is said to have a laminar flow, whilst a fully turbulent system shows highly non-linear dynamics and ultimately has an unpredictable behaviour (Haas, 1993). The fundamental difference between fluid and plasma turbulence is the energies present in the system. Whilst fluid turbulence deals with kinetic and thermal energies, plasma turbulence in addition considers electric and magnetic energies. Hence, plasma turbulence is a mix of fluid turbulence and purely plasma-related features.

The dynamics of an ordinary fluid of velocity \mathbf{u} , pressure p , constant mass density ρ and viscosity ν is described by Navier-Stokes momentum equation (Haas, 1993):

$$\frac{\partial \mathbf{u}}{\partial t} + (\mathbf{u} \cdot \nabla) \mathbf{u} - \nu \nabla^2 \mathbf{u} = -\frac{1}{\rho} \nabla p \quad (2.39)$$

Hence, the description of fluid dynamics differs from the dynamics described by the plasma momentum equation of Eq. (2.3) in the sense that the $\mathbf{J} \times \mathbf{B}$ term vanishes in the neutral fluid picture.

By assuming constant density, i.e. incompressibility of the fluid, the continuity equation of Eq. (2.2) yields that $\nabla \cdot \mathbf{u} = 0$. Furthermore, the pressure p in the momentum equation does not influence the dynamics of an incompressible fluid (Narita, 2012). Hence, the temporal change in the flow velocity is dependent on the velocity itself through advection and dissipation terms, that is $(\mathbf{u} \cdot \nabla) \mathbf{u}$ and $\nu \nabla^2 \mathbf{u}$, respectively. If the advection term dominates, the flow is laminar. If, instead, the dissipation term is dominant, the flow is turbulent. The ratio between the magnitude of these two terms is described by the Reynolds number Re which is a measure of the strength of the turbulence (Frisch, 1995). Let U and L be the characteristic speed and length of the fluid flow. With $\nabla \rightarrow 1/L$, the Reynolds number becomes

$$Re = \frac{|(\mathbf{u} \cdot \nabla) \mathbf{u}|}{|\nu \nabla^2 \mathbf{u}|} \sim \frac{U^2/L}{\nu U/L^2} = \frac{UL}{\nu}, \quad \text{Reynolds number} \quad (2.40)$$

A low Reynolds number correspond to a laminar flow, whilst a high Reynolds number gives a turbulent flow (Frisch, 1995). When $Re \rightarrow \infty$ the fluid is considered fully turbulent (Carbone and Pouquet, 2009).

2.6.1 Kolmogorov turbulence

A well-established description of the spectral signatures of a fully developed turbulence is the Kolmogorov model. The idea behind the Kolmogorov model is that an energy injection in the fluid creates large-scale eddies. These eddies split into smaller scale eddies, transferring all of their kinetic energy to kinetic energy in the smaller eddies. The small eddies split into even smaller eddies and so on, causing an energy cascade (Haas, 1993). However, this splitting cannot go on forever. Consider the Reynolds number in Eq. (2.40). For smaller scales, the Reynolds number decreases, and hence at some point the dissipation term becomes the most important feature, resulting in a dissipation of the energy. Hence, the energy cascade consists of three stages, i.e. the injection, transfer and dissipative ranges (Frisch, 1995). The energy cascade caused by eddy splitting is phenomenologically illustrated in Figure 2.10.

The injection range marks the scales at which energy is injected into the system by external forces or shear flows. It is followed by the transfer range that consists of energy cascades. At some point the small-scale-limit is reached. The dissipation process starts dominating and kinetic energy is converted to thermal energy. Hence, the ultimate energy conversion in the Kolmogorov theory is from kinetic energy injected to the system to thermal energy (Narita, 2012).

In the transfer range the energy-decay with wavenumber follows a power-law (Frisch, 1995). This is illustrated from a few dimensional arguments: Consider a newly generated eddy characterized by a size l and flow speed u in a turbulent fluid. Narita (2012) notes that the eddy will split into a smaller-sized eddies after a time $\tau = l/u$, termed the energy transfer time. For the n 'th eddy splitting, the energy transfer time and kinetic energy per unit mass is therefore

$$\tau_n = l_n/u_n \quad \text{and} \quad E_n = \frac{1}{2}u_n^2 \quad (2.41)$$

Assuming that the entire amount of kinetic energy in the n 'th state is transferred without loss to the next generation yields that the energy transfer rate is

$$\epsilon_n = \frac{dE_n}{dt} \sim \frac{E_n}{\tau_n} \quad (2.42)$$

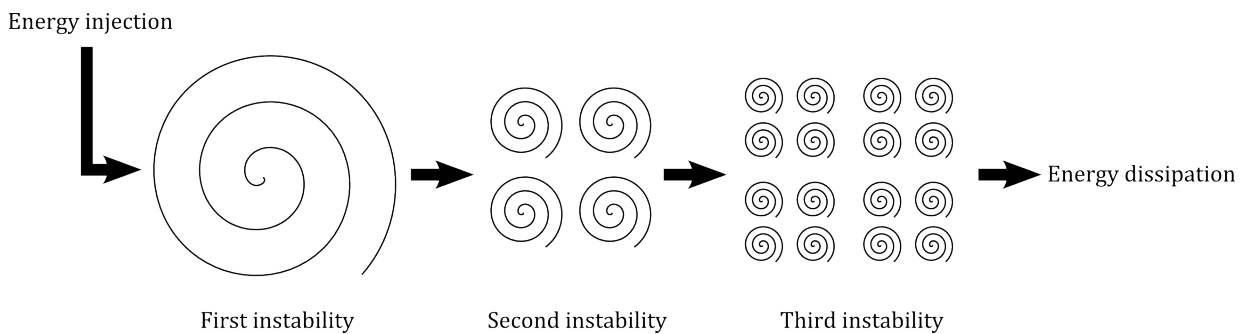


Figure 2.10. Energy cascade: Injected energy creates large-scale eddies. These split into smaller eddies that again split until a minimum eddy size is reached. The energy is then dispersed due to the viscosity of the fluid.

For a stationary state, the energy transfer rate is constant throughout the entire cascade (Narita, 2012). Combining the equations in (2.41) with (2.42) using the relation between length scale and wave number $l_n \propto k_n^{-1}$, give

$$E_n \propto \epsilon^{2/3} k_n^{-2/3} \quad (2.43)$$

By definition, the total kinetic energy E_{kin} over the entire range of the energy spectrum $E(k)$ is

$$E_{kin} = \int_0^\infty E(k) dk \quad (2.44)$$

and hence, the kinetic energy in the n 'th generation of the cascade can also be given as

$$E_n = E(k_n) k_n \quad (2.45)$$

This together with Eq. (2.43) give the wavenumber dependence of the energy spectrum:

$$E(k) = C_K E k^{-1} = C_K \epsilon^{2/3} k^{-5/3} \quad (2.46)$$

in which the subscript n has been excluded. The constant C_K appears in Eq. (2.46) to make up for the pure dimensional analysis in this section (Narita, 2012).

Figure 2.11 shows the energy spectrum related to the eddy-splitting of Figure 2.10. The energy $E(k)$ is the kinetic energy in an eddy of size l with wave number $k = 2\pi/l$, and k_I and k_D mark wave numbers related to eddies in the injection and dissipation ranges, respectively.

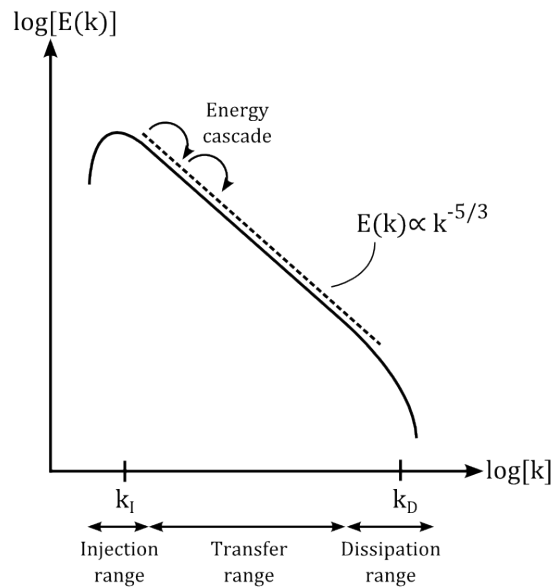


Figure 2.11. Kolmogorov energy spectrum in wave number space. The energy cascade for eddies in the transfer range follows a power-law. Inspired by Narita (2012)

Observed turbulence in cometary environments

In the comparative study of turbulence observed at comets 26P/G-S, 21P/G-Z and 1P/H, Tsurutani et al. (1995) found that the observed turbulence in the magnetic field followed a Kolmogorov-like power-law in addition to the excited water-ion gyrofrequencies summarized in Table 2.2. At higher frequencies than the water-ion gyrofrequencies, Tsurutani et al. (1995) note that the spectral densities (introduced in Section 3.3) of the magnetic fields fell off with frequency as f^α , where $\alpha_{GS} = -1.9$, $\alpha_{GZ} = -1.9$, and $\alpha_H = -2.1$, are the exponents for 26P/G-S, 21P/G-Z and 1P/H, respectively, which resembles the Kolmogorov power-law exponent of $-5/3 = -1.67$.

2.7 Summary of signatures in the cometary environment

The comet - solar wind interaction region upstream of the comet is a diverse environment consisting of large-scale features, wave-activity and varying degrees of turbulence-like behaviour caused by the interaction of ionized cometary particles with the solar wind plasma and electromagnetic fields. Figure 2.12 summarizes the boundary signatures of an active comet discussed in Section 2.4.

The interaction region consists of two main boundaries, i.e. a weak bow shock (Mach number 2), where the solar wind goes from being super- to subsonic, and the contact surface, where the solar wind magnetic field drops to zero.

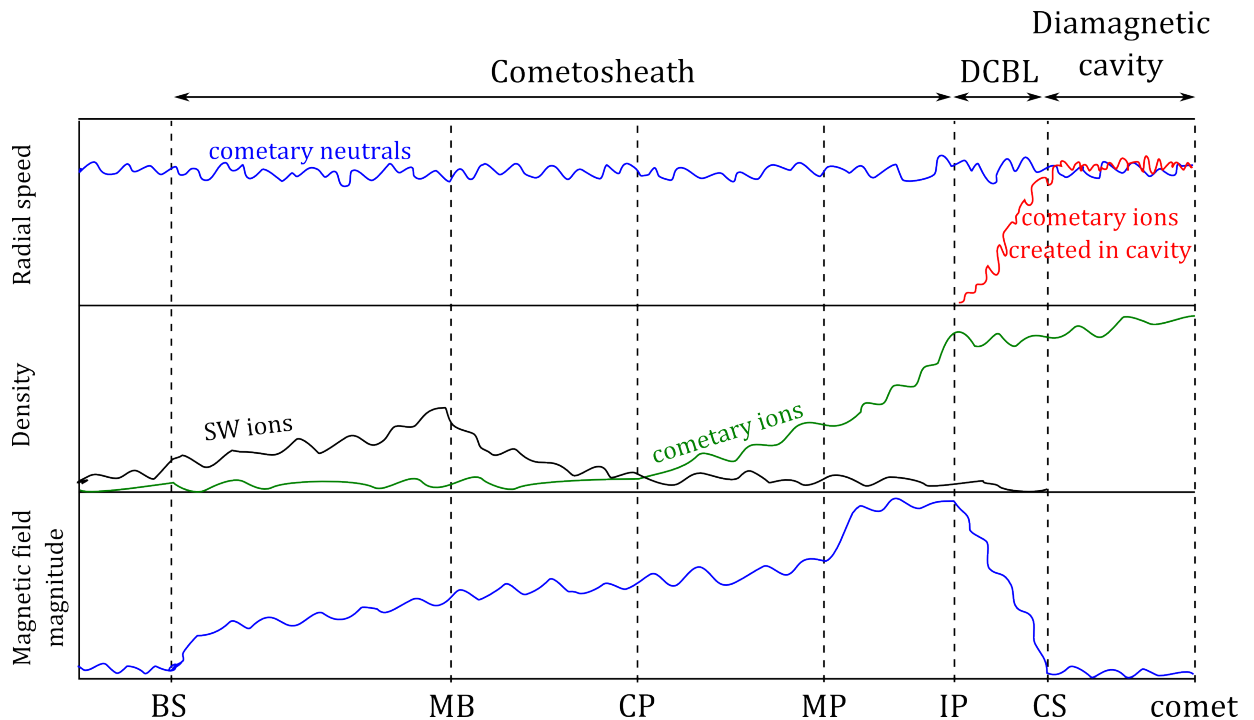


Figure 2.12. Simplified large-scale characteristics of the cometary particle speeds, solar wind density, cometary ion density, and magnetic field magnitude as functions of cometocentric distance. Features in the parameters determines the location of the bow shock (BS), mystery boundary (MB), cometopause (CP), magnetic pile-up region (MP), ion pile-up region (IP), and contact surface (CS). The approximate locations of the cometosheath, diamagnetic cavity boundary layer (DCBL), and diamagnetic cavity are shown, as well. Not to scale.

The contact surface marks the beginning of the diamagnetic cavity, from where the solar wind is excluded. Upstream of the contact surface, the ion pile-up region marks the outer boundary of the diamagnetic cavity boundary layer (DCBL) within which the magnetic field gradually goes to zero. The typical speed of the cometary neutrals and ions created in the diamagnetic cavity is 1 km/s, but when entering the DCBL, the ions are affected by the magnetic field and start gyrating.

The density of the cometary ions vary inversely with the cometocentric distance r inside the ion pile-up region. At greater distances, the cometary ion density goes as r^{-2} due to the change in chemical reactions. In the region upstream of the contact surface, ions interact with the solar wind and are picked-up. Frequent observations of low-frequency waves in the water-group ion gyrofrequency range are thought to be related to the pickup process.

Numerous observations of waves in the water-group lower hybrid frequency (LHF) range have also been carried out in cometary environments. These are often correlated with density gradient and are thought to be related to critical ionization events, where neutrals moving relative to a magnetized plasma are ionized by the energy conversion of kinetic to electrostatic energy. In the inner coma, neutrals are moving with finite speed relative to the almost stagnant plasma, and it is hence likely that this mechanism might work here.

Note, however, that every comet is different from another. Hence, the signatures depicted in Figure 2.12 and discussed in the sections above might not exist at all comets and throughout their entire orbit. This is e.g. the case for the mystery boundary and the magnetic pile-up region that might be replaced by a gradual increase in the magnetic field magnitude. In addition, small transient events, variations in the solar wind, and asymmetric outgassing might alter the comet - solar wind plasma environment. The "singing comet" feature observed at comet 67P by the magnetometer aboard the Rosetta spacecraft is a good example of this. These waves were observed in the cometary coma when the comet was in a low-activity phase. The waves have not been observed at earlier cometary flybys, where the inner coma has been dominated by water-group ion gyrofrequency waves generated by ion-pickup (Richter et al., 2015).

INSTRUMENTATION AND DATA PROCESSING

The Rosetta spacecraft has followed comet 67P for two years and was the first spacecraft to orbit a comet. It carried a variety of instruments to image and characterize the comet nucleus and its effects on the solar wind. In this work, the instruments of most interest are the ones in the Rosetta Plasma Consortium (RPC). These were designed to characterize the encountered plasma and electromagnetic field environments from in-situ measurements of the comet - solar wind interaction region. The RPC instruments are described in Section 3.2 following a description of the spacecraft and solar distances to the comet, the considered coordinate systems, and the so-called "spacecraft sheath". Section 3.3 provides a description and discussion of the Fourier and Morlet wavelet methods used in this work to obtain the electric and magnetic field spectra from observation by some of the RPC instruments. The implemented methods, presented in this chapter, are included as MATLAB scripts in Appendix A.

Rosetta arrived at comet 67P on August 6, 2014 (Bauer, 2014), and orbited the comet until landing on the comet surface on September 30, 2016, marking the end of the mission (Gibney, 2016). The two years of scientific measurements made by the RPC instruments aboard the Rosetta spacecraft have resulted in a wealth of plasma and electromagnetic field data enabling a characterization of the evolution of the comet - solar wind interaction region. Figure 3.1 shows the cometocentric distance of the spacecraft and the heliocentric distance of the comet throughout the two years of cometary monitoring.

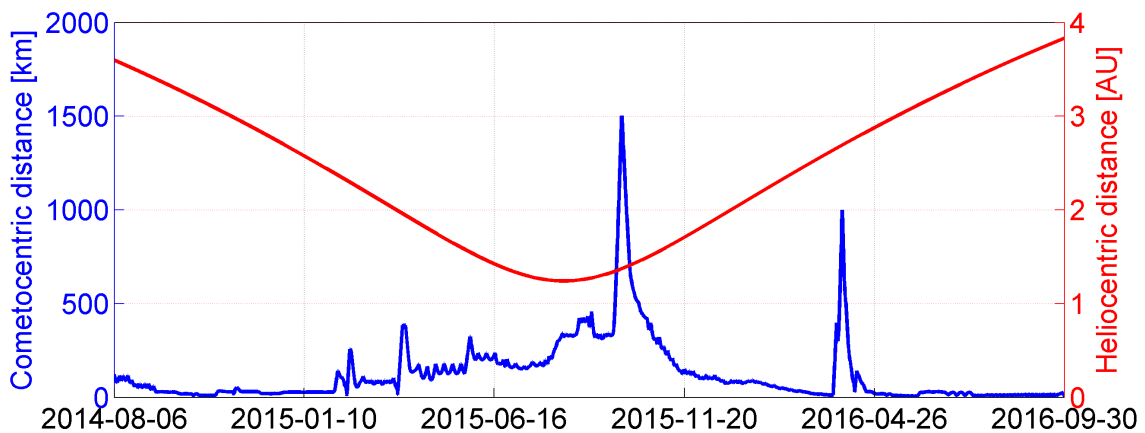


Figure 3.1. Overview of the Rosetta mission from arrival at comet 67P on August 6, 2014, to end of mission at September 30, 2016.

The Rosetta spacecraft followed the evolution of the comet as it went from being a relatively inactive comet at a solar distance of 3.60 AU, through its closest approach to the Sun at 1.24 AU in August 2015, and back to lower activity levels at 3.83 AU. Throughout the evolution of the cometary environment, the Rosetta spacecraft has mostly been orbiting the dayside of the comet at a distance of less than a few hundred kilometres. This was interrupted by a dayside excursion in September and October 2015 and a tail excursion in March and April 2016, when the cometocentric distance of the spacecraft was increased.

During the Giotto flyby of comet 1P/H, the spacecraft was well inside the diamagnetic cavity at a distance of a few hundred kilometres from the nucleus (see Table 2.1). However, the outgassing rate and hence the activity level of comet 67P throughout the Rosetta mission has been lower by several orders of magnitude than it was for comet 1P/H during the Giotto mission (Hansen et al., 2016). The result is that the Rosetta spacecraft has spend most of its time outside the diamagnetic cavity at small cometocentric distances providing in-situ measurements of the innermost cometary regions and their evolution. Electromagnetic signatures of crossings of the contact surface in May 2015 and February 2016, when the solar distance and hence the evolutionary state of the cometary environment differ much from each other, are shown and analysed later on in this work.

3.1 Spacecraft sheath

When introducing a spacecraft in a space environment, the local plasma changes due to interactions with the intruding body. This leads to a sheath of disturbed plasma surrounding the spacecraft. The presence of the sheath might result in altered data in scientific measurements done onboard the spacecraft, and is hence important to keep in mind when analysing measurements done by the RPC instruments.

An undisturbed plasma is quasi-neutral and includes of free charges. When a spacecraft is placed therein the thermal motion of the charged particles will cause a migration of these towards its surface. For a shadowed spacecraft, more electrons than ions will migrate to the surface due to greater electron speeds (Schott, 1968, 1968). This leaves the spacecraft negatively charged relative to the plasma, causing a potential difference between the spacecraft surface and the undisturbed environment far from the spacecraft body (Lai, 2011). The plasma potential is often chosen as zero, and the spacecraft potential is then the potential of the spacecraft relative to the undisturbed plasma. When the spacecraft surface is sunlit, electrons are emitted from the surface. This yields a more positive spacecraft potential.

The charging of the spacecraft relative to the plasma sets up an electric field that attracts plasma species of opposite charge and repulses the others. Hence, the spacecraft will be surrounded by a sheath, within which the mean charge densities of the electrons and ions are unbalanced yielding that inside the sheath the principle of quasi-neutrality is broken. Throughout the sheath the local potential goes to zero, and ideally the charge density imbalance shields the spacecraft such that the plasma far from the spacecraft is left undisturbed (Chen, 1965, 1965).

Characteristic length scale of the sheath

To illustrate the characteristic lengths of the sheath and the existence of an undisturbed plasma far from the spacecraft, consider the one dimensional case of introducing a potential V_0 at a distance $x = 0$ in a plasma with undisturbed density n_0 and electron and ion densities and temperatures n_e , n_i , T_e , and T_i . Poisson's

equation is then

$$\frac{d^2V}{dx^2} = -\frac{1}{\epsilon_0}e(n_i - n_e) \quad (3.1)$$

in which ϵ_0 is the vacuum permittivity, and $e(n_i - n_e)$ gives the total charge density of the disturbed plasma (assuming only single-charged ions). Normalizing Eq. (3.1) by the use of the dimensionless quantities

$$\eta = -\frac{eV}{k_B T_e}, \quad v_i = \frac{n_i}{n_0}, \quad v_e = \frac{n_e}{n_0}, \quad \xi = \frac{x}{R}$$

with R being the characteristic length scale related to the spacecraft shielding, yields

$$\frac{\lambda_D^2}{R^2} \frac{d^2\eta}{d\xi^2} = v_i(\eta) - v_e(\eta) \quad (3.2)$$

in which λ_D is the Debye length given in Eq. (2.11). Setting $R = \lambda_D$ and considering the case with stationary ions, such that $n_i = n_0$ everywhere, and electrons in thermal equilibrium, that is $n_e = n_0 \exp[-\eta]$, give

$$\frac{d^2\eta}{d(x/\lambda_D)^2} = 1 - \exp[-\eta] \approx \eta \quad (3.3)$$

The right-hand side follows from the approximation of the Taylor expansion of the exponential for small x . Hence, for a small potential relative to the thermal energy of the electrons, the spacecraft potential decays as

$$V = V_0 \exp[-x/\lambda_D] \quad (3.4)$$

The potential has decreased by a factor of $\exp[1]$ at a distance λ_D from the surface, yielding that the Debye length is the characteristic length scale of the spacecraft sheath. The ideal case of a clear sheath boundary requires the fulfilment of the so-called "sheath criterion" that sets a criterion for the ion speed at the sheath edge. To fulfil this criteria the potential might extend beyond the sheath edge and generate a "presheath" within which the ions are accelerated (Pécseli). It is, however, not a part of the scope of this work to discuss this further.

During the Rosetta mission, the sheath often exceeds a few meters. This is seen by considering typical values in the expression of the Debye length of Eq. (2.11). Throughout the Rosetta mission, the electron temperature has been observed to be on the order of 5 eV (Odelstad et al., 2016) with a typical density of 150 cm^{-3} (Edberg et al., 2015). This yields a Debye length of $\lambda_D \approx 1.4 \text{ m}$. Hence, a plasma closer than 1.4 m to the spacecraft body is deep within the sheath.

It is important to keep in mind that even though the mere presence of the spacecraft alters the plasma characteristics, the plasma response to an intruding body is rather well understood and can to some extent be corrected for in the analysis. Hence, data acquired within the sheath can still provide reliable information about the undisturbed plasma environment and ultimately on the comet - solar wind interaction.

3.2 Instruments description

The main instruments used in this work, are the instruments of the Rosetta Plasma Consortium (RPC). RPC consists of five field and plasma instruments that, with complementary in situ measurements, were intended to characterize the evolution of the plasma environment around comet 67P as the comet activity changed (Carr et al., 2007). The five sensors making up the RPC are the Ion Composition Analyser (ICA), Ion and Electron Sensor (IES), Langmuir Probe (LAP), Fluxgate Magnetometer (MAG), and Mutual Impedance Probe (MIP). In addition to the RPC instruments, the Rosetta Orbiter Spectrometer for Ion and Neutral Analysis comet pressure sensor ROSINA-COPS that is located on the spacecraft body provides an estimate of the neutral gas density for one of the studied events. Figure 3.2 shows the location of the five RPC instruments on the Rosetta spacecraft.

Since the RPC instruments are placed at different positions on the spacecraft body and at different distances from the body, they experience the spacecraft potential differently. This is important to keep in mind when comparing results from the RPC instruments and when carrying out experiments using both LAP probes simultaneously, which is the situation in the electric field mode. An example of the different sheath effects on the RPC instruments is given by Odelstad et al. (2016) where the spacecraft potential is estimated both from the lower boundary of the ICA ion energy spectra (see Section 3.2.4) and from the bias potential sweeps of LAP1 (see Section 3.2.2). Odelstad et al. (2016) finds that LAP1 only experiences a part of the total spacecraft potential, but that by adjusting for the position of the probe relative to the ICA instrument the two methods of obtaining the spacecraft potential often correlate well. The study, in addition, concludes that the spacecraft potential has been mostly negative throughout the Rosetta mission, indicating that the thermal motion of the electrons is more important than the photoemission.

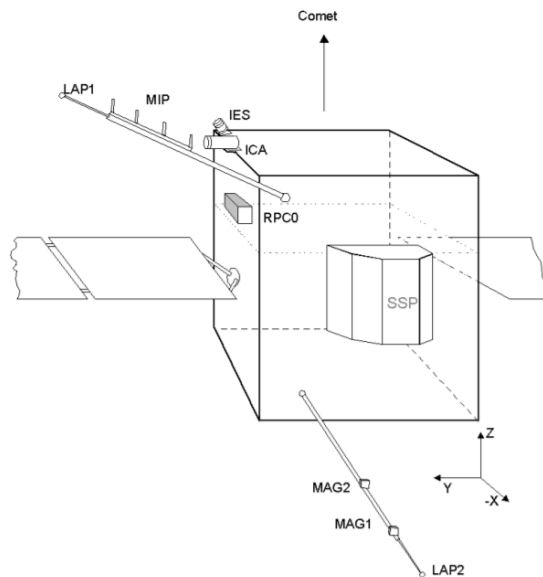


Figure 3.2. The RPC instruments on the Rosetta spacecraft in the spacecraft coordinate system (x, y, z): Ion Composition Analyser (ICA), Ion and Electron Sensor (IES), Langmuir Probes (LAP1 and LAP2), Fluxgate Magnetometers (MAG1 and MAG2), and Mutual Impedance Probe (MIP), the RPC electronics box (RPC0) and the Surface Science Package (SSP). Source: Eriksson et al. (2007).

3.2.1 Coordinate systems

To describe the comet - solar wind interaction region observed by instruments onboard the Rosetta spacecraft, several coordinate systems have been proposed. In this work, both the spacecraft-centered (s/c) and the comet-centered solar equatorial (CSEQ) coordinate systems are used. The CSEQ coordinate system is centred in the comet. x_{CSEQ} points towards the sun, z_{CSEQ} is perpendicular to the solar equatorial plane, whilst y_{CSEQ} completes the frame. The s/c coordinate system origins in the spacecraft. Its y-axis is along the solar panels such that $y_{s/c}$ is nearly always perpendicular to the spacecraft - Sun direction. $z_{s/c}$ points towards the nominal comet direction, and $x_{s/c}$ completes the system. Thus $x_{s/c}$ does not necessarily point in the Sun direction. The components of the two frames are illustrated in Figure 3.3(a). Note, that since the Rosetta spacecraft has been mostly in front of the comet (positive x_{CSEQ}), x_{CSEQ} and $x_{s/c}$ might not be strictly parallel.

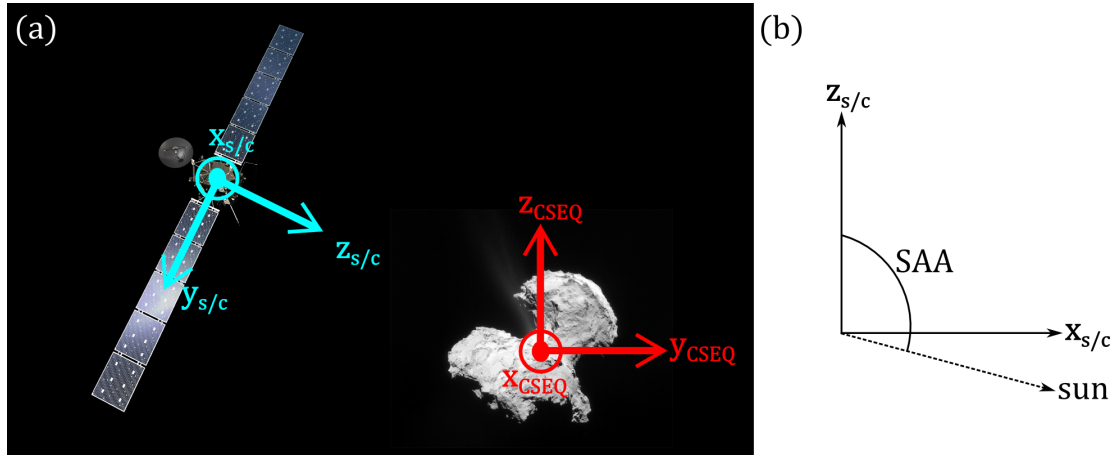


Figure 3.3. (a) Spacecraft (s/c) and comet-centered solar equatorial (CSEQ) coordinate systems. The Sun is located out of the paper. Illustrations from ESA:flickr and NAVCAM. (b) Definition of the solar aspect angle (SAA) in the spacecraft frame.

The booms that carry LAP1 and LAP2 are mounted on the $-x$ surface of the spacecraft body (PDS, March 11, 2017). This means that the probes are at risk of being shadowed by either the solar panels, the spacecraft body itself, or the high gain antenna that sends data to Earth. Whether the probes are in shadow is described by the solar aspect angle (SAA) illustrated in Figure 3.3(b) (e.g. Eriksson et al., 2010). In Johlander (2012), the SAA is defined as the angle between $x_{s/c}$ and the solar pointing direction in the spacecraft frame. However, to follow the European Space Agency usage this work uses the convention that the SAA is the angle from the Sun's position vector to $z_{s/c}$. LAP2 is then shaded if $18^\circ < SAA < 82^\circ$, might be shaded or partially shaded by the high gain antenna for $82^\circ < SAA < 107^\circ$, and is illuminated otherwise.

3.2.2 Langmuir Probes (LAP)

The LAP instrument consists of two spherical Langmuir probes, LAP1 and LAP2, of radius 2.5 cm. The probes are attached at the end of booms of length 2.24 m and 1.62 m, respectively, on the anti-sunward side of the spacecraft (see Figure 3.2), and are separated by a distance of 5.00 m (Eriksson et al., 2007).

Since the probes are not located at the same point relative to the spacecraft body, they might experience different sheath effects from the spacecraft.

By operating the LAP instrument in different modes, estimates of various plasma parameters and the electric field can be obtained. The modes of the LAP instrument are described in depth by Eriksson et al. (2007). The bias voltage sweep requires one probe and gives an estimate of the electron number density, electron temperature, and spacecraft potential by measuring the voltage dependence of the current collected by the probe, whilst the electric field mode is a dual probe experiment estimating the electric field fluctuations in-between the probes. The electric field mode is the most important tools in this work and will be discussed in detail after a general introduction to Langmuir probes.

General Principles Behind Langmuir Probes

A Langmuir probe is a metallic electrode usually in the shape of a sphere or a cylinder (see Schott (1968) and Chen (1965) for thorough descriptions). The most widely used feature of Langmuir probing is the current-voltage $I - V$ characteristics, where the total current from the probe is measured over a bias range. Consider both an infinitely large planar probe and a spherical one. Figure 3.4 shows typical responses of the currents when the probe is biased relative to the plasma.

When no bias is applied, the probe is at its floating potential V_f . After having reached equilibrium, all electrons, apart from an electron flux equal to the ion flux, are repelled from the probe surface, and the collected current is thus zero. This is similar to the generation of the spacecraft sheath, described in Section 3.1, and the previously termed spacecraft potential $V_{s/c}$ is hence the floating potential of the spacecraft.

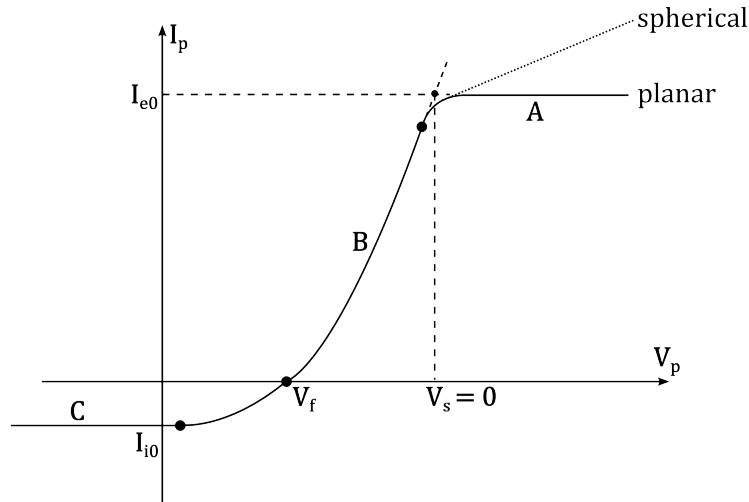


Figure 3.4. Typical current (I_p) - voltage (V_p) characteristics of both an infinitely large planar electric probe and a spherical probe in a closed plasma environment. The three characteristic intervals are the electron saturation region (A), where the current to the probe is the electron saturation current I_{e0} , the transition region (B), and the ion saturation region (C), where the probe current is the ion saturation current I_{i0} . The plasma or space potential V_s is defined here as zero, whilst the floating potential V_f is reached when the net current to the probe is zero. Note for clarity, that the origin of the y-axis is at a negative potential.

When there is no potential difference between the probe and the surrounding medium, that is when $V_p = V_s = 0$, the charged plasma particles will not be either electrically attracted to or repelled by the probe. However, the thermal velocities of the particles causes a current to the probe. Since the thermal speed of a particle of thermal energy $k_B T$ and mass m is given by

$$u_{th} = \sqrt{\frac{2k_B T}{\pi m}} \quad (3.5)$$

The lighter electrons usually have larger thermal velocities than the heavy ions (Schott, 1968). This yields that when the probe is biased at the potential of the plasma, i.e. the space potential V_s , it is placed in, the majority of particles migrating to the probe is electrons, which gives rise to a net electron current.

Increasing the probe voltage relative to the space potential (region A in Figure 3.4) attracts electrons to the probe and hence increases the electron current collected by the probe. Furthermore, the ions are repelled by the positively bias probe. This leaves an excess of electrons, a sheath, near the probe surface. The sheath builds up until the negative charge of the sheath equals the positive charge of the probe. The current collected by the probe is proportional to the net flux of electrons entering this sheath, and is hence proportional to the surface area of the sheath. For an infinitely planar, the sheath surface area is invariant to its thickness, causing an electron saturation current I_{e0} as shown in part A. For a spherical probe, the flux area changes as the sheath thickness changes, causing a constant increase in the collected electron current with increased probe potential (Chen, 1965).

Decreasing the probe potential below the probe floating potential leads to the generation of an ion sheath (C in Figure 3.4) similar to the electron sheath generated for probe potentials greater than V_s . There are, however, a few asymmetries related to the electron and ion saturation currents, caused by the mass and temperature differences between the two species (usually $T_i \ll T_e$) (Chen, 1965). In addition, if the probe is sunlit, emission of electrons from the probe surface will give rise to a photoemission current towards the probe.

To a biased spherical probe with a small radius a compared to the plasma Debye length, the total current can be described by the orbital-motion-limited current collection model as the sum of contributing currents (Laframboise). The model takes into account that in the case of a thick sheath, not all charged particles entering the sheath reach the probe due to the possibility of orbital motion (see e.g. Figure 3 in Schott (1968)). In space plasmas, where the Debye length might be several metres (Blandford and Thorne, 2013), a probe of a few centimetres radius will be governed by this model. The current collected by a probe at potential V_p is then modelled as the sum of the photoemission current I_{ph} , ion current I_i , and electron current I_e , given by the formulas (see e.g. Eriksson et al., 2017):

$$I_{ph} = \begin{cases} -I_{ph0}, & V_p < 0 \\ -I_{ph0} \exp\left[-\frac{eV_p}{k_B T_{ph}}\right], & V_p > 0 \end{cases} \quad (3.6)$$

$$I_i = \begin{cases} -I_{i0} \left(1 - \frac{eV_p}{E_i}\right), & V_p < E_i/e \\ 0, & V_p > E_i/e \end{cases} \quad (3.7)$$

$$I_e = \begin{cases} I_{e0} \exp\left[\frac{eV_p}{k_B T_e}\right], & V_p < 0 \\ I_{e0} \left(1 + \frac{eV_p}{k_B T_e}\right), & V_p > 0 \end{cases} \quad (3.8)$$

where $E_i = m_i u_d^2 / 2$ is the drift energy of the ions, and $k_B T_e$ is the thermal energy of the electrons. Eq. (3.6) assumes a Boltzmann distribution of characteristic energy $k_B T_{ph}$ and an isotropic photoelectron distribution at the surface, whilst Eq. (3.7) assumes that the ions are single-charged and have a negligible thermal speed relative to the plasma flow (Eriksson et al., 2017). In the solar wind case, this is a reasonable assumption, since the solar wind is highly dominated by He-ions that with a thermal energy of 1 eV (Pröls, 2010) have thermal speeds of $u_{th} = 7.8$ km/s which is far less than the typical solar wind speed of 400 km/s.

In Eq. (3.6), (3.7), and (3.8), I_{ph0} , I_{i0} , and I_{e0} denote the photoemission saturation current, the ram ion current at $V_p = 0$, and the random electron motion current (see Figure 3.4). The photoemission saturation current is dependent on the size of the illuminated area, as well as the probe material and solar radiation, whilst the electron saturation current for a spherical probe of surface area $A_e = 4\pi a^2$ is given by

$$I_{e0} = A_e n_e e \frac{k_B T_e}{2\pi m_e} \quad (3.9)$$

and the ram ion current is

$$I_{i0} = n_i e u_d A_i \quad (3.10)$$

where $A_i = \pi a^2$ is the probe surface projected to the flow direction.

Figure 3.5 shows an example of the total current $I_{tot} = I_{ph} + I_i + I_e$ computed from Eq. (3.6), (3.7), and (3.8). The used parameters resemble the He dominated solar wind at a heliocentric distance of 3 AU with a drift speed of $u_d = 400$ km/s, plasma density 1 cm^{-3} , and thermal energy of 1 eV, measured by a spherical probe of radius 2.5 cm (inspired by Eriksson et al. (2017)). These values yield a Debye length (see Eq. (2.11)) of $\lambda_D = 7.4$ m. Hence, the probe radius is much smaller than the Debye length, and the current to the probe can be estimated by the orbital-motion-limited current collection model of Eq. (3.6), (3.7), and (3.8). For this case, E_i/e is an enormous number, and $V_p < E_i/e$ is satisfied throughout the entire domain.

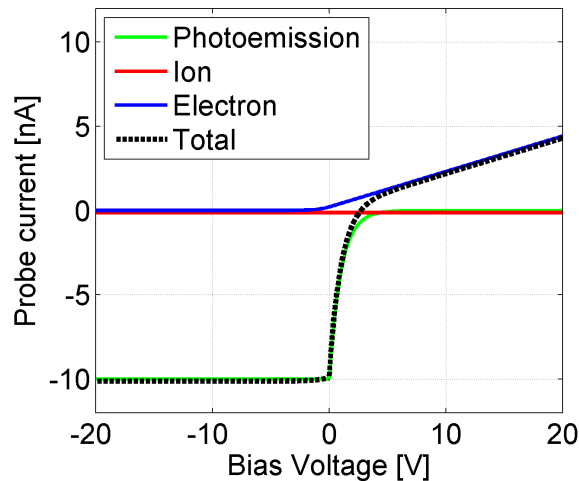


Figure 3.5. Theoretically computed photoemission, ion, and electron currents plotted together with the total probe current for a Langmuir probe voltage sweep for typical solar wind condition 3 AU from the Sun. Note that in the plot the electron current is positive, and that ion current is non-zero, but small compared to the electron and photoemission currents. The space potential is defined as zero. Used parameters: $u_d = 400$ km/s, $n = 1 \text{ cm}^{-3}$, $a = 2.5$ cm, $m_i = 1$ amu, $I_{ph0} = 10$ nA, $k_B T_{ph} = 1$ eV, and $k_B T_e = 1$ eV.

For $V_p < 0$, the total current to the probe in Figure 3.5 is mainly determined by the photoemission current, whilst the dominating contributor for $V_p > 0$ is the electron current. For positive probe potentials, the photoemission current becomes negligible due to the attractive force between the electrons and the probe.

In the current bias mode of the LAP instrument, a sum of Eq. (3.6), (3.7) and Eq. (3.8) can be fitted to the $I - V$ characteristics to extract information about the electron density and temperature (Eriksson et al., 2017). Hence, LAP is a versatile instrument that can provide plasma measurements as well as the electric field estimates introduced below.

Electric Field Mode

The electric field mode of the LAP instrument estimates the electric field between LAP1 and LAP2. In this mode, either a controlled bias current is or is not applied to the system. The potentials between the spacecraft and each of the probes, V_1 and V_2 , are measured. From these, the electric field is estimated as

$$E = \frac{V_2 - V_1}{d_{12}} \quad (3.11)$$

where d_{12} is the probe separation of 5.00 m. The electric field mode has a low-frequency continuous data sampling and a high-frequency wave snapshot sampling. The former measures in intervals of 1798 samples with a sampling frequency of 57.8 Hz, giving continuous data sampling in intervals of roughly 31.1 s. The low-frequency sampling is followed by a data gap of roughly 1 s during which the snapshot sampling makes 432 samples with a sampling frequency of 18.75 kHz, lasting for roughly 23 ms.

The potentials V_1 and V_2 are measured relative to the spacecraft body, and hence provide an estimate of variations in the spacecraft potential $V_{s/c}$ (Karlsson et al., 2017). However, since the Debye length is often of the order of meters, the probes are usually measuring the plasma within the sheath. Figure 3.6 phenomenologically illustrates the simplified radial potential profile of the spacecraft sheath and its consequences for the measured probe potentials. Here a spacecraft and a probe are placed in a plasma

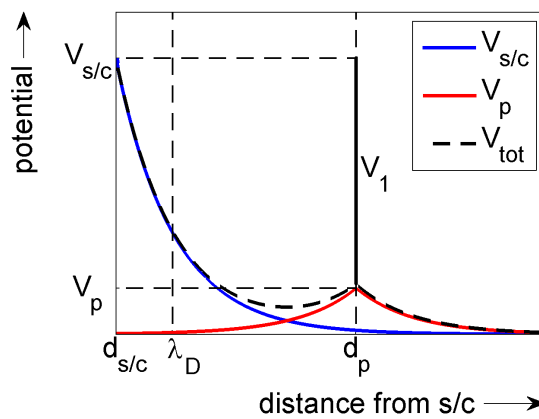


Figure 3.6. Potential structure in sheath generated by intrusion of spacecraft and Langmuir probe in space plasma of Debye length λ_D . The spacecraft is at position $d_{s/c}$ and is at its floating potential $V_{s/c}$ relative to the plasma, whilst the probe is at location d_p and is at floating potential V_p relative to the plasma. The potential difference measured between the probe and spacecraft is $|V_1| < |V_{s/c}|$. Note that in this figure, the spacecraft potential is displayed as positive, which is not the case for the considered event dates in Chapter 4.

of Debye length λ_D , such that the spacecraft and probe potentials, $V_{s/c}$ and V_p , are caused by electron (and ion) migration to the surfaces and photoemission current off the surfaces. Throughout the generated sheath, both potentials go off exponentially with d/λ_D (see Eq. (3.4)), and at any point, in the sheath, the total potential relative to the undisturbed plasma equals the sum of the potential profiles caused by the presence of the spacecraft and the probe. The result is that the potential difference between the probe and the spacecraft is only a fraction of the negative of the full spacecraft potential, as stated above.

During the electric field mode sampling of the LAP instrument, the $I - V$ characteristics cannot be obtained simultaneously. Hence, information about the electron density and temperature is lost, whenever the probes are in electric field mode. However, a change in V_1 and V_2 measured during the electric field mode might give information about variations in the electron density (Karlsson et al., 2017), since changing electron densities results in a different Debye length and spacecraft potential. The latter is seen by considering the equations studied by Odelstad et al. (2015). They investigate the relation between changes in the spacecraft potential and electron density by considering the current to the probe due to electrons being repelled from a negatively biased spacecraft. By combining Eq. (3.8) and (3.9) for the entire spacecraft of current collecting area $A_{s/c}$ and potential $V_{s/c}$ and recognising the thermal speed of the electrons as $u_{th} = \sqrt{2k_B T_e / \pi m_e}$ (see Eq. (3.5)), the electron current becomes

$$I_e = A_{s/c} n_e e \frac{u_{th}}{2} \exp \left[\frac{e V_{s/c}}{k_B T_e} \right] \quad (3.12)$$

Eq. (3.6) states that the photoemission current I_{ph} is independent of the spacecraft potential for a negatively charged spacecraft off the spacecraft, i.e. $I_{ph} = -I_{ph0}$. Recall that the spacecraft potential is actually the floating potential of the spacecraft, and that it is defined as the point where the net current to the spacecraft is zero. Assuming that the entire current to the spacecraft is given by the electron and photoemission currents, i.e., $I_e = I_{ph}$, yields

$$V_{s/c} = -\frac{k_B T_e}{e} \log \left[\frac{A_{s/c} n_e e u_{th}}{2 I_{ph0}} \right] \quad (3.13)$$

Hence, $V_{s/c}$ is directly dependent on the electron temperature T_e and density n_e . By assuming constant temperature T_e , Eq. (3.13) states that an increase in $V_{s/c}$ corresponds to a decrease in n_e and vice versa.

Since the probe potentials are measured relative to the spacecraft, V_1 and V_2 , they give a measure of the negative of $V_{s/c}$. Hence, for a negatively charged spacecraft, an increase in the potentials measured at LAP1 and LAP2 might correspond to a decrease in $V_{s/c}$ and ultimately to an increase in electron density.

To directly compare the fluctuations in probe potentials to electron density variations by Eq. (3.13), it must be assumed that the ratio between the probe potential and spacecraft potential, i.e., $V_1/V_{s/c}$, stays constant throughout the studied time interval. This might not be entirely true, since if the electron density is increased, Eq. (3.13) gives that the magnitude of the spacecraft potential relative to the space potential increases, as well. In addition, the Debye length decreases, which ultimately alters the influence of the presence of the spacecraft body on the probe potentials. This means that one has to be careful when quantitatively interpreting an increase or decrease in the probe potentials as changes in the electron density, since changes in the measured potentials are caused by both changes in the fraction between V_1 and $V_{s/c}$, themselves, related to changes in the electron density and temperature, in addition to possible variations in the probe illumination.

Electric Probe Calibration

When the LAP instrument is in electric field mode, the measured quantities are the probe potentials of LAP1 and LAP2 relative to the spacecraft. From the potentials V_1 and V_2 the electric field is estimated, as described in above. Since the distance between the probes is short, LAP1 and LAP2 are expected to be in similar environments, and that on average $V_1 = V_2$ (Dickeli, 2016). However, due to slightly different boom lengths, this is not entirely true. Instead, there often is a shift in V_2 relative to V_1 . To overcome this shift, the probes are calibrated by equalling the means of the potentials in a chosen time interval, such that V_2 is translated into a system where the linear regression $V_2 = b_1 V_1 + b_2$ has the values $b_1 = 1$ and $b_2 = 0$.

In this work, the least-squares method is implemented as a linear regression tool when calibrating the probe potentials. The method fits a straight line $y = b_1 x + b_2$ to the data points (x_1, y_1) , (x_2, y_2) , \dots , (x_n, y_n) , such that the sum of the squares of the distances measured in the y -direction between each data point and the line is minimized (Kreyszig, 2011). The vertical distance between a data point (x_i, y_i) and the related point on the line $(x_i, b_1 x_i + b_2)$ is $|y_i - (b_1 x_i + b_2)|$, and hence the sum of the squares of the distances is given by

$$s = \sum_{i=1}^n (y_i - b_1 x_i - b_2)^2 \quad (3.14)$$

Since s is a function of b_1 and b_2 , it must be minimized in both of these. Differentiating s with respect to each of these then gives the equations from which b_1 and b_2 can be determined. That is,

$$\begin{aligned} \frac{\partial s}{\partial b_1} &= -2 \sum x_i (y_i - b_1 x_i - b_2) = 0 \\ \frac{\partial s}{\partial b_2} &= -2 \sum (y_i - b_1 x_i - b_2) = 0 \end{aligned} \quad (3.15)$$

where the summation index $i = 1, \dots, n$ has been omitted. Rearranging the sums in Eq. (3.15), gives the relations

$$b_1 \sum x_i^2 + b_2 \sum x_i = \sum x_i y_i \quad (3.16)$$

$$b_1 \sum x_i + b_2 n = \sum y_i \quad (3.17)$$

The slope b_1 and intersection with the y -axis b_2 are found by solving the above system of equations. This gives

$$\begin{aligned} b_1 &= \frac{n \sum x_i y_i - \sum x_i \sum y_i}{n \sum x_i^2 - (\sum x_i)^2}, & \text{slope} \\ b_2 &= \frac{1}{n} \left(\sum y_i - b_1 \sum x_i \right), & \text{intersection with } y\text{-axis} \end{aligned} \quad (3.18)$$

The slope and intersection with the y -axis of the fitted line is then used to translate the data points into calibrated data where a linear regression has a slope of 1 and goes through the origin of the (x, y) -system. The translation of the raw data is done by dividing all points in V_2 by the slope b_1 of the straight line related to the uncalibrated data. Finally, the intersection constant of this semi-calibrated potentials is subtracted from all translated V_2 data points, generating the calibrated data.

Figure 3.7 shows an example of the probe calibration for a 40 min interval on October 25, 2015. This date contains low-frequency wave-activity studied by Karlsson et al. (2017) with the LAP instrument in E-field mode.

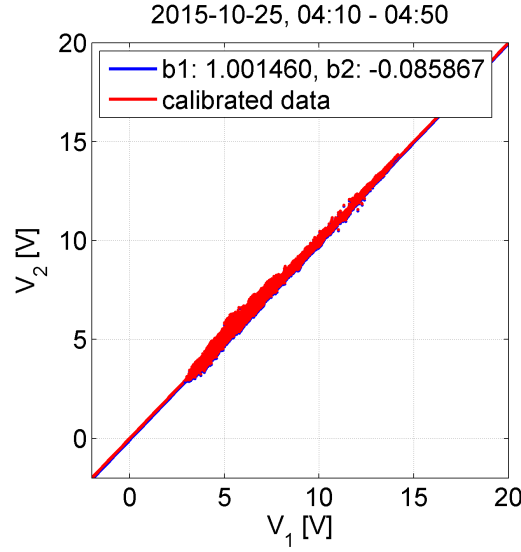


Figure 3.7. Example of probe calibration in which the probe data (blue) is calibrated (red) to make the linear regression go through (0,0) with a slope of 1. Data from October 25, 2015, at 04:10 - 04:50 UT.

In this work, a least-squares method is also used to estimate the frequency-PSD power-law relation of the electric and magnetic fields. This is done by fitting a straight line to the data in double-logarithmic space. The coefficient of determination R^2 of the regression gives a measure of how well the model accounts for the variability of the fitted data (Olofsson and Andersson, 2012). It is computed from the linear regression values \hat{y} , data points y_i and data point mean $\langle y \rangle$ by

$$R^2 = 1 - \frac{\sum_{i=1}^n (y_i - \hat{y}_i)^2}{\sum_{i=1}^n (y_i - \langle y \rangle)^2} \quad (3.19)$$

The numerator of the fraction gives the deviation (the residuals) of the linear regression from the data, whilst the denominator gives the difference from the mean and hence the total variation of the data. Both sums are positive, and since the total variation of the data from the mean is larger than the variation from the estimated fit, R^2 will be a number between 0 and 1. A large value of R means that the model predicts well the data, and hence the best fit is achieved for $R^2 = 1$.

Transformation of spacecraft data into electric field system

Since the LAP instrument consists of only two probes between which the electric field is estimated, the electric field estimate is one dimensional. To compare this to the three-dimensional magnetic field measured by the MAG instrument (see next section), the magnetic field components can be translated from the spacecraft coordinate system into a system where one component is parallel to the electric field estimate and the others are perpendicular. This system will from now on be termed the "electric field coordinate system". The coordinates of LAP1 and LAP2 in the spacecraft coordinate system are given in Table 3.1 together with the normalized coordinates of the electric field estimate.

The values in Table 3.1 give the transformation of the electric field coordinate from the electric field system (where the electric field is in the $e_1 = [1, 0, 0]$ -direction) into the spacecraft system. The first perpendicular coordinate of the electric field system is arbitrarily chosen as the cross-product of the electric field coordinate with the unit vector $\mathbf{u}_1 = [1, 0, 0]$ in the spacecraft system. The last coordinate

Table 3.1. Spacecraft coordinates of LAP1, LAP2 and the electric field unitvector (PDS, March 11, 2017).

	x [m]	y [m]	z[m]
LAP1	-1.19	2.43	3.88
LAP2	-2.48	0.78	-0.65
E-field	-0.26	-0.33	-0.91

of the electric field system completes the system, such that the transformation into the spacecraft system of the electric field basis $\{\mathbf{e}_1, \mathbf{e}_2, \mathbf{e}_3\}$ in electric field coordinates is given by

$$\mathbf{P} = [T(\mathbf{e}_1) \ T(\mathbf{e}_2) \ T(\mathbf{e}_3)] = \begin{bmatrix} -0.26 & 0 & 0.97 \\ -0.33 & 0.94 & -0.09 \\ -0.91 & -0.34 & -0.24 \end{bmatrix} \quad (3.20)$$

The transformation \mathbf{x} into the spacecraft system of an element \mathbf{y} in the electric field system is then given by (see e.g. Lay (2014)):

$$\mathbf{x} = \mathbf{P}\mathbf{y} \quad (3.21)$$

yielding that to transform a signal \mathbf{x}_s from spacecraft coordinates to electric field coordinates, the inverse of the matrix \mathbf{P} is applied to the signal such that

$$\mathbf{y}_s = \mathbf{P}^{-1}\mathbf{x}_s \quad (3.22)$$

Using this on the three-component magnetic field in the spacecraft-centered coordinate system, results in the vector $\mathbf{B} = (B_1, B_2, B_3)$, where B_1 , B_2 , and B_3 are the components parallel and perpendicular to \mathbf{e}_1 that gives the direction of the electric field estimate.

3.2.3 Fluxgate Magnetometer (MAG)

The MAG instrument consists of two fluxgate magnetometer sensors, MAG1 and MAG2, mounted on the same boom as LAP2 (see Figure 3.2) and separated by a distance of 15 cm (Glassmeier et al., 2006). In normal mode, MAG has a sampling frequency of 1 Hz, whilst the burst mode is 20 Hz, giving a bandwidth of 0 - 10 Hz. However, Glassmeier et al. (2006) note that the reaction wheels onboard the Rosetta spacecraft cause interference in the magnetic field at frequencies above 1 Hz. The signature is easy to detect in the magnetic field spectrogram, as will be illustrated in the results and discussion chapter of this work.

Unknown magnetic field sources from the spacecraft might cause an offset in the magnetic field components (Goetz et al., 2016a). A natural calibration to remove this offset from the magnetic field follows from diamagnetic cavity crossings, where all magnetic field components go to zero (see Section 2.4.3). From this, the components can be calibrated by subtracting the means of each of the three components during the cavity from the entire time interval. Figure 3.8 shows the effect of this calibration method on the cavity crossing studied by Goetz et al. (2016a). The event consists of the cavity limited by the contact surface outside which the magnetic field magnitude gradually decreases in the diamagnetic cavity boundary layer. Additional information about the structure of the cavity can be obtained by studying the orientation of the boundaries. This can be done by the minimum variance analysis (MVA). The method gives an estimate of the boundary normals by considering the variance of the magnetic field components, and hence provides an idea about the spatial structure of the diamagnetic cavity.

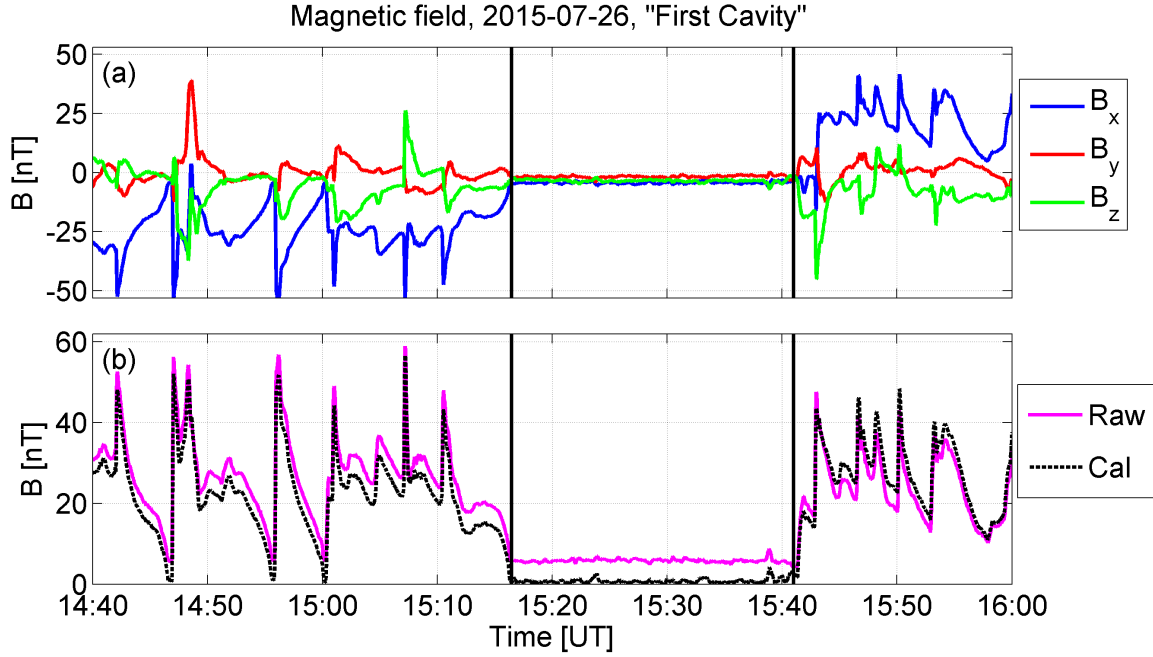


Figure 3.8. Magnetic field during diamagnetic cavity crossing on July 26, 2015. The cavity is between the vertical black lines from 15:16 - 15:41 UT. The magnetic field components, B_x , B_y and B_z are given in the CSEQ coordinate system and have not been calibrated. In the lower plot, the dashed magenta line is the magnetic field magnitude computed from the un-calibrated components, whilst the dashed black curve gives the magnetic field magnitude of the calibrated components.

Minimum Variance Analysis (MVA)

From a single spacecraft crossing a plasma boundary in a space, the MVA of the three-component magnetic field data provides an estimate of the normal \mathbf{n} to a boundary. It originates in the divergence-free magnetic field ($\nabla \cdot \mathbf{B} = 0$) and the assumption of a one-dimensional boundary. In this idealized case, the component of the magnetic field normal to an infinitely thin transition layer is constant throughout the layer, i.e. $\mathbf{B} \cdot \mathbf{n} = \text{const.}$ (Sonnerup and Cahill, 1967). Applying this to a spacecraft boundary crossing consisting of a number of magnetic field measurements $\mathbf{B}^{(i)}$, gives that the normal is in the direction where $\mathbf{B}^{(i)} \cdot \mathbf{n}$ deviates as little as possible from the average value $\langle \mathbf{B} \rangle \cdot \mathbf{n}$ (Sonnerup and Screible, 2000).

Consider a 3-D dataset of N magnetic field measurements $\mathbf{B} = (\mathbf{B}^{(1)} \mathbf{B}^{(2)} \dots \mathbf{B}^{(N)})^T$ with spatial directions (x, y, z) . Assume that the data is achieved from a spacecraft crossing of a transition layer. The aim is now to find the normal to the layer. The variance σ^2 of the difference $(\mathbf{B}^{(i)} \cdot \mathbf{n} - \langle \mathbf{B} \rangle \cdot \mathbf{n})$ is defined as

$$\sigma^2 = \frac{1}{N} \sum_{i=1}^N |(\mathbf{B}^{(i)} - \langle \mathbf{B} \rangle) \cdot \mathbf{n}|^2 \quad (3.23)$$

where the averaged value of the N measurements of each of the components in the magnetic field $\langle \mathbf{B} \rangle = \langle [\mathbf{B}_x \mathbf{B}_y \mathbf{B}_z] \rangle$ is given by

$$\langle \mathbf{B} \rangle = \frac{1}{N} \sum_{i=1}^N \mathbf{B}^{(i)} \quad (3.24)$$

The normal is subject to the constraint $|\mathbf{n}|^2 = 1$, and hence the problem of finding the minima of σ^2 can be dealt with by introducing a Lagrange multiplier λ . Now, the problem reduces to solving the vector equation

$$\nabla_{n_x, n_y, n_z} \left(\sigma^2 - \lambda (|\mathbf{n}|^2 - 1) \right) = \mathbf{0} \quad (3.25)$$

The differentiation of the three equations in Eq. (3.25) leads to the eigenvalue problem (Sonnerup and Screible, 2000):

$$\sum_{j=1}^3 \mathbf{M}_{ij} \mathbf{n}_j = \lambda_j \mathbf{n}_i \quad (3.26)$$

where \mathbf{M} is the symmetric magnetic variance matrix with elements given by

$$\mathbf{M}_{ij} = \langle B_i B_j \rangle - \langle B_i \rangle \langle B_j \rangle \quad (3.27)$$

Eq. (3.26) can now be solved to find the three eigenvectors \mathbf{n}_1 , \mathbf{n}_2 and \mathbf{n}_3 with corresponding eigenvalues $\lambda_1 \leq \lambda_2 \leq \lambda_3$ in the measurement frame of reference (x, y, z) .

When translating \mathbf{B} into the eigenvector frame where the eigenvectors are expressed as $\mathbf{n}_1 = (1, 0, 0)$, $\mathbf{n}_2 = (0, 1, 0)$ and $\mathbf{n}_3 = (0, 0, 1)$, the symmetric magnetic variance matrix becomes diagonal. The diagonal entries of the matrix are the eigenvalues of the system (Narita, 2012). Since the elements of \mathbf{M} are given as the variance of the magnetic field (see Eq. (3.27)), it is evident that the eigenvalues are indeed the variance of the magnetic field in the directions parallel to the eigenvectors. Hence, the eigenvector corresponding to the lowest eigenvalue gives the direction of the minimum variance, i.e. the normal to the boundary. Due to orthogonality of the eigenvectors, the remaining ones are transverse to the boundary.

Test of Minimum Variance Analysis on First Detection of Diamagnetic Cavity

The implementation of the MVA method presented above is able to reproduce results from previous studies. To illustrate this, the diamagnetic cavity crossing observed in the MAG instrument on July 26, 2015, and studied by Goetz et al. (2016a) is here analysed by the presented MVA method.

The magnetic field data used for the computation of the boundary normals is presented in Figure 3.8. It has a sampling frequency of 1 Hz, and is "cavity calibrated" by removing the mean of each magnetic field component within the cavity from the entire dataset. The intervals across which the direction of minimum variance is determined are the boundary crossing intervals determined by Goetz et al. (2016a), i.e. 15:14:40 - 15:16:30 UT for the inbound crossing and 15:41:10 - 15:42:00 UT for the outbound. The boundary normals computed in this work are denoted \mathbf{v}_{in} and \mathbf{v}_{out} , whilst the normals obtained by Goetz et al. (2016a) are denoted \mathbf{n}_{in} and \mathbf{n}_{out} . Their coordinates in the CSEQ frame are given in Table 3.2, together with the angular difference of \mathbf{v}_{in} to \mathbf{n}_{in} and \mathbf{v}_{out} to \mathbf{n}_{out} in the $x-y$ and in the $x-z$ planes of the CSEQ systems.

Table 3.2. Comparison of the boundary normals presented in Goetz et al. (2016a) (\mathbf{n}_{in} and \mathbf{n}_{out}) with the normals computed in this work (\mathbf{v}_{in} and \mathbf{v}_{out}) for a cavity crossing on July 26, 2015, over shown time intervals. Θ_{xy} and Θ_{xz} indicate the angle between the two boundary normals in the $x-y$ and $x-z$ plane of the CSEQ system, respectively.

Time interval [UT]	s/c position [km] (x, y, z)	\mathbf{n}_{in} & \mathbf{n}_{out} (x, y, z) (Goetz et al., 2016a)	\mathbf{v}_{in} & \mathbf{v}_{out} (x, y, z) (This study)	Θ_{xy}	Θ_{xz}
15:14:40 - 15:16:30	(-0.1, -99.1, -138.5)	(-0.13, 0.53, 0.84)	(-0.15, 0.45, 0.88)	5.07°	1.17°
15:41:10 - 15:42:00	(-0.1, -98.3, -139.0)	(-0.29, 0.82, 0.5)	(-0.31, 0.82, 0.48)	1.25°	2.57°

The differences in the normals are minimal and might be caused purely by slight differences in the calibration level of the used data. Figure 3.9 graphically depicts the similarity between the normals in both the $x-y$ and $x-z$ planes of the CSEQ coordinate system. The normals are shown together with the average magnetic field direction before (14:40:00 - 15:14:40 UT) and after (15:42:00 - 16:00:00 UT) the cavity.

The normal vectors \mathbf{n}_{in} and \mathbf{n}_{out} do not change significantly from the inbound boundary to the outbound. This yields that the surfaces of the boundaries are close to parallel, even though the characteristics of the boundaries differ from each other in terms of time-scales (see Figure 3.8 and first column of Table 3.2). The study, in addition, shows that the averaged magnetic field has reversed after the cavity relative to before (as mentioned in Section 2.4.3). The implementation of the MVA method and computation of mean magnetic fields before and after the cavity crossing in this work show the same features and do well in reproducing the results of the cavity crossing. This indicates that the implementation of the method is able to produce reliable results that are in agreement with findings of published studies.

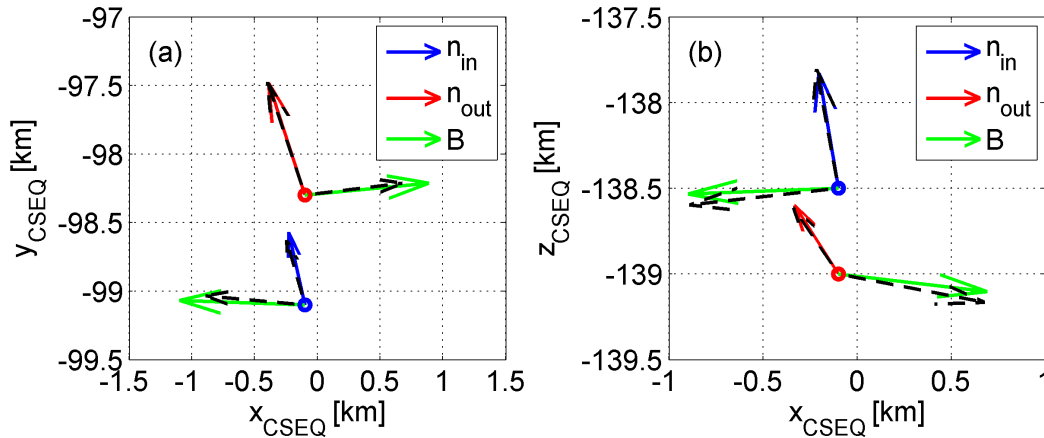


Figure 3.9. Normals for the inbound (\mathbf{n}_{in}) and outbound (\mathbf{n}_{out}) boundaries and averaged magnetic field direction $\mathbf{B}/|\mathbf{B}|$ before and after the diamagnetic cavity, presented by Goetz et al. (2016a). These are shown together with the normals and averaged magnetic field directions (dashed black arrows) computed in this work. Note that the plots show the vectors in the $x-y$ (a) and $x-z$ (b) planes of the CSEQ coordinate system.

3.2.4 Supporting instruments: ICA, IES, MIP and ROSINA-COPS

The Ion Composition Analyser (ICA), Ion and Electron Sensor (IES), and Mutual Impedance Probe (MIP) of the RPC are other plasma instruments designed to investigate the plasma environment encountered by the Rosetta spacecraft. ICA and IES estimate the energy spectrograms and three dimensional distribution functions of ions and both ions and electrons, respectively, whilst MIP estimates the electron density from measurements of the plasma frequency. Whenever possible, ICA, IES, MIP, and ROSINA-COPS that provides an estimate of the neutral density are included in the event analysis of Chapter 4 to support the finding of the LAP and MAG instruments.

In the results and data analysis chapter, the calibration and main analysis of the ICA, IES, MIP, and ROSINA-COPS measurements for the studied events are carried out by the individual teams and provided for this work. This is why only a brief introduction to the aims and principles of the three instruments are given in this section. Thorough descriptions of the instruments can be found in Nilsson et al. (2007) for ICA, Burch et al. (2006) for IES, Trotignon et al. (2007) for MIP, and Balsiger et al. (1998) for ROSINA-COPS. The expected time resolutions, field-of-views, and measurement ranges of the ICA, IES, and MIP instruments are summarized in Table 3.3. However, during real measurements, the field of views might be smaller (Nilsson et al., 2007).

Table 3.3. Time resolutions, field of views, and measurement ranges of the ICA, IES, and MIP instruments (Nilsson et al., 2007; Burch et al., 2006; Trotignon et al., 2007). Note that both the range of the electron density and temperature measurements are shown for the MIP instrument.

	ICA	IES	MIP
Time resolution	12 s (2D) 192 s (3D)	128 s	8 s (normal) 2.5 s (burst)
Field of view	$90^\circ \times 360^\circ$	$90^\circ \times 360^\circ$	—
Range	25 eV - 40 keV	1 eV - 22 keV	$2\text{ cm}^{-3} - 1.5 \times 10^5\text{ cm}^{-3}$ 30 K - 10^6 K
Resolution	$\Delta E/E = 7\%$	$\Delta E/E = 4\%$	5% (density) 10% (temperature)

MIP and ROSINA-COPS

The MIP instrument makes use of natural the plasma frequency of Eq. (2.12). This is done by measuring the voltage difference V between two probes when an alternating current I is applied to the system. The frequency dependence of the mutual impedance $Z = V/I$ can then be used to determine the plasma frequency. Due to the direct relation between the electron density n_e and plasma frequency (recall $\omega_p = \sqrt{n_e e^2 / m_e \epsilon_0}$), the electron density can be deduced rather accurately from this.

ROSINA-COPS can estimate the cometary neutral gas density and velocity. This instrument consists of two pressure gauges. One of them measures the total pressure, whilst the other measures the dynamical pressure in the ram direction (Balsiger et al., 1998). From the total pressure, the local density of the neutral gas can be derived, whilst the dynamical pressure gives an estimate of the flux of cometary neutral, from which the neutral velocity can be estimated.

ICA and IES

Charged particles accepted into the ICA or IES instruments initially encounter the electrostatic analyser (ESA). The ESA lets in only particles within a specific energy range, by applying an electrostatic field that separates the particles according to their kinetic energy. In the IES instrument, charged particles hit a microchannel plate where the energy per charge ratios of the particles are detected. On the other hand, ions passing through the ESA of the ICA instrument enter a mass analyser. Here a cylindrical magnetic field sustained by permanent magnets deflects the ions with an angle dependent on the mass-to-charge ratio of the particles. This means that IES does not discriminate in mass, but ICA does.

The ICA and IES instruments are able to distinguish between different ion species with sufficiently different mass-to-charge or energy-to-charge ratios, and are hence able to distinguish the solar wind species from cometary water-group ions. This enables the instruments to detect the loss of the solar wind signal in the cometary coma, and to investigate the ion pickup process (see e.g. Coates et al., 2015). A drawback of the ICA instruments is that the resolution is rather poor. Hence, particles with similar mass-to-charge ratios, such as O^+ and H_2O^+ where $m/q = 16 \text{ amu/C}$ and $m/q = 18 \text{ amu/C}$, respectively, cannot be distinguished from each other (Nilsson et al., 2015b).

Both the ICA and IES instruments are mounted on the spacecraft body itself, and are well inside the spacecraft sheath (see Section 3.1). As mentioned, Odelstad et al. (2016) report on the lower energy boundary in the ICA ion energy spectra being an estimate of the spacecraft potential. This is due to the fact that the collected ions of charge q will have been accelerated by the spacecraft potential and gained an energy of $-qV_{s/c}$ before entering the ICA instrument. Hence, the flux of particles below this threshold will be close to zero.

3.3 Power spectrum

The electric and magnetic field signatures observed by the LAP and MAG instruments can be investigated by the means of spectral analysis. The general idea of doing a spectral analysis of a time signal is to represent the signal in frequency space. This is desirable since a number of physical features are described in terms of frequencies, and by representing the signal as the power per frequency in the power spectral density (PSD), these can be identified and characterized. Stacking together time-adjacent PSDs generated over small time intervals of the entire time signal creates a spectrogram, from which the time evolution of the frequency features can be studied.

To transform a signal into frequency space, an obvious choice is to do a Fourier transformation. For computational purposes, the fast Fourier transform (FFT) that uses the discrete Fourier transform (DFT) is useful, and is hence applied in this work. When computing the PSD of a physical signal, normalization, detrending, and windowing are concepts that must be kept in mind. These concepts are introduced and discussed in Section 3.3.1 followed by an introduction to the Morlet wavelet method in Section 3.3.2. This is an alternative method to the Fourier method for obtaining the spectrogram of a signal. Section 3.3.3 tests the validity of the implementations by reproducing spectra and spectrograms of the electric field signatures in the vicinity of comet 67P on October 25, 2015, studied by Karlsson et al. (2017).

3.3.1 The Fourier method

In the Fourier method, the PSD of a discrete time signal $u(t_n)$ with $t_n = 0, \dots, N-1$ is

$$S_u(n) = \frac{2}{Nf_s} |\tilde{u}(n)|^2, \quad n = 0, \dots, N/2 \quad (3.28)$$

where $\tilde{u}(n)$ is the discrete Fourier transform of the signal, and f_s is the sampling frequency (in Hertz) related to the signal length T (in seconds) and number of samplings N by $f_s = N/T$ (e.g. Eriksson, 2000). Likewise, n relates to the discrete frequencies by $f_n = n/T$. In Eq. (3.28), the maximal detectable frequency of the signal oscillations is the so-called Nyquist frequency $f_{N/2} = f_s/2$ (Leis, 2011). This stems from the symmetry of the Fourier transform (Heinzel et al., 2002), which yields

$$\tilde{u}(N-n) = \tilde{u}^*(n) \quad (3.29)$$

where $\tilde{u}^*(n)$ is the complex conjugate of $\tilde{u}(n)$. The amplitude of the signal oscillation at frequency $|f_n| > 0$ is then $2|\tilde{u}(n)|$. In addition, this explains the 2 in the numerator of Eq. (3.28).

The computation of the PSD in the Fourier method ultimately relies on Fourier transforming the signal, as seen in Eq. (3.28). That the right-hand side of the equation is indeed the density of the spectral power is illustrated by considering the definition of the Fourier transform. This is done below.

Derivation of the Fourier power spectral density (PSD)

The Fourier transform of a complicated time signal represents the signal in frequency space as a sum of fairly simple sine and cosine functions from which information about the frequencies of the oscillations in the wavepackage can be extracted (Kreyszig, 2011). For a continuous time signal recorded during a finite time T , the signal $u(t)$ and its Fourier transform $\tilde{u}(n)$ are related by

$$u(t) = \sum_{n=-\infty}^{\infty} \tilde{u}(n) \exp \left[-\frac{i2\pi nt}{T} \right] \quad (3.30)$$

with

$$\tilde{u}(n) = \frac{1}{T} \int_{t_0}^{t_0+T} u(t) \exp \left[\frac{i2\pi nt}{T} \right] dt, \quad t_0 < t < t_0 + T \quad (3.31)$$

$\tilde{u}(n)$ is then the oscillation amplitude at $f_n = n/T$.

The averaged power P of Eq. (3.30) during the time interval T is then

$$P = \frac{1}{T} \int_{t_0}^{t_0+T} |u(t)|^2 dt = \sum_{n=-\infty}^{\infty} |\tilde{u}(n)|^2 = |\tilde{u}(0)|^2 + 2 \sum_{n=1}^{\infty} |\tilde{u}(n)|^2 \quad (3.32)$$

in which the last two equalities stem from Parseval's equation (Oppenheim and Willsky, 1982) and the assumption of a real signal. The left-hand side of Eq. (3.32) is independent of the length of the time interval T . However, the right-hand side is not. The frequency spacing Δf between two neighbouring frequency values in Eq. (3.31) depends on T (recall that $f_n = n/T$). Hence, the number of $\tilde{u}(n)$ increases with increasing T . To avoid the signal length dependence of $\tilde{u}(n)$, Eriksson (2000) introduces the PSD as

$$S_u(n) = 2T |\tilde{u}(n)|^2, \quad n \geq 0 \quad (3.33)$$

Since $T = 1/\Delta f$, an increase in the signal length T does not influence the PSD for a specific frequency. Note, however, that the definition of the PSD in Eq. (3.33) is only useable for real signals due to the restriction $n \geq 0$.

Applying Eq. (3.33) to (3.32) and assuming a continuous PSD, yields

$$P = \frac{1}{T} \int_{t_0}^{t_0+T} |u(t)|^2 dt = \int_0^\infty S_u(f) df \quad (3.34)$$

implying that $S_u(f)$ is indeed the density of the power P of the real signal $u(t)$.

Above, the time signal $u(t)$ is assumed to be continuous. This is, however, not the case in physical measurements. In general, a signal will be generated with a sampling frequency $f_s = 1/\Delta t$ such that the signal of length N consists of the data points $u(j) = u(t_j) = u(t_0 + j\Delta t)$, $j = 0, 1, \dots, N-1$. The discrete Fourier transform of such a signal is

$$\tilde{u}(n) = \sum_{j=0}^{N-1} u(j) \exp \left[-\frac{i2\pi jn}{N} \right] \quad (3.35)$$

From this and with similar arguments as for the continuous case, the total power of the system is

$$P = \frac{1}{N} \sum_{j=0}^{N-1} |u(j)|^2 = \frac{1}{N^2} \sum_{n=0}^{N-1} |\tilde{u}(n)|^2 = \frac{1}{2} S_u(0) \frac{f_s}{N} + \sum_{n=1}^{N/2-1} S_u(n) \frac{f_s}{N} + \frac{1}{2} S_u(N/2) \frac{f_s}{N} \quad (3.36)$$

where $S_u(n)$ is defined as in Eq. (3.28). Eq. (3.36) is the discrete equivalence to Eq. (3.34) since f_s/N corresponds to the steplength df in a discrete frequency domain. Hence, $S_u(n)$ of Eq. (3.28) is the estimated PSD of the discrete signal.

Time-stationarity and periodicity

Since the Fourier PSD of Eq. (3.28) is computed from the Fourier transform that relies on infinitely periodically sine functions, the method assumes the signal to be stationary in time. A minimum criteria for time-stationarity is obtained when the statistical quantities of the signal, such as mean and variance, are stable with time (Jenkins and Watts, 1968).

If the signal is not sufficiently time-stationary or if the boundary points of the signal differ strongly from each other in the considered domain, the Fourier method might pick up non-physical artificial frequency signatures in the PSD. This is shown in Figure 3.10 where the Fourier PSDs of two simple sinusoidal time series are computed over a time domain that for both signals differ in length from an integer number of the signal periods.

The figure shows that the Fourier method PSDs do identify wave signatures at the frequencies of the sine waves composing the time series, by showing peaks at the frequencies corresponding to the sine wave oscillations. However, the Fourier transforms additionally pick up power for frequencies not present in the original time series. These are termed "sidelobes" and are the lower-intensity peaks seen next to the signal peaks in Figure 3.10(b).

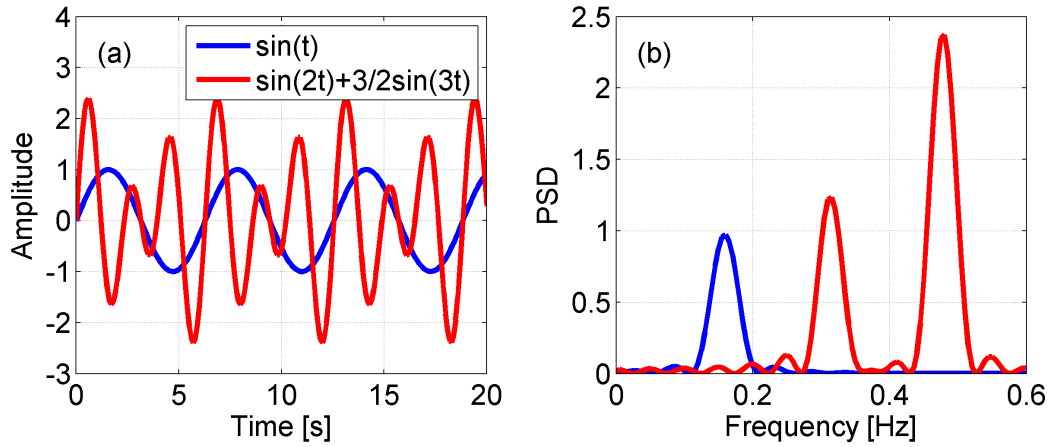


Figure 3.10. (a) Time series, and (b) Fourier PSDs of sine curve with frequency $(2\pi)^{-1}$ Hz and sum of sine curves with frequencies π^{-1} and $3/(2\pi)$ Hz. The PSDs peak at the wave frequencies $(2\pi)^{-1}$, π^{-1} , and $3(2\pi)^{-1}$ Hz, respectively.

The sidelobes appear due to the difference in the initial and final wavepower in the time series. It is seen from the time domain expression of Eq. (3.30) that the Fourier transform assumes a periodic input function in which the signal of length N repeats itself infinitely for every N steps, such that $u(t_i) = u(t_i + T)$. If the considered time interval does not equal a multiple of the wave period, as is the case for $u_1(t)$ and $u_2(t)$ in Figure 3.10(a), the FFT experiences a discontinuity in the periodic spectrum for each N data points. This, ultimately, results in additional artificial power displayed across the spectrum (Heinzel et al., 2002). To some extent this can be overcome by detrending and windowing the signal before transforming it into frequency space.

Detrending

A trend in a signal is a feature that starts before the sampling, affects the data points in a more or less similar way throughout the observation, and continues after. Hence, it is longer than the sampling period. Experimentally gained data might show various types of trends that are more or less artificial and might influence the data processing causing features with no relevant physical meaning. Furthermore, a non-relevant trend might carry energy to all or a significant part of the data points, which might reduce the visibility of interesting features in the PSD. In these cases it is therefore an advantage to remove the trend, i.e. detrending the signal, before processing the data.

There are several ways of detrending data, and the optimal detrending method or whether detrending is even necessary ultimately depends on the purpose of the data processing and the data itself. However, it is important to understand the physical origin of the trend itself before the detrending, since what one might think is an uninteresting trend could actually be a crucial part of the relevant data itself.

To reduce the risk of trend-caused artificial power throughout the spectra, it is often advantageous to subtract a linear fit from the signal, and a simple way of removing low-frequency fluctuations in a time series is by subtracting a moving average from the signal. The moving average filter replaces a data point by the average value of that point and its neighbours, and is therefore often used to smooth a dataset. The number of neighbours can vary, but will always to an equal number such that the span of the moving average filter is uneven. In general, if the number of neighbours to each side is N , the average at the data

point $u(n)$ is

$$u_s(n) = \frac{1}{2N+1} (u(n+N) + u(n+N-1) + \cdots + u(n-N+1) + u(n-N)) \quad (3.37)$$

where all neighbours and the data point itself are weighted equally. By subtracting the moving average from the signal, such that the detrended data is $u_d(n) = u(n) - u_s(n)$, large-scale time features are filtered out. Due to the inverse relation between time and frequency, moving average-detrending results in a depression of the low-frequency domain.

Windowing

To filter out artificial high-frequency features and dampen sidelobes caused by e.g. different signal amplitudes at the start and end point of the time series, the signal can be windowed. A window is often a symmetric function with values between 0 and 1. For practical purposes, the window $w(n)$ is a vector of equal length as the signal $u(n)$, such that the windowed signal is

$$u_w(n) = u(n) \cdot w(n), \quad \text{for } n = 1, \dots, N \quad (3.38)$$

Since $w(n) \leq 1$ for all n , windowing the signal causes a general loss in power in the computed PSD. According to the definition of the PSD in Eq. (3.28), the loss caused by windowing the signal (i.e. $u(n) \rightarrow u_w(n)$) scales with the weighting squared, i.e. $w(n)^2$. Hence, an obvious estimate for the total power loss is

$$W_{loss} = \frac{1}{N} \sum_{n=1}^N w(n)^2 \quad (3.39)$$

as introduced by Eriksson (2000). To compensate for the loss in power, the computed PSD can be divided by this number, such that the loss-corrected PSD computed from a windowed time signal is $PSD_c = PSD_w / W_{loss}$.

The simplest window is the rectangular window. This is a step function that takes on the value 1 for all n , and equals zero everywhere else. Hence, the rectangular window leaves the data unaltered. However, the main advantage of applying a window to the signal is to reduce the edge effects illustrated as sidelobes in Figure 3.10. It is, therefore, often relevant to introduce windows that alter the data at the edges and leave data central in the signal as undisturbed as possible, i.e. a window where the weighting goes to or close to zero at the boundary and has a large value at the central part. One of these, is the triangular window $w_T(n)$. The triangular window takes on the values $w_T(1) = w_T(N) = 0$ and $w_T((N+1)/2) = 1$ for an interval $1, \dots, N$ with an uneven number N of data points. Data points between the start, middle and end points are weighted by a factor determined by a linear relation between the start and central points or the central and end points. This gives a triangular shape of the window, hence the name.

Two widely used windows that resemble the normal distribution are the Hanning and Hamming windows (Oppenheim et al., 1999). The Hanning window is given as

$$w_{Hann}(n) = \frac{1}{2} \left(1 - \cos \left(2\pi \frac{(n-1)}{(N-1)} \right) \right), \quad \text{for } n = 1, \dots, N \quad (3.40)$$

whereas the Hamming window takes the form

$$w_{Hamming}(n) = 0.54 - 0.46 \cos \left(2\pi \frac{n}{N} \right), \quad \text{for } n = 1, \dots, N \quad (3.41)$$

Eq. (3.40) and (3.41) show that both take the value 1 at the central points, but differ at the edges where the Hanning window goes to zero whilst the Hamming window does not. The time domain behaviour of these windows are plotted in Figure 3.11(a) along with the rectangular and triangular windows. The blue circles on the Hanning window at the times 0, 5, 10, 15, and 20, are the values of the window for $N = 5$, i.e. $w(1) = w(5) = 0$, $w(2) = w(4) = 0.5$, $w(3) = 1$, and show the symmetry of the function for an uneven N .

Applying a window to a time signal eventually affects the computed PSD in frequency domain. Figure 3.11 shows the same two sinusoidal functions as in Figure 3.10 in both time and frequency space. In Figure 3.11(b) these are, however, windowed by the Hanning window, and the resulting PSDs are given in Figure 3.11(c) along with the loss-corrected PSD of the Hanning-windowed signal. To compare the effects of the Hanning and Hamming windows, the black lines in Figure 3.11(c) give the corresponding PSDs of the Hamming-windowed signal. The sidelobes observed in the PSD of the unwindowed signal of Figure 3.10(b) are reduced enough to not be detectable by in either of the PSDs of the Hanning- or Hamming-windowed signal in Figure 3.11(c). Heinzel et al. (2002) mention that for a window that is discontinuous at the edge, such as the rectangular and Hamming windows the sidelobes fall off as f_n^{-1} , whilst they fall-off as f_n^{-3} when applying a window that is continuous in both the function and its derivative, such as the Hanning window. This explains the reduction of sidelobes for the windowed function in Figure 3.11(c) compared to the non-windowed function in Figure 3.10(b).

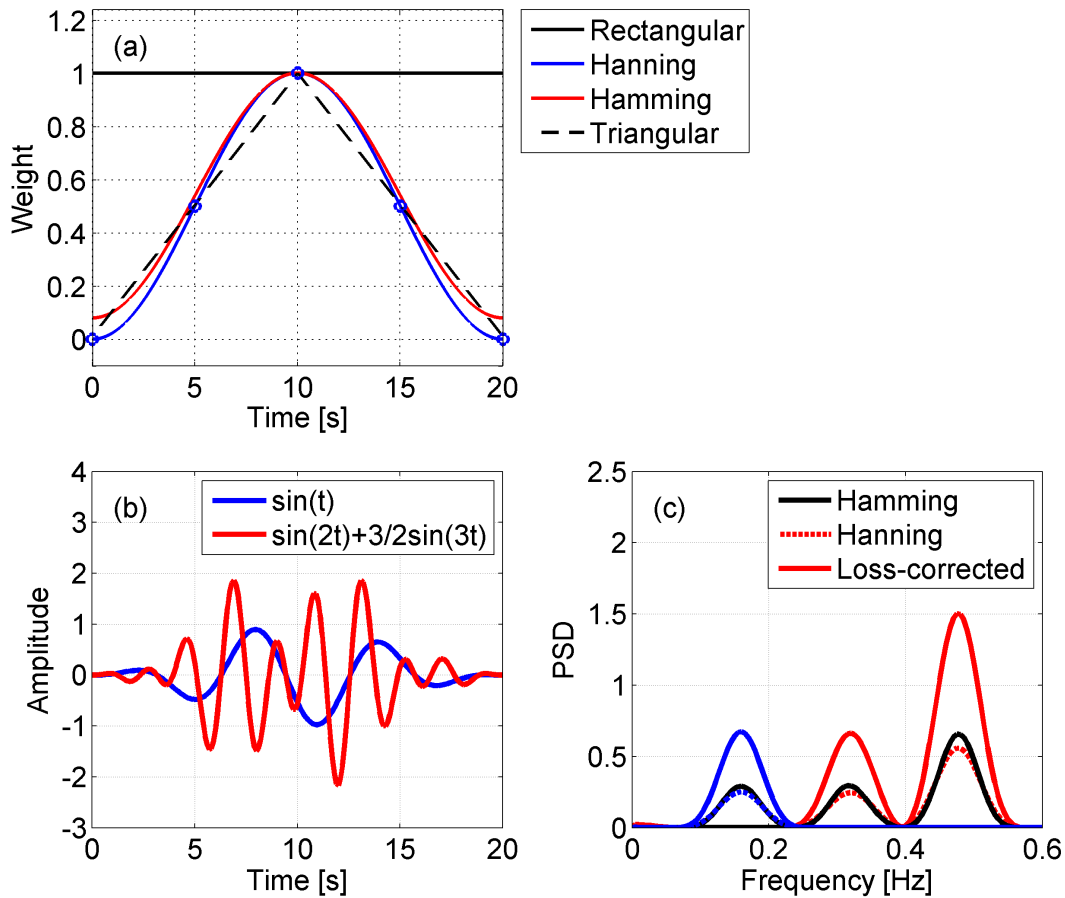


Figure 3.11. (a) Selection of windows, (b) Hanning-windowed signal of time series in Figure 3.10(a), and (c) corresponding PSDs. The dashed blue and red curves in (b) and (c) are the PSDs of the Hanning-windowed signals, whilst the solid lines are the similar loss-corrected PSDs (see Eq. (3.39)). The black lines are PSDs of the same Hamming-windowed signal.

A drawback of windowing is the general reduction of the power and a broadening of the peaks. The power loss is, however, almost compensated for by loss-correcting the PSDs with Eq. (3.39). To conclude, the windowing of a signal causes a loss of information and results in a greater frequency uncertainty as compensation for a depression of artificial signatures in the spectrum. Therefore, whether or not the windowing of a signal is an advantage has to be evaluated for the specific signal.

Noise reduction and overlapping

Eriksson (2000) mentions that the standard error for a PSD is $\sigma_m = 100\%$. By averaging unwindowed sub-PSDs, the standard error decreases by a factor of $1/\sqrt{M}$ (Olofsson and Andersson, 2012). Assume dividing a signal of N data points into M sub-domains, each containing L data points. If all M time-adjacent sub-PSDs are similar in shape and features, they can be used in the computation of an average PSD for the entire investigated period. The averaged PSD is then

$$\langle S_u(n) \rangle = \frac{1}{M} \sum_{m=1}^M S_{u_m}(n) \quad (3.42)$$

where S_{u_m} denotes the PSD of the m 'th sub-interval. Even though averaging increases the signal to noise ratio, it might not always be an advantage. This is due to the fact that averaging requires a division of the interval, causing each sub-interval to be shorter than the total signal. Since the lowest detectable frequency is inversely proportional to the interval length, a splitting of the signal might reduce detectability of signatures in the low-frequency range of the spectrum.

As mentioned, if a non-rectangular window is, additionally, applied to a sub-intervals, signal information is reduced due to the windowing coefficients being in the interval $0 \leq w(n) \leq 1$. This might not be a problem if the signal is completely time-stationary and the sub-intervals are long enough to detect all waves. If not, a splitting of the data set into several overlapping sub-intervals, such that some or all data points influence more than one spectrum, might be a way of overcoming the information loss. The principle is that data points of low weights in one sub-interval will be important in another resulting in all data points being of roughly the same importance when summing up their weightings in different sub-intervals.

An overlapping of 10-s sub-intervals windowed by the triangular window is shown in Figure 3.12. Due to the 50% overlap in the figure, the sum of weightings for each point in the triangular-windowed data is 1, yielding that all points are on average equally important. Note however, that the first and last sub-intervals will contain points that are only contributing to those intervals, and consequently some information is still lost due to the windowing method.

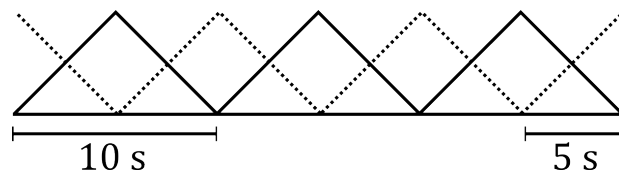


Figure 3.12. Illustration of overlapping sub-intervals with an applied moving triangular window.

There are two main considerations to take into account when determining the "optimal" overlapping of windowed time intervals. One is the so called "amplitude flatness", whilst the other is the "overlap correlation" (Heinzel et al., 2002). When overlapping sub-intervals, a point will be weighted multiple times. Adding up all weightings for a point gives the total weighting of this point. The amplitude flatness is the ratio of the minimum and maximum of the total weighting of any point. If all points are assumed equally important, it is desirable to have this value as close to one as possible. The overlap correlation gives a measure of the correlation for an overlap. To reduce the computational time, the correlation should be as small as possible, reducing overlap as much as possible. With the amplitude flatness and the overlap correlation being equally important, the recommended overlap is when the difference between these two functions is as large as possible. Heinzel et al. (2002) states that for the Hanning window, this is achieved for a sub-interval overlap of 50%.

Filtering out data gaps

When continuously computing and averaging the PSDs of sub-intervals of a signal, the appearance of data gaps can alter the results and depress real physical signatures by introducing artificially high power in the spectra. This is indeed the case for the electric field mode of the LAP instrument, where the low-sampling frequency mode periodically introduce a 1 s data gap roughly every 32 s.

That the data gaps can cause an artificially high-power Fourier spectra can be illustrated by introducing a data gap in an otherwise clean sinusoidal signal. This is done in Figure 3.13 where Fourier PSDs are computed from a sinus function of period $(2\pi)^{-1}$ Hz over three different time intervals. The first and last time intervals consist of continuous data, whilst the second interval has a 9 s data gap. The PSDs of the former clearly show a peak at $(2\pi)^{-1}$ Hz, whilst the latter results in a noisier spectra of generally higher power for frequencies not existing in the original time signal.

The artificially high power caused by the presence of data gaps can be overcome by using only the continuous sampling in-between the gaps. The principle of this is shown in Figure 3.14 for a triangular-windowed signal that resembles the LAP electric field mode. However, when windowing each of the sub-intervals in-between two gaps, more information is lost than for continuous sampling, since one half of the first and last sub-intervals have no overlap with other sub-intervals.

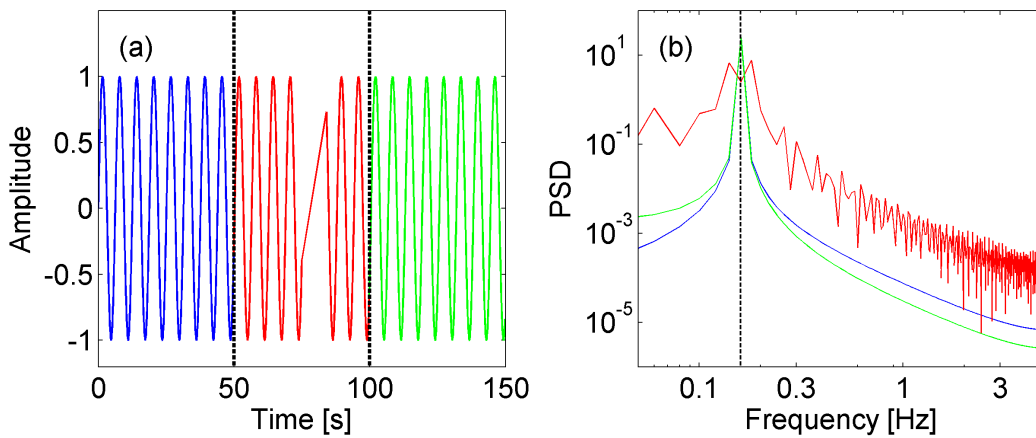


Figure 3.13. (a) Sinusoidal time series of frequency $(2\pi)^{-1}$ Hz with a 9 s data gap, and (b) corresponding PSDs. The color-coding of the PSDs match the colors of the time intervals they are computed over.

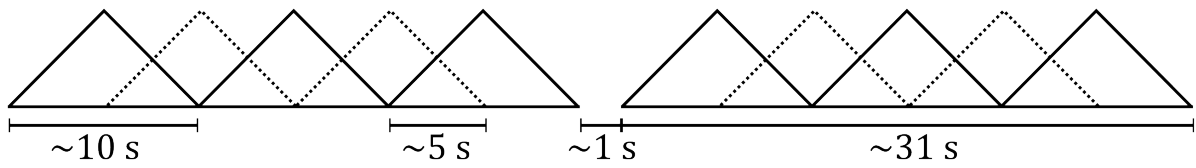


Figure 3.14. Illustration of division of continuous sampling between data gaps into sub-intervals.

With this in mind the spectrum resulting from the Fourier method depends on the choice of signal length, averaging, overlapping, detrending and windowing, and ultimately counts on the assumption that the signal is time-stationary and free of data gaps. Taking this into account through visualization of the data and comparison of the effect of different analysis methods on the spectra, the Fourier method is, however, a reliable method in the computation of a signal PSD.

In the Rosetta mission, electric and magnetic field measurements done aboard the spacecraft rarely show time-stationarity for a long time period. Changes in spacecraft orientation and manoeuvring, solar wind fluctuation, comet outgassing variations and instabilities on the large-scale cometary boundaries are all factors that might eventually affect the the signatures of the observed quantities.

One, therefore, has to be careful when choosing sub-interval lengths, periods for averaging and signal altering methods. A comparison of sub-PSDs in the spectrogram that depicts the time evolution of the frequency space can give a clue about whether the signatures are similar enough to compute an average. Another way of checking the reliability of the signatures in the Fourier spectrogram is to compare it to the Morlet wavelet spectrogram, introduced in the next section. The Morlet wavelet spectrogram does not assume time-stationarity and has a better time resolution than the Fourier method. Hence, signatures observed simultaneously in both the Fourier and Morlet wavelet spectrograms are good candidates of being real physical phenomena and not method-induced.

3.3.2 Morlet wavelet analysis

Wavelet analysis provides an alternative to the sliding Fourier transform to evaluate the spectrogram of a signal in time-frequency space. Whereas the time series and its Fourier transform are localized in time and frequency, respectively, and spread out in the other component, the wavelet is localized in both time and frequency to the extent allowed by the uncertainty principle ($\Delta f \Delta t \geq 1$) (Eriksson, 2000). Farge (1992) thoroughly reviews the wavelet method, whilst Torrence and Compo (1998) provide a well-documented MATLAB script for computing the wavelet transform of a time signal. The latter is used in the data analysis of Chapter 4 to support the PSD findings obtained from the Fourier transform. This section is dedicated to give only a brief introduction to the principles behind wavelet analysis, and the nature of the Morlet wavelet.

The wavelet analysis of a time signal is based on a so-called mother wavelet that is finite in time and has a finite energy, as opposed to the infinite sinusoidal signals of the Fourier transform. From the mother wavelet, a family of daughter wavelets are computed. The correlations between the daughter wavelets and the signal are estimated to determine the power of the oscillations. There are several possible wavelets to choose as the mother wavelet. However, similar for all is that they must fulfil the wavelet criteria, including that the wavelet must have a finite energy, a zero mean and be localized in time and frequency (Farge, 1992).

The choice of wavelet influences the results. Hence, it is important to choose a wavelet that fits the time series to a sufficient extent. An often used wavelet is the Gaussian-modulated plane wave Morlet wavelet introduced by Morlet et al. (1982). It is given as

$$\psi_0(t) = e^{i\omega_0 t} e^{-t^2/2} \quad (3.43)$$

with Fourier transform

$$\tilde{\psi}(\omega) = \sqrt{2\pi} e^{-(\omega - \omega_0)^2/2}, \quad \text{for } \omega > 0 \quad (3.44)$$

In Torrence and Compo (1998), the wave frequency ω_0 is set to 6 to fulfil the wavelet criteria. They, in addition, introduce a normalisation factor of $\pi^{-1/4}$ in Eq. (3.43). Figure 3.15(a)-(b) shows the composition of the Morlet wavelet of Eq. (3.43) in time domain along with its Fourier transform for $\omega_0 = 6$.

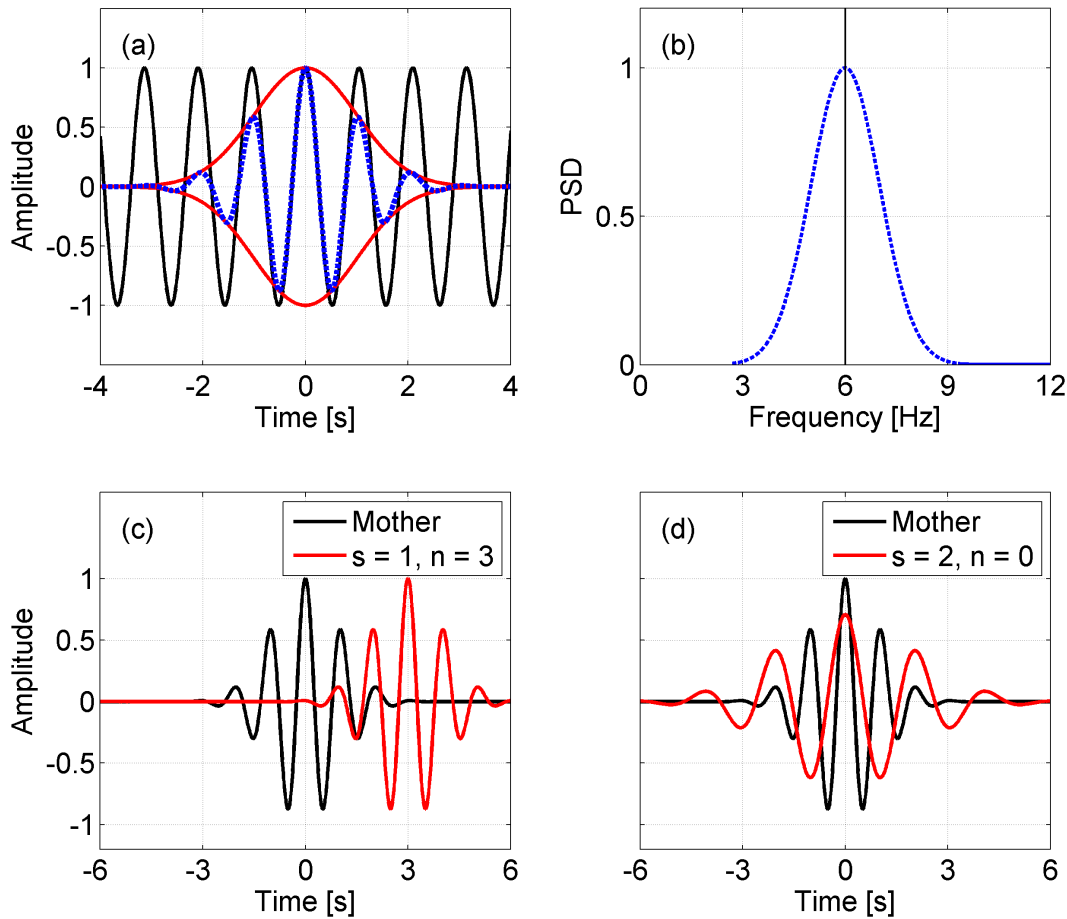


Figure 3.15. (a) Real part of the Morlet wavelet generated from a plane wave (black) and Gaussian envelope (red) with $\omega_0 = 6$. (b) Fourier transformed Morlet wavelet in frequency space. (c)-(d) Morlet mother wavelet (black) and daughter wavelets (red) with different scaling s and translation n parameters. The scaling parameter changes the frequency of the wave, whilst the translation parameter changes the time location of the wavelet.

The daughter wavelets ψ_{sn} are generated from the mother wavelet ψ_0 by introducing a scaling parameter s and translation parameter n , such that

$$\psi_{sn}(t) = \frac{1}{\sqrt{s}} \psi_0 \left(\frac{t-n}{s} \right) \quad (3.45)$$

n indicates the position of the daughter wavelet along the time axis, whilst changes in s result in different frequencies of the wavelet oscillations. However, s does not change the number of oscillations in the wavelets, and hence, smaller temporal scales correspond to higher frequencies (Farge, 1992). From Eq. (3.45) it is evident that $\psi_{1,0} = \psi_0$, and hence the first wavelet that is compared to the signal is the Mother wavelet. Figure 3.15(c)-(d) illustrate the effect of changing the scaling and translation parameters of the Morlet wavelet.

For every time step, the signal is compared to a daughter wavelet with a specific scaling parameter s_i . All time steps are then scanned by varying n . When all data points have been compared to the s_i 'th daughter wavelet, s is varied and the signal is compared to the new wavelet, once again by varying n . This is done for all daughter wavelets over the entire domain. In the MATLAB algorithm of Torrence and Compo (1998), the comparison is, however, done in frequency space to speed up the computation. The comparison between the signal and the daughter wavelets in frequency space is done by computing the wavelet transform. For a discrete time signal $u(t)$ of length N , the wavelet transform takes the form (Chun-Lin, 2010):

$$W_n(s) = \frac{1}{\sqrt{a}} \sum_{i=0}^{N-1} u(i) \psi_0^* \left(\frac{i-n}{s} \right) \quad (3.46)$$

where ψ_0^* is the complex conjugate of the mother wavelet ψ_0 . The Torrence and Compo (1998) method uses fast Fourier transform to transform the signal and wavelets into frequency space and hence assumes periodicity of the signal, as well. This is partly overcome by padding the ends of the signal with zeroes, but might influence the low-frequency part of the spectrum, since this corresponds to large scales, i.e. long time intervals.

From the frequency-power information gained by comparing different daughter wavelets to the signal, the wavelet power spectrum is computed as the square of the wavelet transform. To make the power comparable to the PSD obtained from the Fourier method in Eq. (3.28), the wavelet power spectrum is additionally divided by the sampling frequency f_s , such that

$$S_n(s) = \frac{1}{f_s} |W_n(s)|^2 \quad (3.47)$$

Whereas the Fourier PSD of Eq. (3.28) transforms an entire interval into frequency space by representing the signal by a sum of sine oscillations, the Morlet wavelet scans all points in the time series and, at each of them, compares the signal to various wave packages. Since low-frequency signals are detected by comparing daughter wavelets of large scales (long wavelengths) to the signal, the time resolution is poor for low-frequency signatures. For high frequencies, the scales are small, and hence the time resolution is good. From the uncertainty principle ($\Delta f \Delta t \geq 1$) this results in a good low-frequency resolution and a poor high-frequency resolution. Hence, the time resolution of a Fourier spectrogram is limited by the time interval length, whilst frequency and time resolution of the Morlet wavelet method varies with frequency.

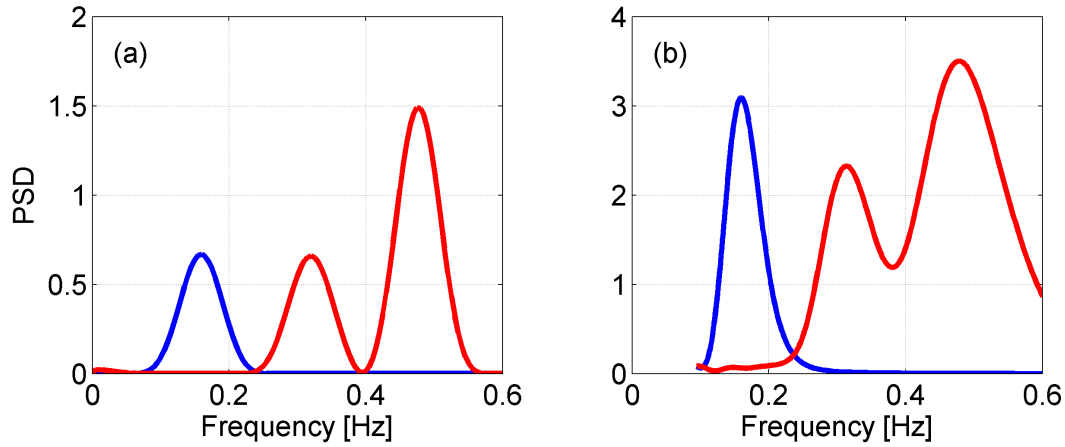


Figure 3.16. (a) Loss-corrected Fourier PSDs of Hanning-windowed signal and (b) Morlet wavelet PSDs of the same sinusoidal waves as in Figure 3.10.

Figure 3.16 shows the wavelet spectrum of the same sinusoidal signal as investigated by the Fourier method in Figure 3.10. The PSD is generated by averaging over all $S_n(s)$ for each s . This, together with the uncertainty principle, result in Morlet wavelet PSDs in Figure 3.16(b) that are less localized in frequency than the Fourier PSD in Figure 3.16(a).

The Morlet wavelet method of Figure 3.16(b) succeeds in detecting the frequencies of the original sinus waves with a power of the same order of magnitude as detected by the loss-corrected Hanning-windowed Fourier method in Figure 3.16(a). This indicates that the Fourier and Morlet wavelet methods can indeed be used complementary to detect wave signatures in times series.

3.3.3 Reproduction of electric field signatures observed in the vicinity of comet 67P

This section provides a reproduction of a recently published Fourier spectral analysis of electric field fluctuations in the plasma environment close to comet 67P studied by Karlsson et al. (2017). The Morlet wavelet method is, additionally, included to show the similarities between spectrograms computed from the Fourier and Morlet wavelet methods. In the Karlsson et al. (2017) study, these wave signatures are interpreted as lower hybrid frequency (LHF) oscillations in the electric field measured by the LAP instrument. The study includes two events with the LAP instrument in floating potential electric field mode without an applied bias.

The electric field spectral analysis of the October 25, 2015, event is reproduced in this section as a validation of the implemented Fourier and Morlet wavelet methods. During this day, the Rosetta spacecraft was at a cometocentric distance of 348 km and at a heliocentric distance of 1.52 AU. Figure 3.17 gives the calibrated probe potentials V_1 and V_2 , estimated electric field and Fourier and Morlet wavelet spectrograms for a similar time interval as the one in the Karlsson et al. (2017) study. During the interval, both probes were sunlit, and the calibration of these is presented in Figure 3.7.

The PSDs of the Fourier spectrogram presented in Figure 3.17(b) are computed from 10 s Hanning-windowed sub-intervals with a 50% overlap of a moving average-detrended electric field estimate to make it comparable to the spectrogram presented in Karlsson et al. (2017). The Morlet wavelet spectrogram of Figure 3.17(c) is included as a validation of the signatures seen in the Fourier spectrogram.

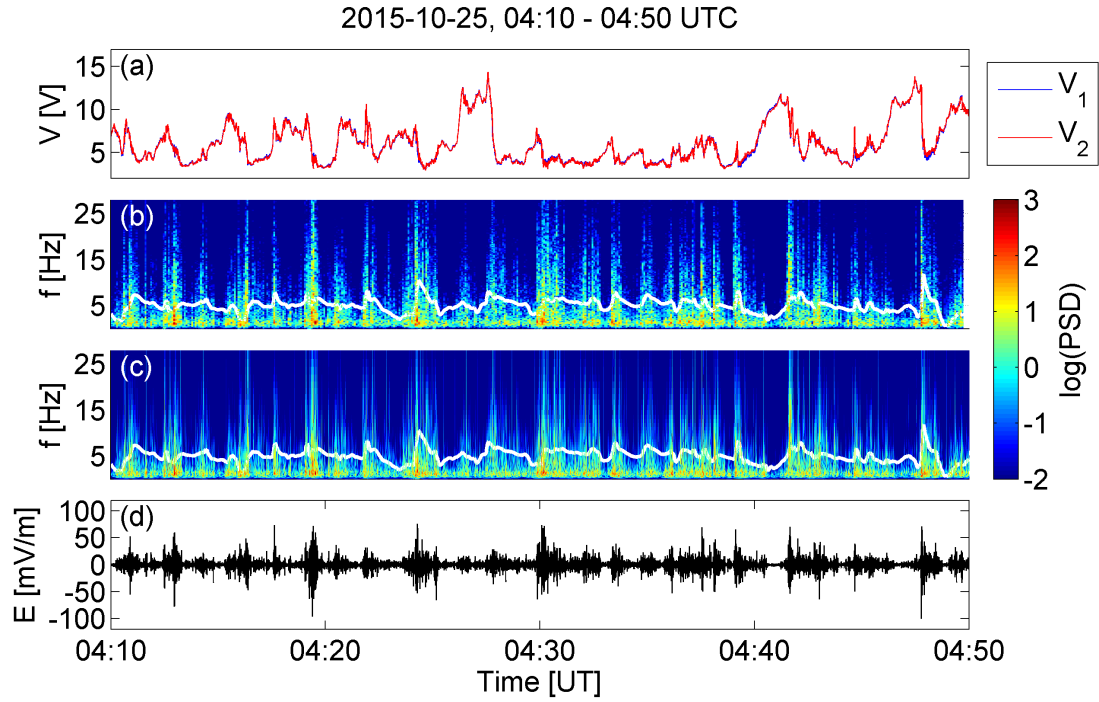


Figure 3.17. Electric field data during a similar time interval on October 25, 2015, as that studied by Karlsson et al. (2017). (a) Calibrated probe potentials. (b) Fourier spectrogram computed from Hanning-windowed electric field sub-intervals of 10 s with an overlap of 50%. (c) Morlet wavelet electric field spectrograms. In (b) and (c) the white lines are the local LHF estimated from the MAG magnetic field. (d) Detrended electric field fluctuations. A moving average of span 1 s is subtracted from the 57.8 Hz electric field data to remove low-frequency oscillations.

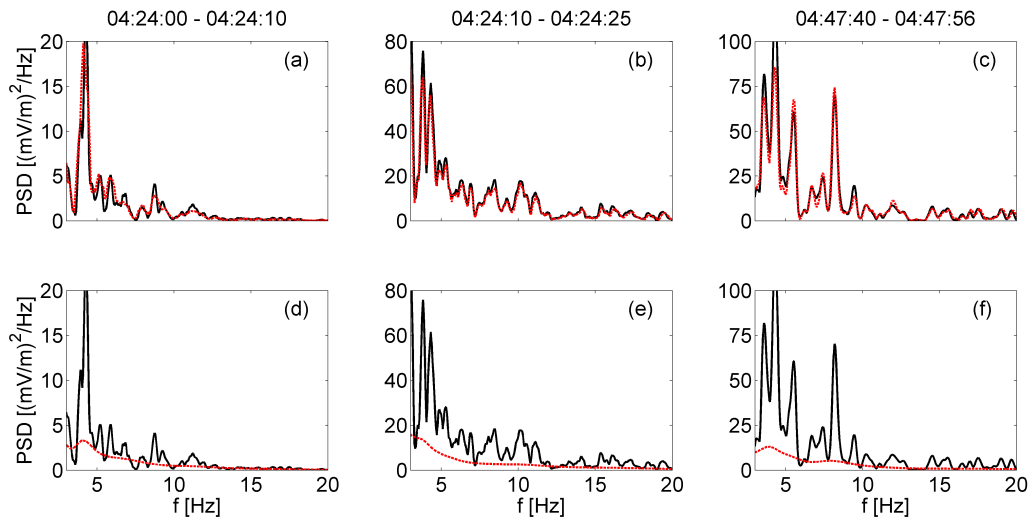


Figure 3.18. PSDs during three different time intervals within the time scale of Figure 3.17. (a) - (c) Fourier method. (d) - (f) Averaged Morlet wavelet PSDs. The dashed red lines are the PSDs computed by the implementation of the Fourier and Morlet wavelet methods in this work, whilst the solid black lines are results from Karlsson et al. (2017) provided by Tomas Karlsson (KTH, Stockholm, Sweden).

The white lines in the spectrograms indicate the LHF of Eq. (2.36) simplified to

$$f_{LH} \approx \frac{1}{2\pi} \sqrt{\Omega_{ce}\Omega_{ci}} \quad (3.48)$$

computed from the water-ion (H_2O^+) and electron gyrofrequencies Ω_{ci} and Ω_{ce} . The approximation of the LHF is reasonable whenever $\omega_{pi} \gg \Omega_{ci}\Omega_{ce}$, which is the case for the considered situation where $B \approx 30 \text{ nT}$, $n_i \approx 500 \text{ cm}^{-3}$ and $m_i \approx 18 \text{ amu}$. The magnetic field magnitude used in the computation of the gyro frequencies is obtained from PSA as the 1 s averages for the out-board MAG sensor.

Figure 3.18 zooms in on four individual PSDs computed from the time series of Figure 3.17. These are intervals studied by Karlsson et al. (2017) to illustrate the appearance of electric field oscillations in the LHF range. The figure shows the electric field PSDs computed by the implementation of the Fourier method in this work and the Morlet wavelet method by the Torrence and Compo (1998) wavelet implementation, together with Fourier PSDs provided by Tomas Karlsson (KTH, Stockholm, Sweden). Note, however, that the displayed power of the results from Karlsson et al. (2017) vary slightly from the ones given in the paper due to a slight difference in the generation of these.

The implementation of the Fourier method in this study gives similar spectra as those presented in Karlsson et al. (2017), and the peaks identified as oscillations within the LHF range are determined with similar powers in both Fourier implementations. The Morlet wavelet method picks up the peaks in Figure 3.18(d) and (f), but with a lower power and a cruder frequency resolution. The lower power of the Morlet method might be caused by e.g. a difference in normalization of the PSD in Eq. (3.28) compared to (3.47) and the fact that the Fourier method is loss-corrected by Eq. (3.39) after computing the PSD from a Hanning-windowed time interval. The less prominent signatures of the Morlet PSDs compared to the Fourier PSDs might be caused by the averaging of several Morlet spectra in the intervals or by a lower frequency resolution of the chosen wavelet transform relative to the Fourier method frequency resolution. However, recall that the error of a non-averaged Fourier PSD is high (see Section 3.3.1), and hence the fluctuations in the Fourier spectra could be artificially generated by the method.

The plots of Figure 3.18 clearly show that the Fourier method implemented in this work is able to reproduce signature in published works, and that the Morlet wavelet method of Torrence and Compo (1998) used in this study to supplement the findings of the Fourier method identifies the same features at lower power and with a more smeared out signature in frequency space.

3.4 Summary of the electric and magnetic field data analysis methods

The LAP electric field mode provides probe potentials V_1 and V_2 measured relative to the spacecraft, whilst the data provided by the MAG team is the temperature-corrected three-dimensional magnetic field components (B_x, B_y, B_z). In this work, the magnetic field components are additionally cavity-calibrated by subtracting the mean of each component inside the cavity from the entire signal of that component. The probe potentials are calibrated by a translation of V_2 into a system where the linear regression between V_1 and V_2 has a slope of 1 and goes through $(V_1, V_2) = (0, 0)$. The electric field is estimated from the calibrated probe potentials as the potential difference divided by the probe separation distance. Since the electric field is estimated in only one direction, the magnetic field components can advantageously be translated into a system where one magnetic field component is parallel to the electric field estimate whilst the others are perpendicular.

In the data analysis of this work, the spectral analysis of the electric and magnetic field fluctuations relies on the Fourier and Morlet wavelet methods that have proved to be able to reproduce results published in the study by Karlsson et al. (2017). The Fourier method is localized in frequency, but spread out in time, and requires time-stationarity, whilst the Morlet wavelet method is stationary in both time and frequency (to the extent of the uncertainty principle). The Fourier method, however, allows for several data altering aspects, such as the detrending, windowing, overlapping and averaging, and a combination of these might result in a more reliable analysis. In this work, the Fourier and Morlet wavelet methods are used supplementary to discuss whether the signatures seen in the spectra have physical origins or are caused by the implementation of the methods.

In addition to spectral information, the MVA of the three magnetic field components can give an estimate of the normal to a crossed boundary. Hence, it provides information about the spatial structures of the observed events, and it is found that the implementation of the MVA, in this work, succeeds in reproducing results presented in the published study by Goetz et al. (2016a).

RESULTS AND DISCUSSION

During the last two years of the Rosetta mission, when the Rosetta spacecraft was accompanying comet 67P, features of the structure and evolution of the cometary plasma environment on the dayside of the comet have been unravelled by the plasma and field instruments of the Rosetta Plasma Consortium (RPC).

Through more than half a decade prior to the Rosetta mission, several large-scale boundaries and regions on the dayside of an active comet have been argued for, in the light of pre-Rosetta comet flybys, simulations and theoretical work (see Section 2.4). However, only some of these structures have been observed and studied in the vicinity of comet 67P (see e.g. the IES studies by Mandt et al. (2016) and Nemeth et al. (2016), and the MAG study by Goetz et al. (2016b)).

Most of the RPC boundary studies focus on the diamagnetic cavity due to the numerous crossings in and out of this region. This chapter presents the first event study on the electric field signatures estimated from the RPC Langmuir probe (LAP) instrument aboard the Rosetta spacecraft during some of the cavity crossings. The studied cavities are put into the context of the current understanding of cometary diamagnetic cavities by including several RPC instruments in the characterization of the nature of these events.

4.1 Event characteristics

As seen in Section 2.4.3, the cometary diamagnetic cavity is defined as a region within which all components of the magnetic field are nearly zero. It is bounded by the contact surface that marks the end of the diamagnetic cavity boundary layer (DCBL). Inside the DCBL, the magnetic field gradually goes to zero. Within the magnetic field-free cavity charged cometary particles are generated. These particles travel radially from the comet, and when entering the DCBL, they start gyrating. Due to the gyration of the charged particles a current is induced perpendicular to the stagnant magnetic field.

The clear magnetic field signatures of diamagnetic cavities make the magnetic field measurements of the RPC Magnetometer (MAG) instrument good indicators of cavity crossings. Even though several hundred cavity events have been observed and studied in the magnetic field of the MAG instrument (Goetz et al., 2016b), only events on two dates coincide with the LAP instrument in electric field mode. These are a 4 min cavity on May 28, 2015, and two 0.25-1 min cavities on February 17, 2016. In the subsequent analysis these are notated M15, F16a and F16b, respectively.

The three cavity crossings are a part of the statistical study of magnetic signatures in and around cavities in the vicinity of comet 67P, performed by Goetz et al. (2016b), but whereas the M15 event occurs during a period of frequent and relatively long cavity crossings, the F16 events are the last two cavities included in the study and appear on much shorter time scales. The difference in duration of the cavities is easily seen in Figure 4.1, where their magnetic field components in the comet-centered solar equatorial (CSEQ) coordinate system (see Figure 3.3 in Section 3.2.1) are shown for time spans over the cavity crossings. Note that panel (a) spans over 25 min, whilst panel (b) has an 18 min time span. The vertical lines in Figure 4.1 mark the temporal contact surface positions defined by the MAG instrument using the convention in Goetz et al. (2016b) and given in Table 4.1.

The magnetic field data is cavity-calibrated by subtracting the mean of each of the magnetic field components inside the cavity from the entire signal of that component. Hence, the means of B_x , B_y , and B_z are zero within the cavity, whilst the mean of the magnetic field magnitude $\langle B \rangle$ might be a finite number, which is the case for the studied events. Inside the M15 cavity $\langle B \rangle = 1.68$ nT, whilst $\langle B \rangle = 1.11$ nT inside the F16a cavity, and $\langle B \rangle = 0.43$ nT inside the F16b cavity that is used for the cavity-calibration of the magnetic field during the F16 events.

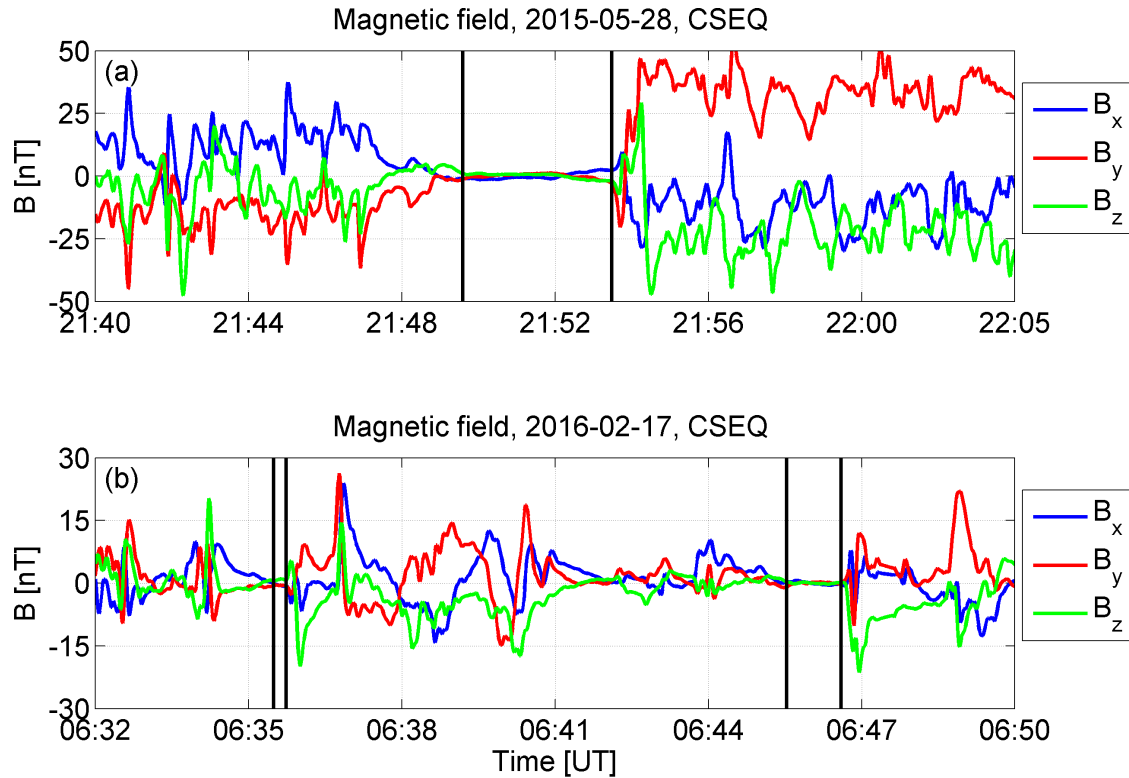


Figure 4.1. 1 s average of the magnetic field components in the CSEQ coordinate system during the (a) M15, and (b) F16 cavity crossings. The components are cavity-calibrated such that the means of each magnetic field component are zero within the cavities. The vertical black lines indicate the contact surfaces defined by the MAG instrument.

The three cavity events of Figure 4.1 are preceded by a gradual decrease in the magnetic field components and succeeded by a sharp increase in these. This implies a long inbound DCBL and a short outbound one, as are typical features of cavity crossings around comet 67P (Goetz et al., 2016b). Note, however, that the nature of the DCBL described here might vary from the theoretically defined one in Section 2.4.2. This is due to the short durations of the studied cavities, which suggests that the observed events are not crossings over the perfectly elliptical large-scale contact surface limiting the cavity. Goetz et al. (2016a) instead suggest that the observations are most likely caused by e.g. Kelvin-Helmholtz instabilities on the contact surface moving over the spacecraft (see Figure 5 in the referred article). The M15 cavity, in addition, shows signs of magnetic field draping in the B_x and B_y components. However, no clear draping signature is seen in the magnetic field around the F16 cavities. This might be related to the short duration of the cavity observation and is further discussed in Section 4.1.2.

4.1.1 Event parameters

In the comet frame, the cometary neutrals move radially away from the nucleus with a speed of the order of 1 km/s. During the studied events, the speed of the spacecraft relative to the comet is less than 1 m/s, and is thus negligible compared to particle motion. Hence, in the comet frame of reference the spacecraft can be considered stationary compared to the cavity plasma and neutral flow. The speed of the spacecraft is estimated over the cavity crossings from the change in spacecraft position and is presented in Table 4.1. The table, additionally, give the temporal contact surface positions determined from the MAG instrument, cometocentric distances, solar distances of the comet, estimated outgassing rates and stand-off distances of the contact surfaces for the studied events.

The outgassing rate estimates are computed from the empirical model by Hansen et al. (2016). The model builds on measurements from multiple instruments aboard the Rosetta spacecraft during the two years of monitoring the evolution of comet 67P, and gives that the outgassing rate Q is related to the heliocentric distance d_h in AU by

$$Q = (2.59 \pm 2.75) \times 10^{28} \times d_h^{-5.18 \pm 0.06}, \quad \text{before perihelion} \quad (4.1)$$

$$Q = (1.58 \pm 0.09) \times 10^{29} \times d_h^{-7.15 \pm 0.08}, \quad \text{after perihelion} \quad (4.2)$$

Since the comet reached perihelion on August 13, 2015, the outgassing rate of May 28, 2015, is computed from Eq. (4.1), whilst the outgassing rate of February 17, 2016, is computed from Eq. (4.2).

The expected stand-off distances of the cavities are estimated from results of the hybrid simulation of the inner coma of an active comet by Koenders et al. (2015). The simulation shows a contact surface stand-off distance of $r_{sim} = 25$ km for an outgassing rate of $Q_{sim} = 5 \times 10^{27} \text{ s}^{-1}$. Combining this with the $r_{cs} \propto Q^{3/4}$ dependence of the stand-off distance (see Section 2.4.3), yields that the cometocentric distance r_{cs} of the contact surface along the Sun-pointing direction for an outgassing rate Q_{est} can be estimated as

$$r_{cs} = \left(\frac{Q_{est}}{Q_{sim}} \right)^{3/4} r_{sim} \quad (4.3)$$

Applying this relation to the outgassing rate estimates provides the expected stand-off distances of the contact surfaces given in the last column of Table 4.1.

Table 4.1. Times of cavity crossings defined by the MAG instrument (Goetz et al., 2016b), cometocentric distances $r_{s/c}$, heliocentric distances d_h , estimates of the outgassing rates Q from the models proposed by Hansen et al. (2016), and theoretically expected stand-off distances of the contact surfaces r_{cs} .

Date	Time [UT]	$r_{s/c}$ [km]	$u_{s/c}$ [m/s]	d_h [AU]	Q [s^{-1}]	r_{cs} [km]
2015-05-28	21:49:59 - 21:54:03	269	0.8	1.54	2.77×10^{27}	16.1
2016-02-17	06:35:29 - 06:35:44 06:45:32 - 06:46:36	42	0.1	2.38	3.21×10^{26}	3.19

Since the boundaries on the dayside of a comet are non-spherical (see Section 2.4), the latitudinal and longitudinal position of the spacecraft relative to the comet is important when comparing the measured cometocentric distances of the contact surfaces $r_{s/c}$ with the simulation and theoretically expected ones r_{cs} . It is, however, considered unlikely that a factor of more than 10 difference between $r_{s/c}$ and r_{cs} can be explained purely by the elliptical shape of the boundary on the comet, which is also what is found for the majority of cavities crossings in the environment comet 67P studied by Goetz et al. (2016b).

4.1.2 Orientation of the diamagnetic cavity boundary layers (DCBL)

The differences between the observed stand-off distances of the contact surfaces $r_{s/c}$ and the theoretically expected ones r_{cs} might be explained by asymmetric cometary outgassing and irregularities in the solar wind that along with shear plasma flows and other mechanisms can result in instabilities on the contact surface. On the contact surface, these instabilities might result in "bulges" or "fingers" that extend beyond the ion-neutral friction-caused pressure balance with the magnetic field (Goetz et al., 2016b). Whether the structure of the studied cavities agrees with this theory can be tested by studying the orientation of the boundary planes that can be estimated by minimum variance analysis (MVA) of the magnetic field components. In the MVA of a three-component magnetic field signal sampled during a boundary crossing, the resultant direction of least variance is the estimation of the normal to the boundary (see Section 3.2.3).

The MVA normal vectors of the cavity boundaries are shown in Figure 4.2 together with the averaged magnetic field direction before and after the cavity crossings. The normals are computed from intervals spanning over the in-/outbound DCBL crossings. The intervals are chosen visually such that they include the entire gradual decrease/increase of all three magnetic field components and the crossing of the contact surface. The exact time intervals used for the MVA of the DCBL crossings are shown in Table 4.2 along with the CSEQ components of the the estimated normals, \mathbf{n}_{in} and \mathbf{n}_{out} , to the in- and outbound transition layers, and the MVA-determined variances of the vectors. The table additionally shows the CSEQ spacecraft positions at the contact surfaces. Recall that in the CSEQ system, x originates in the comet and points towards the Sun, whilst z is parallel to the solar equatorial plane (see Section 3.2.1). Hence, the spacecraft is located in front of the comet's southern hemisphere during all three events. Also note that in the MVA-vector plots of Figure 4.2, the Sun is to the right whilst the comet is to the left.

From the MVA, it is evident that the structure of the M15 cavity varies considerably from the F16 cavities. The M15 cavity resembles that of the cavity on July 26, 2015, studied by Goetz et al. (2016a) (see Section 3.9): the directions of the normals change only slightly from the inbound to the outbound transitions, whilst the reversal in the averaged magnetic field pointing direction indicates that the magnetic field has been draped around the cavity.

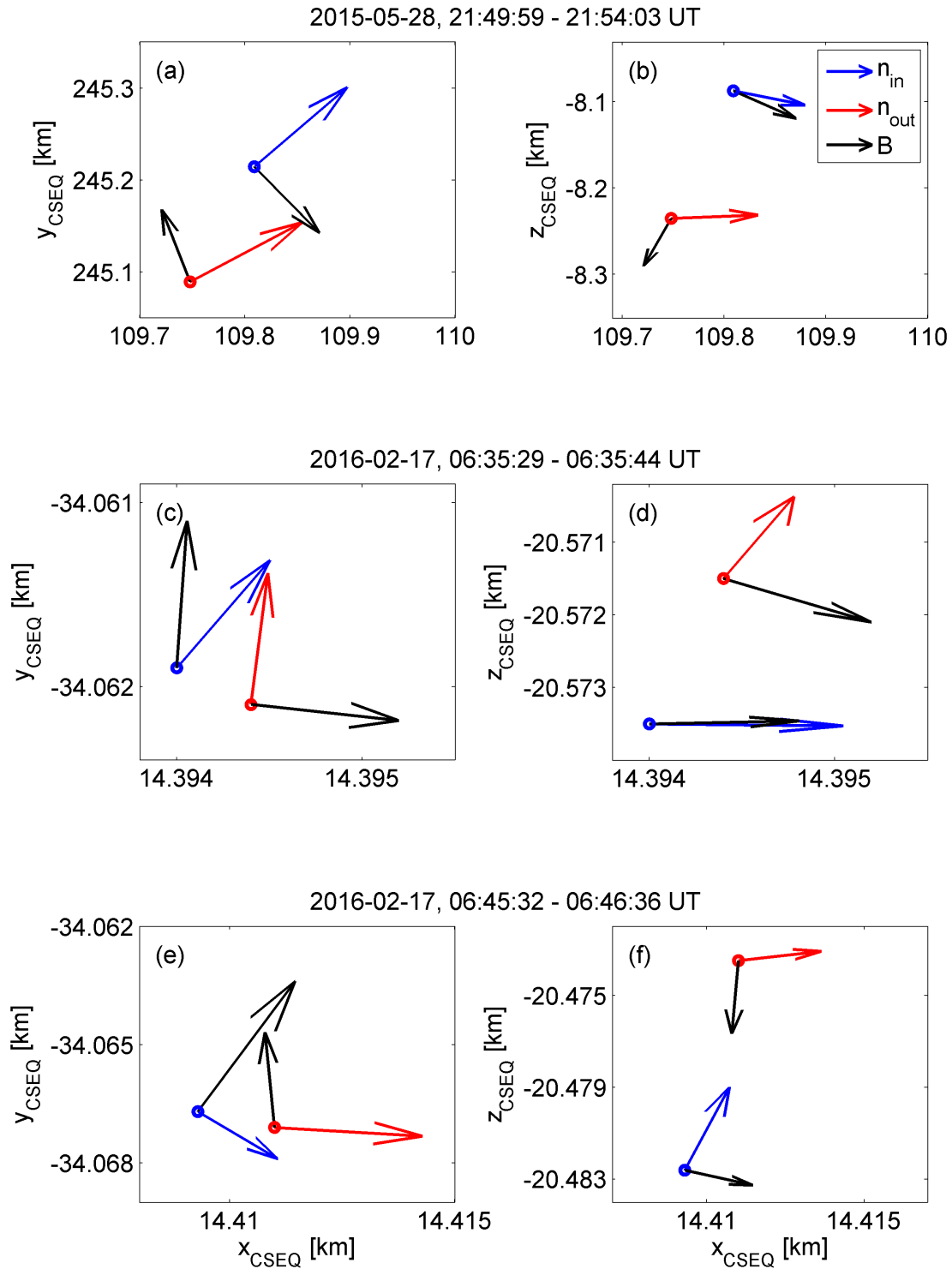


Figure 4.2. In- and outbound DCBL normals, \mathbf{n}_{in} and \mathbf{n}_{out} , and averaged magnetic field directions, \mathbf{B} , before and after the studied cavities. (a)-(b) M15, (c)-(d) F16a, and (e)-(f) F16b. The normals of the boundaries are computed in the transition regions defined in Table 4.2. For the M15 event the averaged magnetic field components are computed over 5 min intervals before and after the transition regions, whilst this interval is 2 min for the F16a and F16b events. Note that the vectors are given in the CSEQ coordinate system. Hence, the Sun is to the right for all figures, whereas the comet is to the left.

Table 4.2. Times for the boundary transitions used in the MVA, s/c positions in CSEQ, estimated normals to the boundaries, and variances of the MVA systems.

Date	Time interval [UT]	s/c (x, y, z) [km]	\mathbf{n}_{in} & \mathbf{n}_{out} (x, y, z)	$(\lambda_x, \lambda_y, \lambda_z)$
2015-05-28	21:47:00 - 21:50:30	(109.81, 245.21, -8.09)	(0.71, 0.69, -0.16)	(1, 2.05, 39.1)
	21:53:30 - 21:55:15	(109.75, 245.09, -8.24)	(0.86, 0.47, 0.22)	(1, 33.7, 60.5)
2016-02-17	06:34:10 - 06:35:34	(14.40, -34.06, -20.57)	(0.65, 0.76, -0.2)	(1, 6.20, 11.9)
	06:35:39 - 06:36:05	(14.40, -34.06, -20.57)	(0.05, 0.94, 0.34)	(1, 3.27, 57.7)
2016-02-17	06:43:58 - 06:45:35	(14.41, -34.07, -20.48)	(0.35, -0.24, 0.90)	(1, 5.03, 16.5)
	06:46:29 - 06:47:03	(14.41, -34.07, -20.47)	(0.99, -0.07, 0.15)	(1, 3.86, 10.4)

It is worth mentioning that the magnetic field magnitude increased by a factor of 2 after the cavity compared to before (see Figure 4.1(a)). This is not expected for a static system with magnetic field draping around an obstacle. Therefore, it is assumed that the cavity bulges on the contact surface are indeed travelling and locally compress the magnetic field. However, if the M15 cavity is the only obstacle compressing the magnetic field in the vicinity of the spacecraft during the observation, this hypothesis fails in explaining why the magnetic field magnitude is largest *after* the cavity. Several cavities are albeit observed during the days neighbouring the event and it is likely that other travelling cavity bulges can be responsible for the observed increase in magnetic field magnitude.

The boundary normals of the F16 events differ strongly from the inbound to the outbound transition. This might indicate that either the spacecraft is passing through only the tip of the cavity "finger" and not through the entire structure, or that the F16 boundaries of the cavities have a greatly varying surface structure. Additionally, the F16 cavities do not show signs of magnetic field draping. Instead, the observed rotation in the averaged magnetic field direction seems to indicate a deflection of the field. The non-draping behaviour of the magnetic field around cavities near comet 67P has been observed on multiple occasions and might also be caused by instabilities that result in non-linear perturbations of the magnetic field in the environment surrounding the cavity or by changes in the field direction during the time the Rosetta spacecraft was inside the cavities (Charlotte Götz, TU Braunschweig, Germany, private communication).

4.1.3 The plasma environment

As mentioned, the evolution of the cometary environment observed by the Rosetta spacecraft in May 2015 differs strongly from that in February 2016. This is partly due to the achieved cometocentric observation distances, and partly due to the fact that comet 67P is only two and a half months from perihelion during M15, whilst the F16 events are observed more than half a year after the comets closest approach to the Sun. It is therefore important to keep in mind that no direct quantitative comparison between the three events is possible, even though the subsequent analysis will show some qualitatively similar features in all events.

The ion and electron energy-per-charge spectrograms of the RPC ion and electron sensor (IES) illustrate the different conditions experienced by the Rosetta spacecraft during the two dates (see Appendix C). However, IES does not provide a good enough time resolution to add information in the characterization of the cavities themselves. The M15 cavity is observed in what Mandt et al. (2016) characterize as the

”outer region”. This region is outside the ion-neutral collisionopause boundary, outside of which collisions between ions and neutrals become negligible. Mandt et al. (2016) argues that this region seems to be located outside the diamagnetic cavity and is likely subject to enhanced magnetic field pile-up, possibly reduced electron densities, and acceleration of water-group ions. The observation of the M15 cavity in the outer region supports the claim that the contact surface is not a static elliptical feature that shields the innermost region of the cometary environment from the solar wind.

The F16 cavities are observed during a time when the solar wind is seemingly detected by the IES ion energy-per-charge spectrogram. The solar wind reveals itself as the two bands of energetic ions at roughly 1 keV/e and 2 keV/e. Since IES does not distinguish between mass, it cannot be excluded that the observed signatures are highly accelerated cometary water-group ions. However, the two time-persistent signals at 1 keV/e and 2 keV/e are good indicators of the solar wind. This is because the solar wind mostly consists of a great abundance of H^+ and a smaller fraction of He^{++} that in the ion energy-per-charge spectrogram results in a strong signal of H^+ at about half the energy-per-charge of the double-charged He^{++} .

Plasma physical quantities

To characterise the nature of the observed plasma, the plasma quantities presented in Section 2.1 are useful. As argued for in Section 3.1 the Debye length gives the characteristic length of the spacecraft sheath, and that instruments within the sheath are measuring plasma that is altered by the presence of both the spacecraft and the instrument itself. Recall from Eq. (2.11) that the Debye length is related to the electron density n_e and temperature T_e by

$$\lambda_D = \sqrt{\frac{\epsilon_0 k_B T_e}{n_e e^2}}$$

The electron density additionally provides an estimate of the plasma frequency of Eq. (2.12):

$$f_p = \frac{1}{2\pi} \omega_p = \frac{1}{2\pi} \sqrt{\frac{n_e e^2}{m_e \epsilon_0}}$$

The average magnetic field magnitudes give an indication of some of the characteristic frequencies that have previously been observed in the inner coma of comets, i.e. the water-group ion and electron gyrofrequencies and the lower hybrid frequency (LHF). Recall that these are given by

$$f_c = 2\pi\Omega = \frac{1}{2\pi} \frac{|q|B}{m} \quad \text{and} \quad f_{LH} \approx \frac{1}{2\pi} \sqrt{\Omega_{ce}\Omega_{ci}}$$

In sweep mode, the LAP instrument provides estimates of both n_e and T_e . However, since the LAP instrument is in electric field mode during the cavity crossings of this study, no LAP sweeps are done in the considered time intervals. Instead, by assuming that the average densities and temperatures do not change much within a few hours, LAP sweeps neighbouring the electric field modes are used to make estimates of n_e and T_e for both days. Alternatively, the electron density can be measured by the RPC mutual impedance probe (MIP) instrument (see Section 3.2.4). However, no reliable MIP estimates are available for the M15 event, and to make the methods for obtaining estimated parameters for the two dates comparable, the MIP electron density estimates for the F16 events are not included in this section. It is, however, shown later in Figure 4.4 that the MIP electron densities estimated during the F16 events show a similar mean value as the estimate gained from the LAP sweeps.

Table 4.3. Estimates of the electron densities n_e , electron thermal energies $k_B T_e$, and magnetic field magnitude B shown together with the estimated Debye length λ_D , water-group ion and electron plasma frequencies, f_{pi} and f_{pe} , electron and ion gyrofrequencies, f_{ce} and f_{ci} , and LHF f_{LH} . The ion density is assumed to be of the same order of magnitude as the electron density. The densities and electron temperatures are obtained from the LAP instrument overview plots, a few hours before/after the studied events, provided by the RPC-LAP Uppsala team. This gives rough estimates of the quantities whenever the LAP instrument is in the bias sweep mode. The two values for M15 event indicate the averages before and after the cavity.

	2015-05-28	2016-02-17
n_e [cm ⁻³]	100	1000
$k_B T_e$ [eV]	5	5
B [nT]	24 - 45	9
<i>Derived Quantities</i>		
λ_D [m]	1.7	0.53
f_{pi} [kHz]	0.50	1.6
f_{pe} [kHz]	90	2.8×10^2
f_{ce} [kHz]	0.672 - 1.26	0.252
f_{ci} [mHz]	20.5 - 38.4	7.7
f_{LH} [Hz]	3.71 - 6.92	1.39

Table 4.3 shows the estimated electron density and temperature, averaged magnetic field magnitudes and corresponding characteristic frequencies for the cavity crossings. Note that the two values of the magnetic field magnitudes and corresponding gyrofrequencies and LHF for M15 are the averages before and after the cavity.

The characterization of the plasma environment experienced by the Rosetta spacecraft during the cavity events studied in this work, are crucial in the interpretation of the studied electric fields signatures. Recall that LAP1 and LAP2 are mounted at the end of booms of length 2.24m and 1.62m, respectively. Since the sheath extends further than one Debye length, i.e. 1.7m for M15 and 0.53m for F16, the probe measurements are done within the sheath. Hence, the probe potentials picked up by LAP1 and LAP2 are only a fraction of the true spacecraft potential, as illustrated in Figure 3.6.

The electric field mode of the LAP instrument has two sampling modes: a low- and a high-frequency mode (see Section 3.2.2). The low-frequency mode samples data with a sampling frequency of 57.8Hz for 31 s. Hence, the maximum bandwidth of the low-frequency electric field mode is 32mHz – 28Hz. Frequencies below 1 Hz are not investigated in this study due to the not yet established reliability of signatures in this range (Karlsson et al., 2017). Hence, in the low-frequency mode, only the LHF out of the suggested frequencies might be detected.

The high-frequency mode has a sampling frequency of 18.75kHz and samples for 23ms every 32s, which gives a bandwidth of 43.5Hz – 8kHz. Therefore, if the electron gyrofrequency is present it might be detected in the high-frequency data. However, neither the electron plasma frequency f_{pe} , nor the water-group ion gyrofrequency f_{ci} were within the bandwidth of either the low- or high-frequency sampling mode of the LAP electric field modes during the M15 and F16 events.

4.1.4 Electric field signatures

The electric field fluctuations during the cavity crossings are estimated as the difference in probe potentials V_1 and V_2 relative to the spacecraft divided by the probe separation (see Section 3.2.2). Figure 4.3 and 4.4 show the calibrated probe potentials and derived electric fields for the M15 and F16 events, whereas the probe calibrations themselves are given in Appendix B. The electric fields are detrended by removing a moving average that spans over 57 data points, i.e. an average over roughly 1 s. Due to availability of the ROSINA-COPS and MIP data during the events, the M15 event includes the neutral density n_n derived from the ROSINA-COPS instrument, whereas the MIP electron density n_e is given for the F16 events.

The temporal positions of the contact surfaces defined by Goetz et al. (2016b) from the magnetic field components of Figure 4.1 are imposed on the electric field plots as vertical black lines. Along with these are the beginning/end of the in-/outbound DCBLs and contact surface positions defined from the electric field estimates. These are found by eye from variations in the means and variances of the electric field (see Appendix D). The means and variances are computed over intervals of 1 s, and hence there is a 1 s uncertainty of the defined times.

The chosen criteria for a cavity observed in the electric field are that both the mean and variance are small compared to the values outside the cavity. The inbound DCBL is then limited by the beginning of the cavity and the mean and variance peaks preceding the cavity, such that both the mean and variance gradually decrease throughout the inbound DCBL. The outbound DCBL is characterized by a small increase in the mean value relative to what was found inside the cavity and limited by a sudden sharp increase in both the mean and variance of the electric field. The times for the crossings are shown in Table 4.4.

Note, however, that several intervals obey the above-mentioned cavity criteria in the electric field without having the magnetic field components going to zero. Hence, a study of the mean and variance of the one-component electric field estimate obtained by the LAP instrument alone is not a sufficient method to determine the positions of diamagnetic cavities in the environment of comet 67P. Also note that the temporal positions of the cavities would be differently defined if only one component of the magnetic field was available (see e.g. Figure 4.1(a) where B_x and B_y goes to zero prior to B_z). Hence, a better definition of the limits of the diamagnetic cavity might be proposed if a three-dimensional electric field estimate was available.

Table 4.4. Temporal positions of the beginning of the electric field in- and outbound boundary layers, t_{DCBLin} and $t_{DCBLout}$, and contact surfaces defined by the electric field estimates, t_{cE} , and the magnetic fields t_{cB} . The magnetic field-defined contact surface positions are given already in Table 4.1, but are include again here for comparative reasons.

Date	t_{DCBLin} [UT]	$t_{DCBLout}$ [UT]	t_{cE} [UT]	t_{cB} [UT]
2015-05-28	21:47:08	21:54:11	21:50:14 - 21:53:54	21:49:59 - 21:54:03
2016-02-17	06:34:12	06:35:48	06:34:30 - 06:35:40	06:35:29 - 06:35:44
	06:44:02	06:46:38	06:45:20 - 06:46:20	06:45:32 - 06:46:36

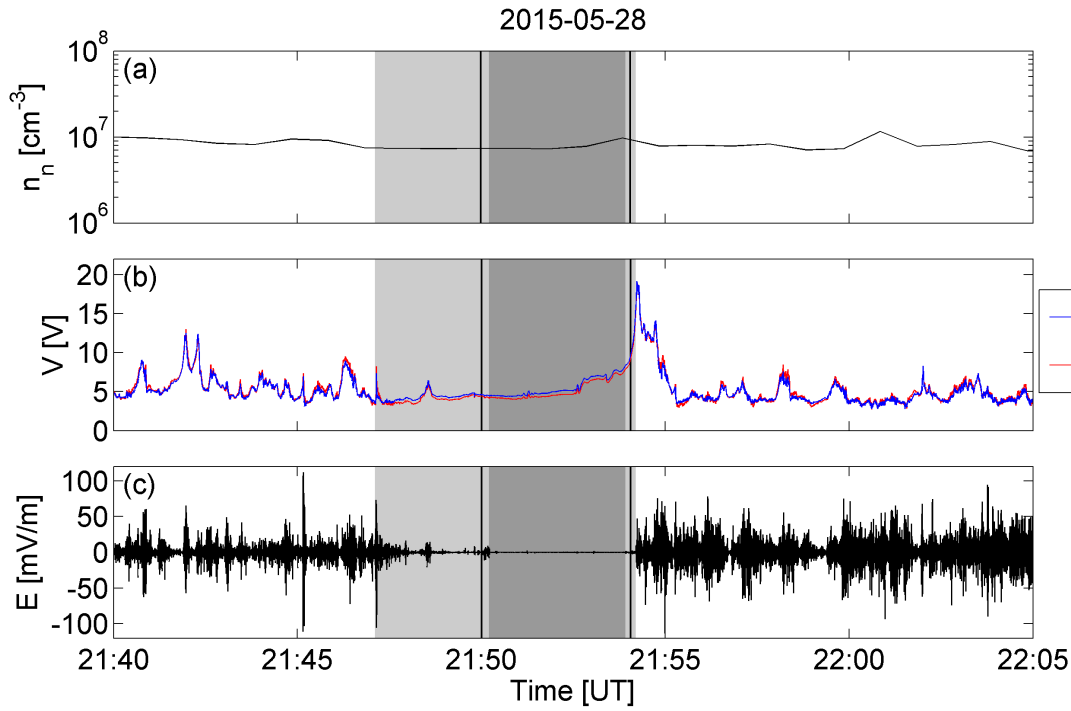


Figure 4.3. (a) ROSINA-COPS neutral gas density with a 1 min sampling period, (b) calibrated LAP probe potentials V_1 and V_2 and (c) moving average-corrected electric field fluctuations during the M15 cavity crossing. The shaded areas mark the DCBLs and cavity as defined by the electric field, whilst the vertical black lines mark the magnetic field cavity limits.

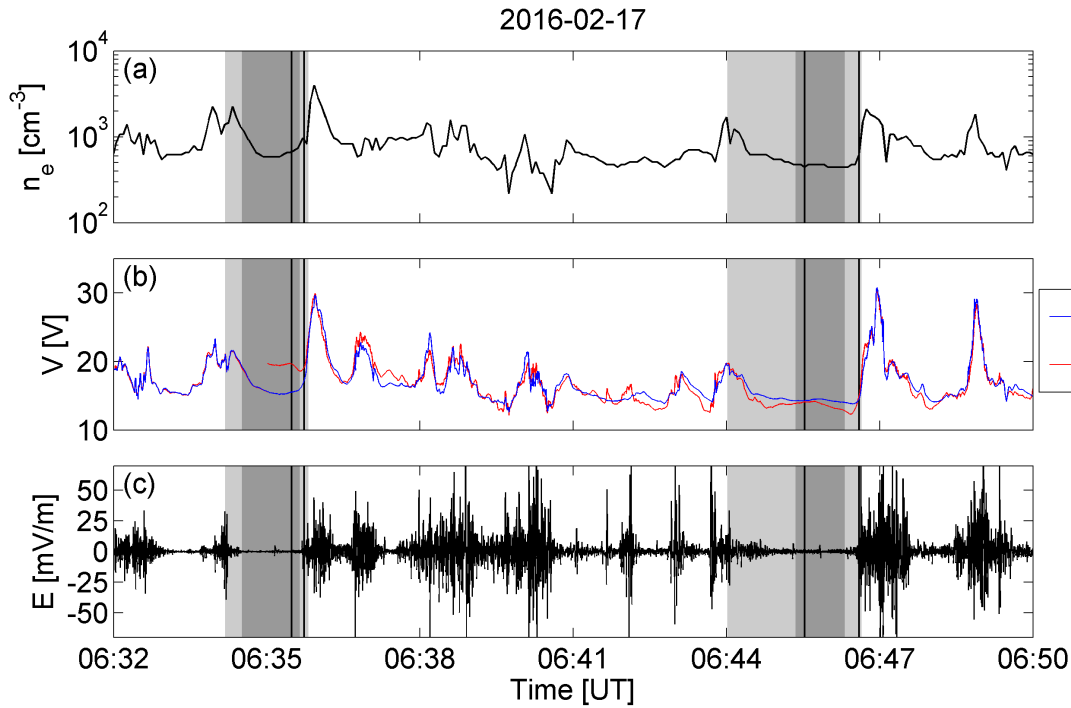


Figure 4.4. (a) MIP electron densities of a roughly 4.4 s time resolution, (b) calibrated LAP probe potentials V_1 and V_2 and (c) moving average-corrected electric field fluctuations during the F16 cavity crossings. The jump in probe potential of LAP2 at 06:35 UT occurs due to a change in calibration. The vertical lines and shaded areas are defined as those in Figure 4.3.

Throughout the entire M15 event, the probe potentials follow each other well, suggesting that the probes are in similar environments. This is not the case for the F17 events. At 06:35 UT there is a jump in the V_2 value of Figure 4.4(b). This is caused by a change in calibration. At this time the solar aspect angle (SAA) decreases to a value below 107° , indicating that LAP2 might go into shadow (see Section 3.2.1). When LAP2 goes into shadow, the total electron current to the probe $I_{tot} = I_e - I_{ph}$ increases, due to a decrease in the photoemission current. This results in a more negative probe potential. Since the spacecraft is negatively charged, the potential difference V_2 between LAP2 and the spacecraft body will decrease. LAP1 is still illuminated, and hence the difference between V_1 and V_2 increases, employing a change in calibration. In addition, the change in the SAA causes greater fluctuation in V_2 relative to V_1 . However, the probes and the estimated electric field still pick up features that seem to be characteristic for observed cavity crossings around the comet.

The cavity limits defined by the electric field follow relatively well the ones observed in the magnetic field, considering the uncertainties related to defining the limits from only one component of the electric field estimate. For two of the three cavities studied herein, the electric field picks up a long inbound boundary of roughly the same length as the cavity itself, and a short outbound boundary followed by a rapid increase in the electric field fluctuation level, as also observed in the magnetic field. Only the limits defined for the F16a strongly mismatch the magnetic field limits by including a large part of the magnetic field-defined inbound boundary in the electric field-defined cavity. However, in the electric field definition of the F16a cavity, the MIP data and probe potentials show that there is a significant gradient in the electron density inside the first half of the cavity. This gradient seems to be related to a general increase in electron density at the beginning of the inbound DCBL for all three cavities. It seems more likely that this gradient is limited to the DCBL, and hence should not be within the cavity. It is therefore suggested to modify the the above the definition of the contact surface position to include that the probe potentials should be rather constant within the cavity. Applying this on the F16a cavity makes the limits of the electric field-defined cavity fit those defined by the magnetic field better. In addition to an electron density increase at the beginning of the inbound DCBL, the outbound DCBL is subject to a sharp peak in electron density. These peaks are further studied in the following section that compares the LAP1 probe potential to the MIP electron density estimate.

In contrast to the MIP electron density, the neutral gas density estimates provided by the ROSINA-COPS instrument during the M15 event stay rather constant throughout the cavity crossing and do not seem to be significantly affected by the cavity, as also expected from theory. This statement, however, has to be treated with care since the time resolution of the ROSINA-COPS instrument is poor relative to the scale of the cavity and its boundaries. Hence short-lived variations in the neutral density might be present even though not observable in the data.

The ROSINA-COPS neutral density estimate of $n_n \approx 10^7 \text{ cm}^{-3}$ can, nevertheless, be used to evaluate whether the outgassing rate Q during the M15 event varies strongly from the one estimated in Table 4.1, and hence whether the theoretically expected stand-off distance of the contact surface might be larger than the one presented in the table. For the estimate of Q , the neutral gas speed is set to $u_n = 700 \text{ m/s}$ (Hansen et al., 2016), whilst the photodestruction rate is given the value $v_d = 9.3 \times 10^{-6}/d_h[\text{AU}] \text{ s}^{-1} = 6.0 \times 10^{-6} \text{ s}^{-1}$ (Simon Wedlund et al., 2017). With a cometocentric distance of $r_{s/c} = 269 \text{ km}$, the Haser

model of Eq. (2.23) estimates the outgassing rate to be

$$Q = 4\pi u_n r^2 n_n \exp\left[\frac{V_d r}{u_n}\right] = 6.4 \times 10^{27} \text{ s}^{-1}$$

which is only a factor 2 different from the value found by the Hansen-model, and therefore not enough to explain the large difference between $r_{s/c}$ and r_{cs} for the M15 event in Table 4.1.

Comparison between ICA, LAP and MIP

For all events, the inbound DCBL is initiated by an increase ($\Delta V \approx 5 - 10 \text{ V}$) in the probe potentials, whilst the outbound boundaries coincide with a stronger peak ($\Delta V > 10 \text{ V}$) in the potentials. As argued in Section 3.2.2, such increases relative to the spacecraft can be an indication of increases in the electron densities n_e . The electron density of the plasma observed by the Rosetta spacecraft can be estimated by the MIP instrument (see Section 3.2.4) or by the voltage sweep mode of the LAP instrument (see Section 3.2.2). Unfortunately, no reliable MIP electron density estimates are available during the M15 event, and hence it cannot be verified that the variations in the probe potentials during the M15 event are indeed caused by changes in the electron density. However, during the F16 events, the MIP instrument delivers data in burst mode with a time resolution of about 4.4 s. These are shown in Figure 4.4(a), and a qualitative comparison between these and the probe potentials in Figure 4.4(b) indicate that, on this date, fluctuations in the potentials (disregarding the LAP2 shadowing) are indeed related to changes in the electron density. Nemeth et al. (2016) mention that during the summer of 2015, cavity crossings observed by the MIP electron densities show little fluctuations and are of the order of 800 cm^{-3} inside the cavity, but increase by several 100 cm^{-3} at the boundaries, similar to what is observed for the F16 events of this study. They explain the DCBL electron density increase by a trapping of low-energy electrons by the DCBL magnetic field, and relate the increased electron density to increased spacecraft charging that, in turn, accelerates ions near the boundary, resulting in observations of increased ion fluxes at energies 10 – 40 eV.

A quantitative comparison between changes in the probe potentials and electron density fluctuations can be done using the expression of the spacecraft potential in Eq. (3.13), for a negatively charged spacecraft, where the total current is assumed to consist of only the photoemission current I_{ph0} to the spacecraft and the electron current. The equation states that the spacecraft potential $V_{s/c}$ is related to the electron density n_e and temperature T_e through

$$V_{s/c} = -\frac{k_B T_e}{e} \log \left[\frac{A_{s/c} n_e e}{2I_{ph0}} \sqrt{\frac{2k_B T_e}{\pi m_e}} \right]$$

where $A_{s/c}$ is the current collecting area of the spacecraft, and m_e is the mass of the electrons. For the F16 events, the spacecraft potential is indeed negative relative to the plasma, as can be seen in the positive probe potentials measured relative to the spacecraft and by the effect of the shadowing of LAP2 in Figure 4.4(b).

Due to the shadowing of LAP2, only LAP1 is considered in the comparison between the potential and the MIP electron densities. The MIP instrument is, in addition, attached to the same boom as LAP1 (see Figure 3.2), yielding that LAP1 and MIP are relatively close to each other. Recall that LAP1 is mounted at the end of the boom, 2.24 m from the spacecraft body (see Section 3.2.2). With the LAP sweep estimates of T_e and n_e (that agree with an estimate of the average electron density in the MIP data from Figure 4.4(a)), the Debye length, and hence the characteristic spacecraft sheath length scale, is

estimated to be $\lambda_D = 0.53$ m (see Table 4.3). Hence, LAP1 is expected not to be deep within the spacecraft sheath, but might still be influenced by the sheath (in addition to the probe's own sheath, as illustrated in Figure 3.6). It is therefore assumed that the potential V_1 measured at LAP1 relative to the spacecraft is only a fraction of the negative of the full spacecraft potential.

In the comparative study between the lower boundary of the ICA spectrogram and the spacecraft potential estimate gained from LAP1 sweeps, Odelstad et al. (2016) find that in the vicinity of comet 67P the fraction of the spacecraft potential picked up by the LAP1 sweeps is between 0.7 and 0.9. Using the value 0.9 due to the short Debye length on F16, the probe potential V_1 can be related to the electron density and temperature by

$$V_1 \approx -0.9V_{s/c} = \frac{0.9k_B T_e}{e} \log \left[K n_e \sqrt{\frac{k_B T_e}{e}} \right]$$

by introducing the constant

$$K = \frac{A_{s/c} e}{2I_{ph0}} \sqrt{\frac{2e}{\pi m_e}}$$

From the LAP sweeps neighbouring the electric field mode sampling, the electron temperature is estimated to be $k_B T_e = 5$ eV (see Table 4.3). By assuming this temperature inside the cavity, the value of the constant K can be estimated from the MIP electron density and LAP1 probe potential. Here, the MIP electron density measurements are assumed not to be affected by the presence of the spacecraft sheath. The resultant values of K for both F16 cavities are shown in Table 4.5 together with its average value. Figure 4.5 shows the F16 time-evolution of the electron temperature computed from the MIP electron density n_e , LAP1 probe potential V_1 downsampled to the sampling of n_e , and estimated value K_{avg} .

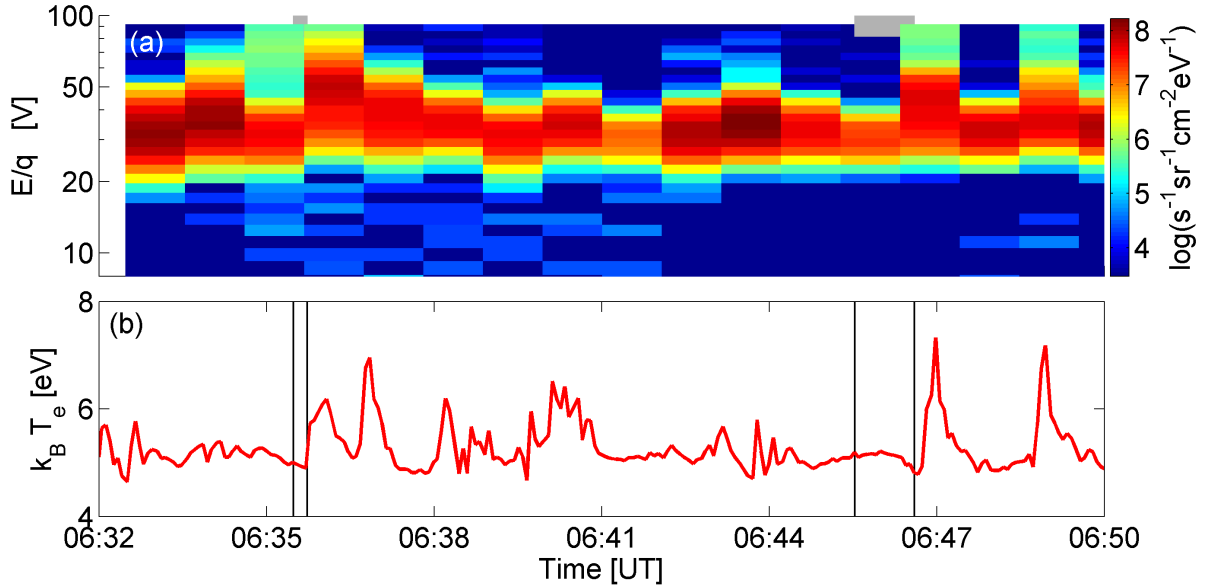


Figure 4.5. (a) High time resolution ICA ion flux spectrogram with shaded areas marking the cavities as observed by the MAG instrument. (b) Estimated electron temperature from MIP electron density n_e and LAP1 probe potential V_1 downsampled to the sampling of n_e . A temperature of $k_B T_e = 5$ eV is assumed inside the cavities in the computation of the constant K_{avg} . The vertical black lines are defined as the shaded area in (a).

Table 4.5. Probe potential, electron density and estimated K value inside the F16 cavities for an assumed temperature of $k_B T_e = 5$ eV. K_{avg} is the average of K for the F16a and F16b events.

Time [UT]	V_1 [V]	n_e [cm ⁻³]	K [cm ³]	K_{avg} [cm ³]
06:35:36	15.7	741	0.0198	0.0211
06:46:22	13.9	441	0.0223	

The temperature profile presented in Figure 4.5(b) indicates that, at the inbound DCBL, electrons are at the same temperature as within the cavity. At the outbound DCBL the electron density peak seems to be related to an electron heating of 1 – 2 eV. Note, however, that the estimated temperature profile builds on the assumption that the fraction of the spacecraft potential picked up by LAP1, i.e. $V_1/V_{s/c}$, is constant throughout the events. This might not be true, since variations in the electron density and temperature influence the magnitude of the spacecraft potential and the Debye length, thus altering the potential profile of the sheath. However, introducing uniformly distributed random numbers for $V_1/V_{s/c}$ in the range from 0.7 – 0.9 gives a similar temperature profile as in Figure 4.5(b), and the noise level introduced by the random numbers is not large enough to explain the temperature peaks. It is therefore concluded that the apparent electron temperature increases at the outbound DCBLs cannot be entirely caused by changes in $V_1/V_{s/c}$. Additionally, that electrons could be heated at the outbound boundary of the observed diamagnetic cavities is physically reasonable since the boundary contains sharp variations in the electromagnetic fields and electron densities and hence may be subject to waves and instabilities related to free energy that might lead to heating. A specific mechanism is, however, to the author’s knowledge still not found.

The related ICA spectrogram of Figure 4.5(a) additionally indicates ion energy increases at the outbound DCBL. Also note the apparent average ion energy increase coinciding with the electron temperature peak at about 06:49 UT after F16b. This might indicate that the increased ion energy is related to the proposed electron temperature increases. However, since the time resolution of the ICA instrument is 1 min, and hence on the order of the cavity time scales, it is an open question whether the energy increase in the ICA spectrogram is significant. The ICA energy signatures might, however, as well be caused by increases in the spacecraft potential that leads to further acceleration of ions, as observed in the IES study by Nemeth et al. (2016). This is supported by the lower boundary of the ICA spectrogram being about 20 V, which is slightly higher than the averaged probe potential of LAP1, and fluctuating with changes in V_1 . With reference to Odelstad et al. (2016), this suggests that the spacecraft potential is approximately $V_{s/c} \approx -20$ V within the cavities, and that LAP1 does indeed only pick up a fraction of this value.

4.2 Spectral signatures of the electric and magnetic fields

The features observed in Figure 4.1(a) by the MAG instrument during the M15 event are typical for cometary cavity crossings by the Rosetta spacecraft (Goetz et al., 2016b), and show electric field signatures that follow the behaviour of the magnetic field well. Studied of the electric field spectrograms, however, unravels further information about the field fluctuations, and the nature of the cavity itself.

Figure 4.6 and 4.8 show the Fourier (a)-(c) and Morlet wavelet (d) electric field spectrograms during the M15 and F16 events, respectively. Since the sampling frequency of the electric field mode is $f_s = 57.8$ Hz, the highest achievable frequency in the spectrograms is 28 Hz. The three Fourier spectrograms are computed from 10 s sub-intervals with a 50% overlap using different degrees of windowing and

detrending. The choice of 10 s sub-intervals yields that the lowest detectable frequency is 0.1 Hz. The gaps in the F16 electric field Fourier spectrograms of Figure 4.8 at 06:35 UT appear due to the change in probe calibration caused by the probable shadowing of LAP2.

For the M15 event, the Fourier spectrogram of Figure 4.6(a) is computed from sub-intervals with the mean value removed from each point in the time series, whilst the panel (b) additionally applies a Hanning window to the sub-intervals. The panel (c) applies a Hanning window to the electric field sub-intervals after subtracting a moving average of span 1 s from the field estimate.

The panel (a) Fourier spectrogram of the F16 events are computed in the same way as for M15 in Figure 4.6(a). Panel (b) is computed from moving average-corrected sub-intervals with an applied Hanning-window, as for M15 in Figure 4.6(c). During the F16 time interval, the periodically appearing data gaps in the LAP electric field mode sampling (see Section 3.2.2) causes vertical lines of artificially high power in the spectrogram of panel (b). To overcome the artificial high-power PSDs caused by the presence of data gaps, the gaps are filtered out in Figure 4.8(c). Each data gap-free interval is split into five sub-intervals of moving average-corrected and windowed electric field data that are slightly longer than 10 s and have a 50% overlap (as illustrated in Figure 3.14). Data gap-filtering causes a loss in information. Since they do not seem to have any strong and consistent influence on the spectrograms of Figure 4.6, the data gaps are not filtered out from the M15 data.

Figure 4.7 and 4.9 show the corresponding magnetic field spectrograms that are computed in a similar fashion as Figure 4.8(c) for comparative reasons. The magnetic field is given in the electric field coordinate system introduced in Section 3.2.2, which is also the case throughout this section if nothing else is stated. This gives the possibility of distinguishing the component of the magnetic field parallel to that of the electric field estimate B_1 , from the perpendicular ones, i.e. B_2 and B_3 . Note the rather time-persistent signature below 5 Hz in all magnetic field components of Figure 4.7 and the signature around 3 Hz in the B_2 component. These are, as well as the garland shaped signatures in the magnetic spectrograms during the F16 events, caused by the spacecraft reaction wheels (see Section 3.2.3) and are not inherent signatures of the plasma environment in the inner coma of comet 67P.

The M15 electric field Fourier spectrograms of Figure 4.6(a)-(c) illustrates the effect of windowing and detrending the signal: As explained in Section 3.3.1, the Fourier spectra of an unwindowed signal might show artificially high power in the high-frequency range of the spectra, if the periodicity assumption of the fast Fourier transform is not fulfilled. These can be filtered out by windowing the signal. Since the spectra of the windowed signal in Figure 4.6(b) shows a depression of the power in the high-frequency range (> 10 Hz) compared to the spectra of the unwindowed signal, it is suspected that the high power at frequencies above 10 Hz in Figure 4.6(a) might be caused by an asymmetry between the sub-interval start and end points and not by real physical phenomena. Hence, panel (b) is assumed to provide more trustworthy results than panel (a). Additionally detrending the time series by subtracting a moving average of span 1 s reduces the power below 1 Hz (see (b) and (c)). The reliability of the low-frequency signature of the LAP instrument electric field mode has not yet been established (Karlsson et al., 2017), and it is not in the scope of this work to do so. Therefore, a removal of these low-frequencies is proposed, and the moving average-corrected signal with an applied Hanning window is chosen for the subsequent analysis of the M15 event.

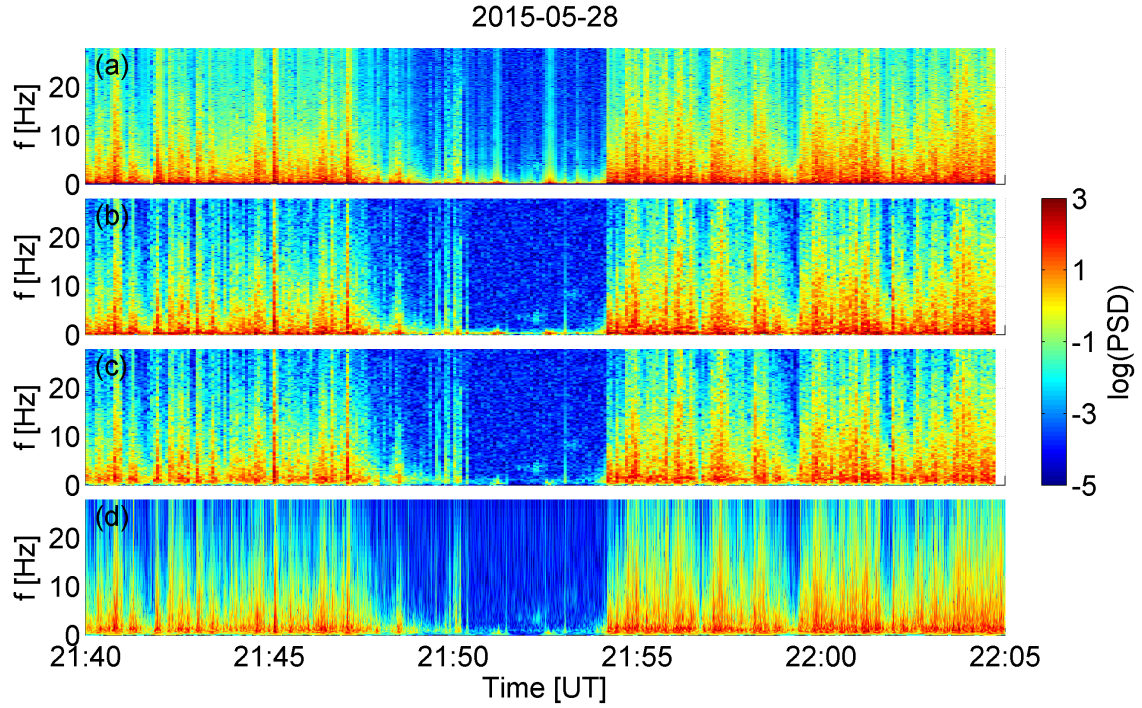


Figure 4.6. Electric field spectrograms computed with the Fourier (a) - (c) and Morlet wavelet (d) methods for the M15 cavity crossing. In the Fourier spectrograms, the sub-intervals are 10 s long and have a 50% overlap. (a) No window, mean removed from sub-intervals. (b) Hanning windowed, mean removed from sub-intervals. (c) Hanning windowed and moving average corrected sub-intervals. Note that the same color scale is used for all four spectrograms.

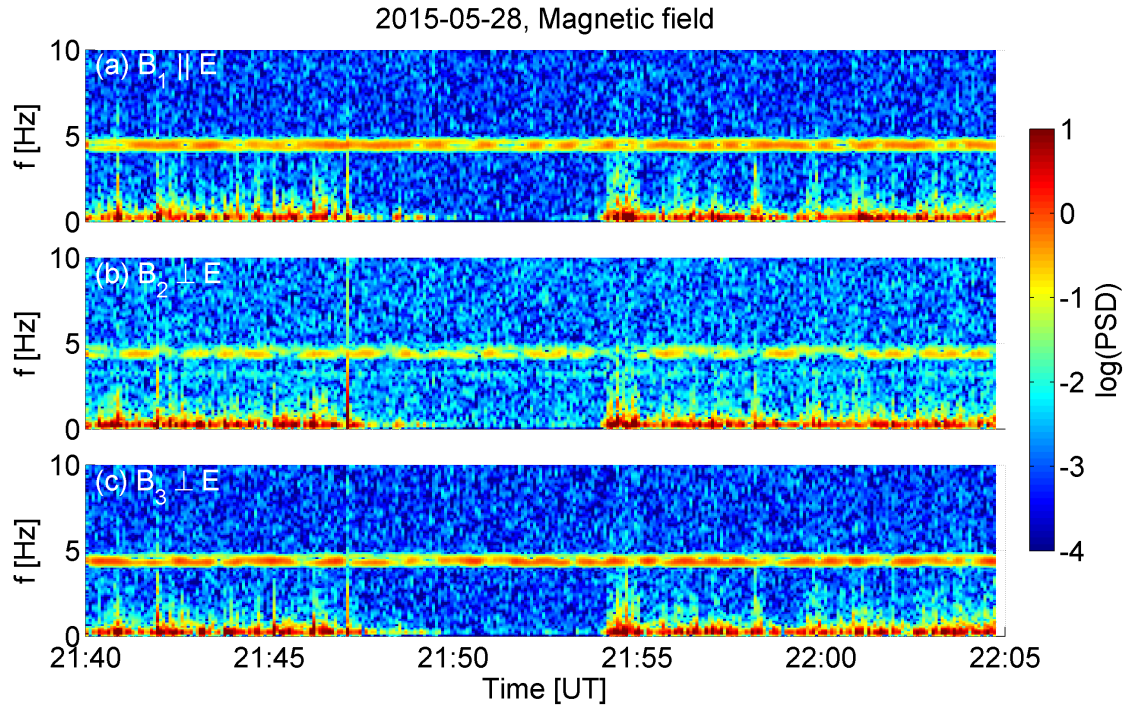


Figure 4.7. Magnetic field spectrograms computed from the Fourier method. The sub-intervals are Hanning-windowed and mean-detrended of length 10 s with an overlap of 50%. (a) $B_1 \parallel E$, (b) $B_2 \perp E$, and (c) $B_3 \perp E$.

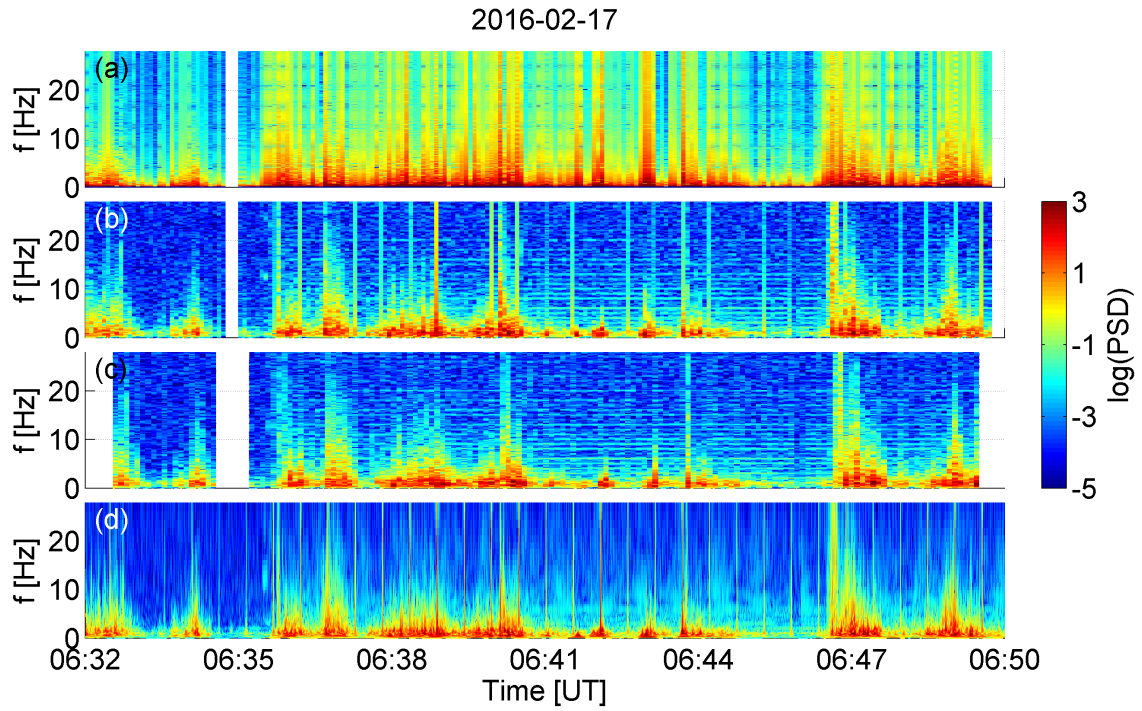


Figure 4.8. F16 electric field spectrograms computed with the Fourier (a)-(c) and Morlet wavelet (d) methods. The Fourier spectrograms use 10 s time intervals with 50% overlap. (a) No window, detrended by removing mean in each sub-interval. (b) Hanning-windowed and moving average-corrected sub-intervals. (c) Hanning-windowed and moving average-corrected sub-intervals between data gaps. Note that the colorbar is the same for all four spectrograms and is similar to the one in Figure 4.6.

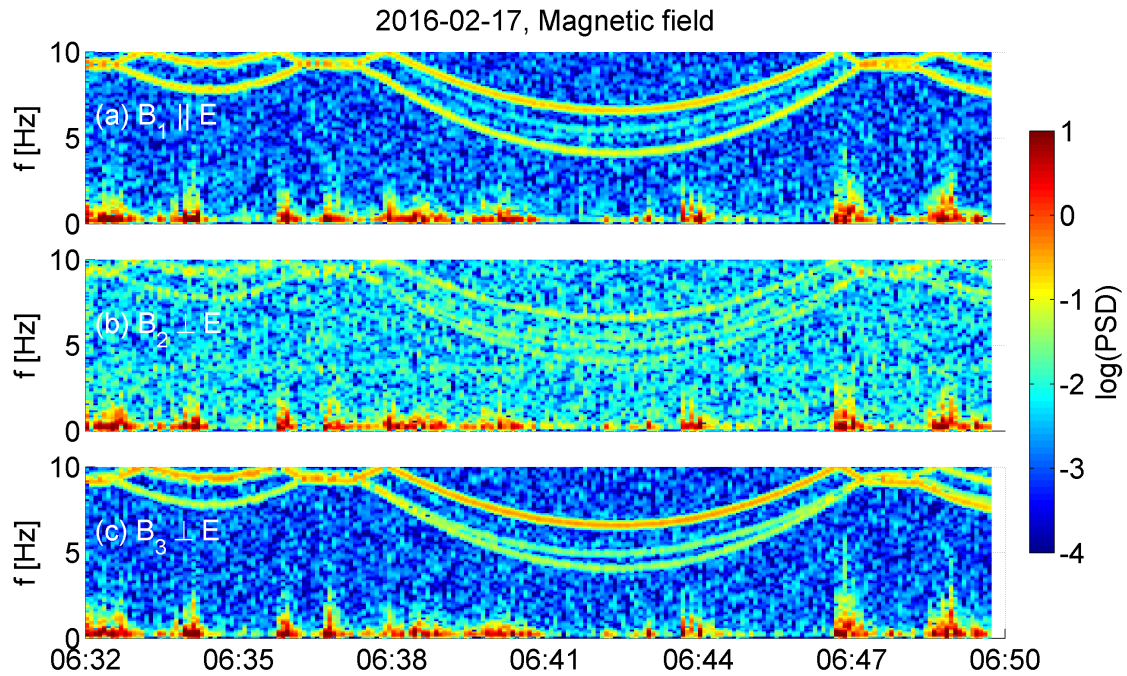


Figure 4.9. Magnetic field component spectrograms computed from the Fourier method. The sub-intervals are Hanning-windowed and mean-detrended of length 10 s with an overlap of 50%. (a) $B_1 \parallel E$, (b) $B_2 \perp E$, and (c) $B_3 \perp E$.

A suppression of the highest ($> 10\text{Hz}$) and lowest ($< 1\text{Hz}$) frequencies is also seen for the F16 spectrograms when comparing the unwindowed, mean-corrected spectrogram of Figure 4.8(a) with the Hanning-windowed, moving average-corrected spectrogram of Figure 4.8(b). Figure 4.8(c) additionally succeeds in filtering out the effects of the data gaps. Therefore, this method is considered the optimal choice for the subsequent analysis. Hence, whenever nothing else is mentioned, the "Fourier spectrogram of the F16 events" refers to as the method displayed in Figure 4.8(c).

From a visual inspection of the spectrograms for both days, it is seen that the signatures seen in the electric field Fourier spectrogram correspond to features in the Morlet wavelet spectrogram, when taking into consideration that the time and frequency resolution of the Morlet wavelet method differs from that of the Fourier method. This supports the assumption that the selected sub-intervals for the Fourier analysis are time-stationary enough to give reasonable spectra. Ultimately, this proposes that the signatures seen in the electric field spectrograms are physical features caused by either the plasma, the spacecraft or the instrument itself, and not by the method. However, the F16 Morlet wavelet method of Figure 4.8(d) also shows vertical lines for every half a minute appearing at the same times as those in Figure 4.8(b). These are, again, interpreted as being caused by the sampling data gaps and implementation of the method, but are not filtered out in this work, since the main purpose of the Morlet wavelet spectrograms is the support the findings of the Fourier method.

The M15 electric and magnetic field spectrograms of Figure 4.6 and 4.7 reveal that outside the cavity, waves at all frequencies are excited with a power that decreases with increasing frequencies. This is further studied in Section 4.2.1. Inside the cavity, these features disappear after undergoing a gradual decrease in power during the inbound DCBL. Two striking features within the M15 cavity are the low-frequency peaks at roughly 3 – 4 Hz and 8 Hz seen for less than 1 min and 30 s, respectively. These frequencies are not in the water-group ion plasma frequency range (see Table 4.7 in Section 4.2.2 for value) that have previously been observed in AMPTE artificial diamagnetic cavity and inside cavities at comet 67P (e.g. Gurnett et al. (1986) and Gunell et al. (2017)). The nature of these low-frequency wave signatures are studied in Section 4.2.2 following an investigation of the signatures outside the cavity.

As for the M15 event, the F17 cavities display a low-power spectrogram signature and are surrounded by a plasma in which electric field waves throughout the entire frequency range are present. The short peak at about 12 Hz appearing shortly before leaving the F16a cavity at 06:35:44 UT is difficult to interpret, since it appears in only a few PSDs and at the time when persistent horizontal lines become present in the spectrogram. These time-persistent peaks appear shortly after the change in probe calibration in both Figure 4.8(b), (c) and (d), and will from now-on be termed the "horizontal lines" of the spectrograms.

Horizontal lines

In the Fourier spectrograms, horizontal lines appear throughout nearly the entire frequency range investigated by the LAP instrument low-frequency electric field mode. The Morlet wavelet spectrogram only captures the peaks at the highest power and the lowest frequencies, and above a frequency of 10Hz they are not distinguishable from the background signal. This is probably caused by the better frequency resolution in the low-frequency range than in the high-frequency range of the Morlet wavelet transform as argued for in Section 3.3.2. Therefore, to highlight the time-persistent features, Figure 4.10 provides zoom-ins of the Fourier and Morlet wavelet spectrograms of the F16b cavity and its boundary layers in the frequency range 0 – 10Hz with a narrower power range than the one for the spectrograms in Figure 4.8.

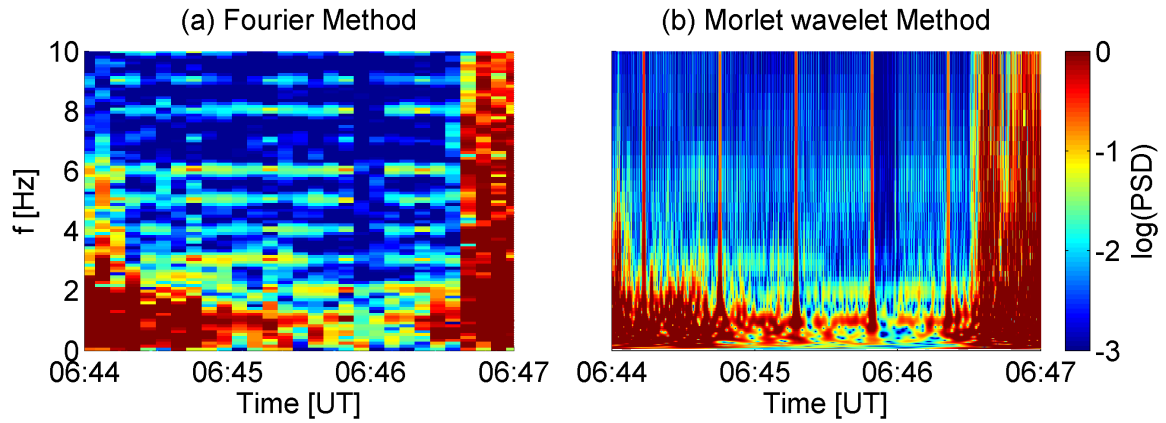


Figure 4.10. Zoom-ins on Fourier and Morlet spectrograms of Figure 4.8(c) and (d). The horizontal lines of highest power and lowest frequencies in the Fourier method spectrogram (a) are also visible in the Morlet wavelet spectrogram (b).

To investigate the frequencies corresponding to the horizontal line power peaks, the PSDs of the Fourier and Morlet wavelet spectrograms are averaged over time. Since the peaks are persistent with time, any time interval can be chosen for the computation of the averages. The F16b cavity at 06:45:32 - 06:46:36 UT (see Table 4.1) and its inbound DCBL is used as the preferred interval. This is chosen in order to reduce the effect of other wave features in the PSD and make the lowest-frequency peaks visible in the average.

As pointed out, the Morlet wavelet spectrogram of Figure 4.8(d) contains periodically appearing PSDs of artificially high power as an effect of the data gaps. To be able to distinguish the horizontal line signatures in the Morlet wavelet spectrogram, the high-power PSDs are filtered out in the computation of the average. The resulting Fourier and Morlet spectra are shown in Figure 4.11. The Morlet wavelet averages are displayed over three intervals separated by data gaps during the in-bound DCBL and within the cavity.

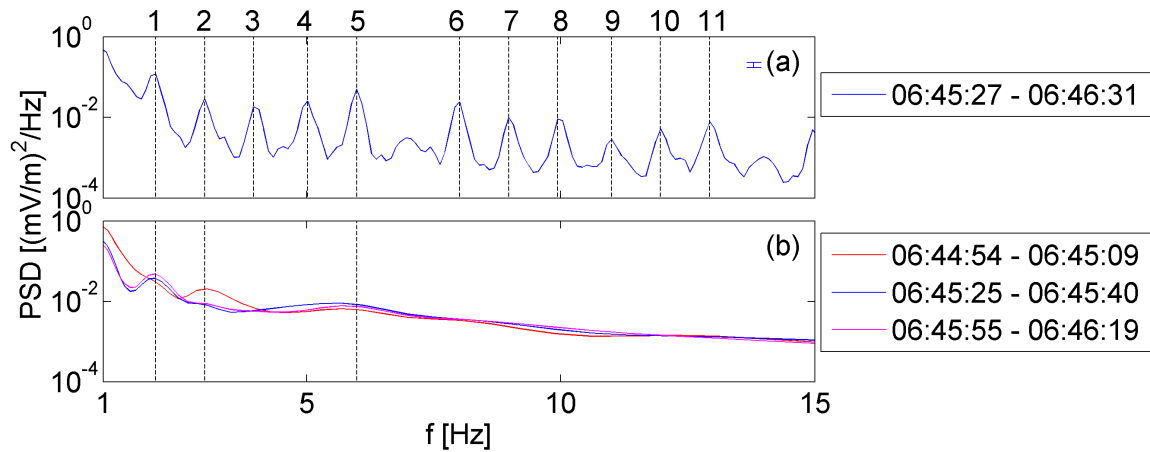


Figure 4.11. Averaged PSDs within the F16b cavity. (a) Averaged Fourier PSD computed from 11 sub-PSDs. (b) Morlet wavelet PSDs using only data in-between data gaps. The dashed vertical lines mark the peaks at frequencies given in Appendix F.

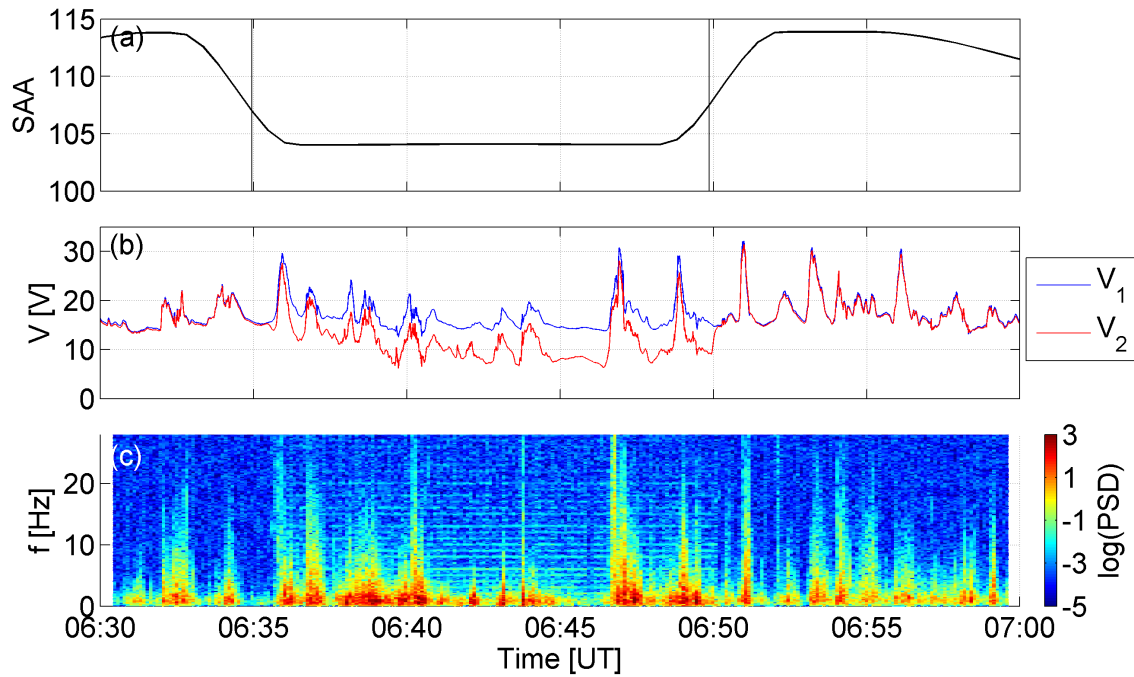


Figure 4.12. (a) The solar aspect angle (SAA), (b) uncalibrated probe potentials, and (c) Fourier spectrogram. The vertical lines mark the time when the solar aspect angle goes below 107° .

The vertical lines in Figure 4.11 mark the position of the spectral peaks. The peaks appear for roughly every 1 Hz throughout the investigated part of the spectrum, but only the peaks at highest power and lower frequencies in the Fourier PSD are detectable in the Morlet PSD, as well (see Appendix F). The fact that the peak frequencies are evenly spaced at almost every multiple of 1 Hz and decrease in power with increasing frequency, suggesting that the peaks might be harmonics of a fundamental 1 Hz-frequency wave.

A candidate for causing the horizontal lines is a change in the SAA, i.e., a change in the spacecraft orientation relative to the Sun's pointing vector, resulting in a change of illumination for the LAP2, as argued for in Section 4.1.4. Figure 4.12 shows the changing SAA, uncalibrated probe potentials and corresponding Fourier spectrogram for a 30 min time interval around the F16 cavity crossings. In the interval 06:35 - 06:50 UT the SAA goes below 107° , possibly causing a shadowing of LAP2. The decrease in the SAA and shadowing of LAP2 correlate well with the sudden appearance of the horizontal lines in the spectrogram. Similar horizontal lines are observed in the electric field spectrogram at other days when LAP2 is in shadow and LAP1 is sunlit (see Appendix F for a few examples of this in May 2016). This supports the claim that the horizontal lines are indeed related to the shadowing of LAP2.

The reason for the appearance of the horizontal lines when LAP2 is shaded and LAP1 is illuminated is still unknown. However, a discussion with Arne Pedersen (UiO, Oslo, Norway) led to the conclusion that a criteria for a well-functioning Langmuir probe in a space plasma is a high coupling to the plasma, and that it might be that the coupling of LAP2 to the plasma becomes poorer when the probe is shadowed, causing the appearance of the horizontal lines. This coupling is determined by the capacitance and resistance between the probe and plasma. The resistance $R = \Delta V / \Delta I$ is the limiting factor and must be smaller than $10^9 - 10^{10} \Omega$ (Arne Pedersen, UiO, Oslo, Norway, private communication).

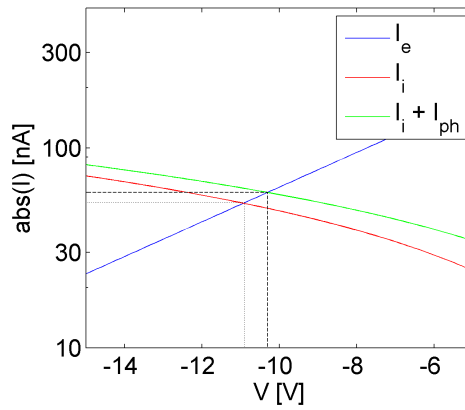


Figure 4.13. Modelled absolute values of electron current I_e , ion current I_i and sum of ion and photoemission currents $I_i + I_{ph}$ for plasma of density $n = 1000 \text{ cm}^{-3}$, electron energy 5 eV, ion speed $u = 700 \text{ m/s}$ and photoemission current $I_{ph} = 10 \text{ nA}$.

The potential difference ΔV and current ΔI of a floating probe is found when the sum of the electron current I_e , ion current I_i and photoemission current I_{ph} is zero. Figure 4.13 gives rough estimates of these values for both a sunlit probe with $I_{ph} = 10 \text{ nA}$ (dashed lines) and shadowed probe (dotted lines) in a plasma resembling the environment experienced by the Rosetta spacecraft during the F16 events. The shadowed probe has a slightly higher resistance than the sunlit one, but they are both on the order of $10^8 \Omega$, and are hence thought to be well-functioning. However, the preceding sections have shown that the experienced plasma environment is highly varying and does indeed differ from the one modelled in Figure 4.13. The difference in the coupling to the plasma between the sunlit and shadowed probes might therefore differ from the depicted one and by that be a candidate for causing the appearance of the horizontal lines. It is, however, not in the scope of this thesis to characterize these signatures, and therefore a further investigation of the coupling of the probes to the plasma, and its influence on the appearance of the horizontal lines is suggested for a later work. In the following the horizontal lines are considered noise in the characterization of the electric field signatures at the diamagnetic cavities.

4.2.1 Turbulent-like behaviour of the electric and magnetic fields

The individual PSDs that make up the electric and magnetic fields spectrograms of Figure 4.6 and 4.9 have a high uncertainty (see Section 3.3.1). To reduce the uncertainty of the PSDs, they are averaged over time-adjacent intervals with similar features. Figure 4.14 shows the averaged electric and magnetic fields PSDs before, during and after the M15 cavity crossing, and during and in-between the F16 cavities. In the averaged PSDs both before, during and after the M15 cavity, the wave signatures of the three magnetic field components are similar, apart from a generally higher power in the $B_2 \perp E$ component and the appearance of a reaction wheel-caused peak at 3.2 Hz in this component. Therefore, in Figure 4.14(c) and (d) the magnetic field components are displayed in the same colors for each interval, following the color-coding of the electric field PSDs. Recall that the time-persistent signature at 4.3 Hz is, as well as the 3.2 Hz peak in B_2 , caused by the spacecraft reaction wheels, and hence, they appear as noise in the averaged magnetic field PSDs. Therefore, only frequencies below 3 Hz are considered in the magnetic field spectra. As evident from the F16 magnetic field spectrograms of Figure 4.9, the reaction wheel signatures in the magnetic field vary significantly in the frequency range above 4 Hz during the observations on this day. Therefore, 4 Hz is set as the upper frequency limit of the averaged F16 magnetic field PSDs in Figure 4.14(f).

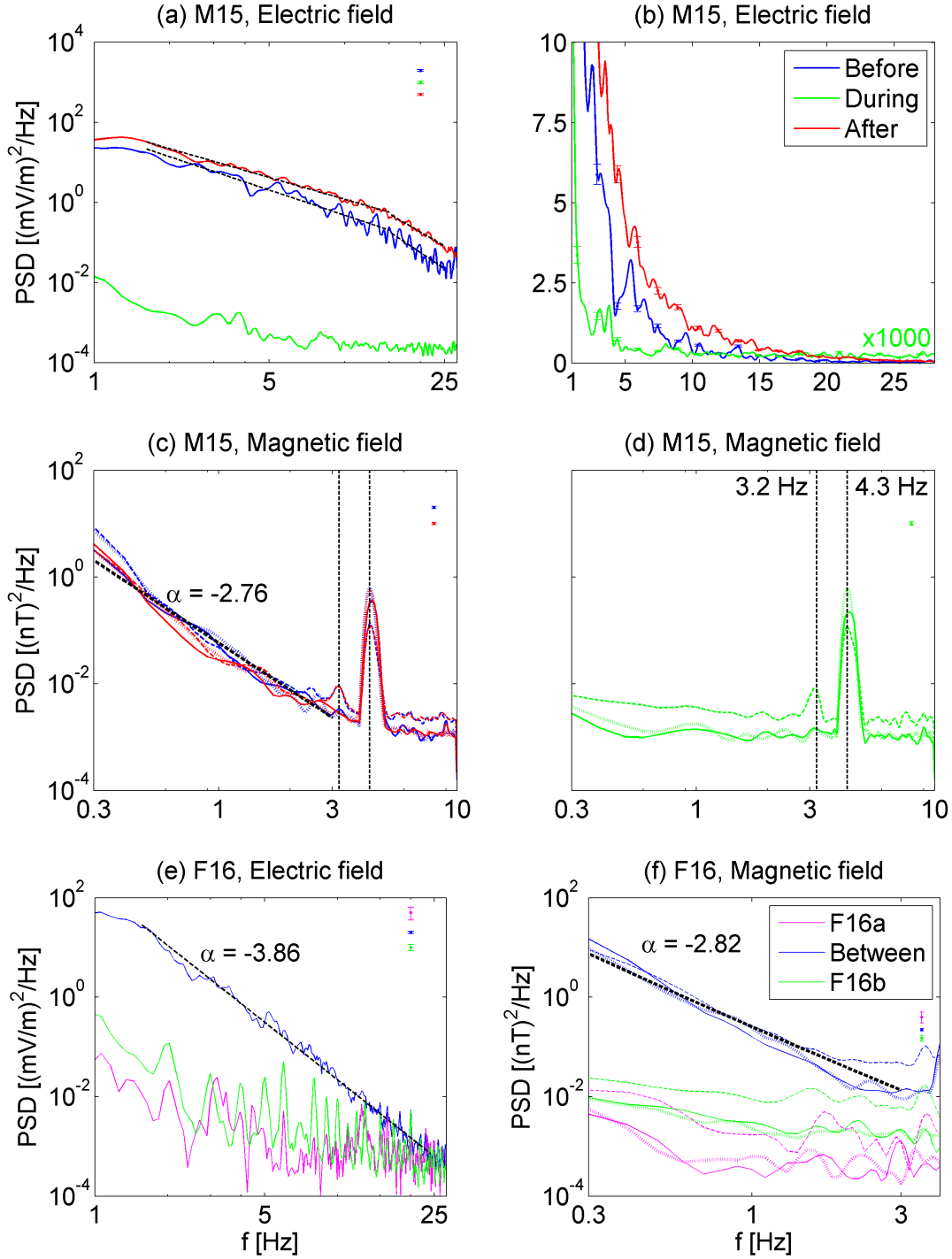


Figure 4.14. Averaged electric and three-component magnetic field PSDs before (21:40:00 - 21:47:00 UT), during (21:50:30 - 21:53:50 UT) and after (21:54:30 - 22:04:50 UT) the M15 cavity crossing and during and between (06:35:44 - 06:43:30 UT) the F16a (06:35:29 - 06:35:44 UT) and F16b (06:45:32 - 06:46:36 UT) cavities. (a)-(d) M15 electric and magnetic field PSDs using the same color coding. In (b) the PSD during the cavity is multiplied by 10^3 to increase visibility. (e)-(f) F16 electric and magnetic field PSDs during and between the cavities using same color coding. In the magnetic fields, the solid lines are $B_1 \parallel E$, the dashed lines are $B_2 \perp E$ and the dotted lines are $B_3 \perp E$. The dashed lines following the power-laws give the linear regressions of the PSDs with power-law coefficient α (for (a) the power-law coefficients are given in Table 4.6). In (c) and (d), the vertical dashed lines mark the power peaks at 3.2 and 4.3 Hz caused by the spacecraft reaction wheels. The errorbars are computed for the error $1/\sqrt{M}$ of a PSD averaged over M sub-PSDs.

Table 4.6. Power-law coefficients α_1 and α_2 for the averaged PSDs before and after the M15 cavity in the frequency intervals 1 – 15 Hz and 15 – 25 Hz, respectively. The first values in each cell give the slopes from the Fourier method, whilst the second values give the Morlet wavelet slopes.

	α_1 (1.5 – 15 Hz)				α_2 (15 – 25 Hz)			
	Fourier	R_F^2	Morlet	R_M^2	Fourier	R_F^2	Morlet	R_M^2
21:40:00 - 21:47:00	–2.09	0.8836	–1.91	0.9822	–4.18	0.6909	–3.78	0.9997
21:54:30 - 22:04:50	–1.81	0.9805	–1.74	0.9772	–3.65	0.9311	–3.45	0.9973

Figure 4.14(a) shows that outside the M15 cavity, electric field waves are excited throughout the entire frequency range with a slightly larger power after the cavity than before. The power in the magnetic field waves of Figure 4.14(c) do, however, not differ significantly from before to after the cavity. Inside the cavity both fields are at low powers, and for frequencies greater than the reaction wheel signatures, the power of the magnetic field waves outside of the cavity flattens to the values within the cavity. Between the F16 cavities, Figure 4.14(e) shows that waves throughout the frequency range are also present. Inside the F16 cavities the powers in the electric field PSDs are low, apart from the peak at roughly 12 Hz inside F16a that is also visible in the F16 electric field spectrograms of Figure 4.8. The noise is, however, rather large for the averaged F16a spectra due to the short duration of the cavity. Hence, no further analysis on this peak is carried out. The averaged magnetic field PSDs of the F16 events are at a constant low power within the cavities and show signatures of low-frequency waves in-between the cavities.

In both the electric and magnetic fields outside the M15 cavity and in the electric field between the F16 cavities, the power decreases with frequency in a cascade-like fashion that resembles the Kolmogorov turbulence cascade theory of Section 2.6.1. However, to quantitatively compare the power-laws of Figure 4.14 with the Kolmogorov theory, the PSDs must be first transformed into wavenumber space. To do so, several assumptions and simplifications on the spacecraft speed, sampling frequency, and wave propagation must be made (see e.g. Spicher (2013)). However, even without doing so, a few phenomenological remarks can be made on the features of the averages PSDs in frequency space.

The power-law relations for the magnetic and electric field PSDs are computed from least-squared fits of the frequency dependence of the PSD in double-logarithmic space. The fitted power-law relations show that the low-frequency magnetic field power decrease with a power-law coefficient of $\alpha = -2.76$ outside the M15 cavity and with $\alpha = -2.82$ between the F16 cavities. The related R-squared values vary between 0.5 – 0.97, and hence the difference between the coefficients is insignificant. In the study of low-frequency (< 1 Hz) magnetic fields fluctuations measured at comet 1P/H, 21P/G-Z, and 26P/G-S, Tsurutani et al. (1995) found that the magnetic field power fell off as $f^{-2.1}$, $f^{-1.9}$, and $f^{-1.9}$, respectively. They conclude that even though the magnetic field PSD at the three comets are similar in their power-laws coefficients, a more thorough study unravels that the observed plasma waves differ strongly from each other. Hence, similar power-laws of the magnetic field spectra during the M15 and F16 events of Figure 4.14(c) and (f) are not necessarily indicators that the wave behaviour in the plasma environments surrounding the M15 and F16 events is similar.

The fact that the waves in the plasma environments around the M15 and F16 cavities differ is evident from the low-frequency electric field PSDs of Figure 4.14(a) and (e). Between the F16 cavities, the power in the electric field decreases with a single power-law coefficient of $\alpha = -3.86$, whilst the electric field outside the M15 cavity shows dual-slope behaviour in both the Fourier and Morlet wavelet spectra. This

dual-slope power relation becomes steeper for frequencies above the break-point $f = 15\text{Hz}$. The M15 power-law coefficients in the intervals $1.5 - 15\text{Hz}$ and $15 - 25\text{Hz}$ for the interval before and after the cavity are presented in Table 4.6 along with their R-squared values.

Dual-slope electromagnetic power-laws have previously been observed in space plasmas. The break-point frequency at which the slope changes has for instance been related to the ion gyrofrequency. Spicher et al. (2014) find a power-law dual-slope relation in the density fluctuations in the Earth's ionosphere that steepens near the oxygen gyrofrequency, whilst Li et al. (2001) study the steepening of the magnetic field spectrum in the solar wind from a $f^{-5/3}$ to a f^{-3} relation at the local proton gyroradius. Bale et al. (2005) mention that the dual-slope relations exist since the plasma shows transfer range behaviour (see Figure 2.11) for frequencies below the ion gyrofrequency, but become demagnetised for higher frequencies, which causes a damping of the wave energy. However, the water-group ion gyrofrequency during the M15 event is on the order of $f_{ci} \approx 30\text{mHz}$, and is hence not linked to the observed break-point frequency near 15Hz .

High-frequency signatures

To investigate potential high-frequency features during the events, the averaged high-sampling frequency electric field PSDs for the M15 and F16b cavities are shown in Figure 4.15. The F16a cavity is excluded due to its short duration and the sampling of the high-frequency electric field signal. In each sampling period of 432 samples roughly every 32 s, the probe potentials are calibrated, and each resulting electric field time interval is Hanning-windowed and mean-detrended. No moving average is applied to the intervals, and hence the lowest frequency signatures must be interpreted with caution.

The high-frequency PSDs outside the cavities start at 43.5Hz with a power of $P = 10^{-3} - 10^{-1} (\text{mV/m})^2$ which roughly corresponds to the power at 28Hz in the low-frequency data. As in the low-frequency electric field PSDs, the power of the high-frequency sampling decreases with increasing frequency in a turbulence cascade-like fashion until a frequency of about 700Hz for the M15 event and 200Hz for the F16b event. These frequencies roughly correspond to the electron gyrofrequencies for the plasma environments surrounding the cavities (see Table 4.3). For higher frequencies, the PSDs flatten out and no clear peaks are detectable in the spectra.

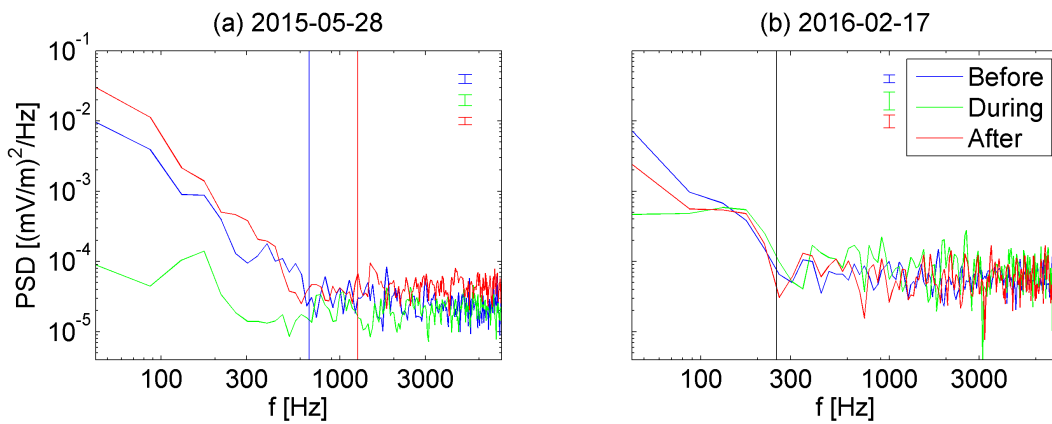


Figure 4.15. Averaged high-sampling frequency electric field PSDs before, during and after the (a) M15 and (b) F16b cavities. The vertical lines mark the electron gyrofrequencies estimated in Table 4.3, and the errorbars show the $1/\sqrt{M}$ error from averaging over M sub-PSDs.

In conclusion, the average electric and magnetic field PSDs of Figure 4.14 show that outside the cavity, the plasma waves follow a cascade-like behaviour. Outside the M15 cavity, the electric field spectra follow a dual-slope power-law that, in the present understanding, is interpreted as a possible change in unknown length scales. Figure 4.15 shows that the cascade-like behaviours of the electric fields outside of the cavities appear for frequencies below the local electron gyrofrequencies, and that for higher frequencies the power flattens out to the noise level. No distinguishable peaks are observed in the high-frequency range. The low-frequency electric field spectra, however, shows features below 10 Hz during the M15 event. Some of these features might also be present during the F16 events. However, due to the horizontal line-noise in the F16 spectra, these events are omitted for the subsequent sections that study time-localized low-frequency electric field wave signatures.

4.2.2 Low-frequency wave peaks

In addition to the cascade-like appearance, the M15 averaged electric field spectra of Figure 4.14(b) show signatures of low-frequency waves inside the cavity and possibly several low-frequency wave peaks in the environment surrounding the cavity. However, if the waves are not persistently present at the same frequency throughout the entire time intervals that the PSDs are averaged over, their signatures might be suppressed in the averaged PSDs. To investigate the nature of the spectral peaks observed in Figure 4.14(b), this section zooms in on specific time intervals outside of the cavity, where low-frequency wave signatures might be related to the LHF, in a similar fashion as done by Karlsson et al. (2017). This is followed by a discussion on the low-frequency wave signatures inside the M15 cavity itself.

Figure 4.16 shows individual PSDs of two 10 s sub-intervals before the M15 cavity (a)-(c) and a 6 s and 10 s sub-interval after the cavity (d)-(f). The intervals are chosen at times with a gradient in the potentials and over what visually looks like an electric field wave packet, using only the continuous signal between data gaps. For the considered time intervals, the probe potentials, local LHF computed from the cavity-calibrated magnetic fields, electric field estimates and corresponding PSDs are shown. Since the displayed PSDs are computed over just one time interval, their uncertainties are large. Hence, no definite conclusion about the existence of waves at the observed peak frequencies can be drawn. The PSDs, however, show features that might be related to the appearance of low-frequency waves within the cavity, which justifies the current analysis.

Before the cavity, the PSDs of Figure 4.16(c) show clear peaks at low frequencies. For the first time interval at 21:42:32 - 21:42:42 UT the PSD peaks at about 5.5 Hz. This correlates with a relatively constant LHF at 5 Hz and a gradient in the probe potentials, possibly related a change in electron density. The peak at about 3.5 Hz during the second interval at 21:42:42 - 21:42:52 UT also occurs in an interval with a probe potential gradient. During this interval, the LHF is roughly 4 Hz. Figure 4.16(f) shows that shortly after the cavity, the plasma is highly disturbed and several waves are excited in the frequency range below 6 Hz. Above this frequency, the wave power dies out apart from broad peaks at 8 – 9 Hz and 8 – 11 Hz in the intervals at 21:54:48 - 21:54:54 UT and 21:54:54-21:55:04 UT, respectively. These intervals are subject to changes in the probe potentials and a varying LHF in the range 8 – 10 Hz. If waves at the LHF are excited, the temporal change in the frequency might result in a broadening of the corresponding spectral peak, which might be what is observed in Figure 4.16(f).

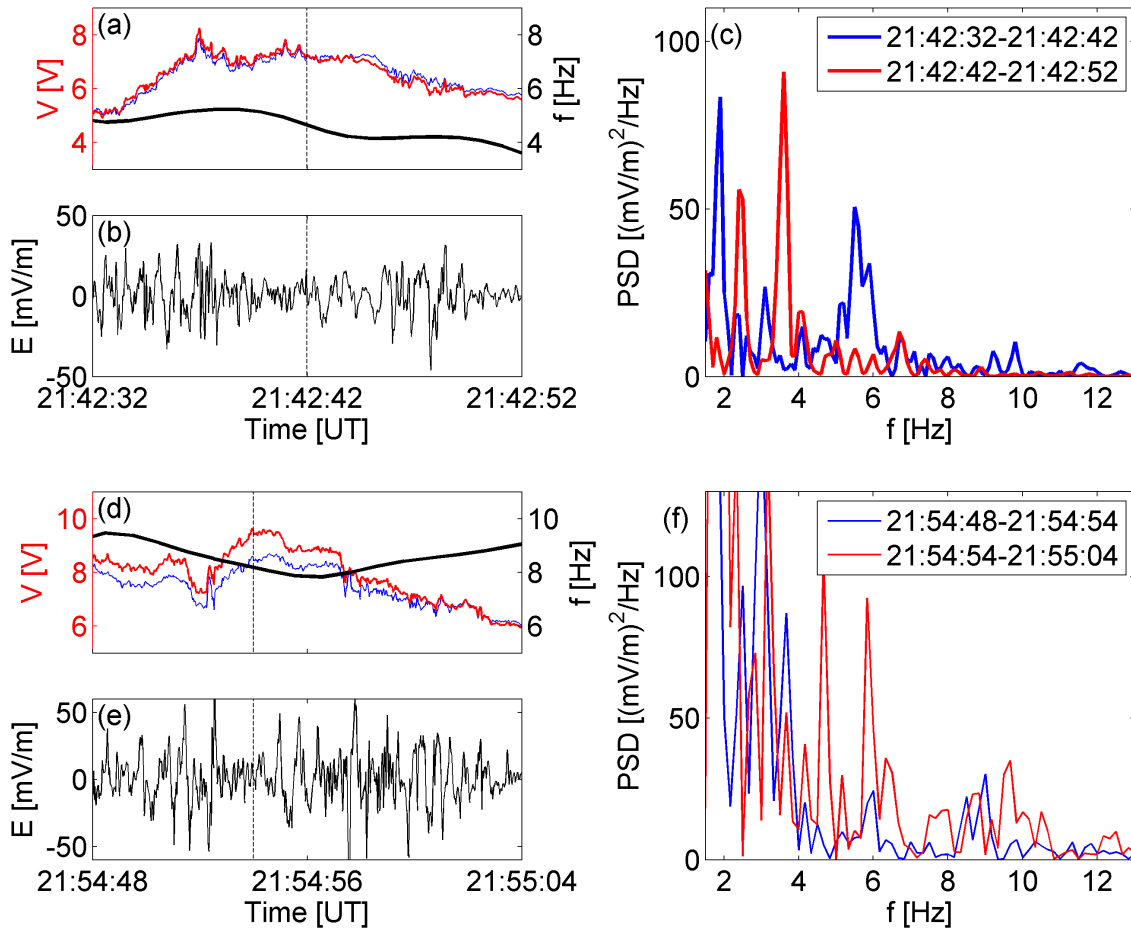


Figure 4.16. Zoom-ins on time intervals before (a)-(c) and after (d)-(f) the M15 cavity. (a),(d) Probe potentials and LHF, (b),(e) moving average-corrected electric field, (c),(f) Fourier PSDs computed over time intervals limited by the vertical dashed lines in (a), (b), (d) and (e). Inside the M15 cavity, the magnetic field magnitude has an averaged value of $\langle B \rangle = 1.67$ nT. The error of the computed LHF is assumed to be on the order of the corresponding LHF, i.e. 0.26 Hz.

The observed peak frequency matches the LHF in intervals where a density gradient is observed, suggesting that the peaks might be signatures of LH waves in the plasma outside the diamagnetic cavity. The detections of LH waves in cometary comae have earlier been ascribed to critical ionization velocity (CIV) events, where neutrals moving with a speed relative to a plasma are ionized (see Section 2.5.2). It is therefore possible that this mechanism may work near the diamagnetic cavity where the stagnant solar wind magnetic field separates the motion of the cometary plasma from the almost unaffected cometary neutrals. The criteria for the ionization is that the relative speed of the neutrals exceed the critical speed u_c determined by the ionization energy E_{ionize} and the kinetic energy of the neutrals of mass m , i.e.

$$u_c = \sqrt{\frac{2E_{ionize}}{m}}$$

A rough estimate of the critical speed yields $u_c \approx 12$ km/s for a water-molecule of ionization energy $E_{ionize} = 12.6$ eV and mass $m_{H_2O} = 18$ amu (NIST, May 25, 2017). Hence, in the simplified picture where cometary water neutrals travelling with a speed of the order of 1 km/s pass ions that are completely stagnant in the DCBL, the relative speed of the neutrals cannot alone cause a CIV effect.

However, since the LHF observations seem to be related to gradients in the electron density, it might be that the CIV mechanism does indeed work near the M15 cavity causing the LHF observations. Unfortunately, the observed peak frequencies additionally correspond to the reaction-wheel signatures in the magnetic field, and it cannot, in the present understanding, be excluded that the observed signatures are related to the spacecraft reaction wheels. However, the time-variability of the observed electric field signatures seems to indicate that these are not directly related to the persistent magnetic field reaction-wheel signatures easily detectable in the magnetic field spectra of Figure 4.7 and 4.14.

Low-frequency peaks within the cavity

Inside the M15 diamagnetic cavity the magnetic field magnitude is small (< 2 nT). Hence, the LHF is small within the cavity compared to outside. Even so, the Fourier and Morlet wavelet spectrograms of Figure 4.6 clearly show the existence of two time-localized low-frequency peaks at frequencies corresponding to the LHF both before and after the cavity are observed within the cavity itself (see e.g. Figure 4.6). These are also detectable, however, with dampened power, in the averaged Fourier PSD of Figure 4.14(b) within the cavity.

To investigate the nature of these peaks, Appendix E provides zoom-ins on the cavity and the time intervals where the peaks appear. The magnetic field measurements do not indicate that the peaks in the electric field spectra are related to changes in the magnetic field. Likewise, the probe potentials show that the peaks are not caused by any large change in the measured potentials. Hence, the electric field peaks are probably not related to a large increase in either the electron temperature or density. The electric field estimate, however, shows an increase in amplitude of the fluctuations when the 3 – 4 Hz peak reaches its greatest power around 21:52:15 UT. Zooming further in on the 3 – 4 Hz peak time intervals unravels that the increase in electric field fluctuation amplitude is related to a slight increased potential difference (i.e. $|V_2 - V_1|$) of the order of 0.1 V. As the difference in probe potentials decreases, so does the electric field amplitude and the peak power. In the 8 Hz peak, the maximum peak power at about 21:53:17 UT is, as well, related to an increase in the difference between the probe potentials (again see Appendix E for a zoom-in on this peak). However, the probe potential difference keeps increasing after the peak of greatest power in the PSDs. It is therefore concluded that the signatures are not purely caused by the increased potential difference.

To test the significance of the M15 low-frequency peaks, the electric field spectra are averaged over time intervals localized around the peaks. This is done in Figure 4.17 using both the Fourier and the Morlet wavelet methods. The sub-intervals for the Fourier method are subject to the same detrending and windowing degree as Figure 4.6(c), whilst the Morlet wavelet method uses a moving-average detrended signal. The time interval span of the 4 Hz peak is 21:51:50 - 21:52:40 UT, whereas the 8 Hz peak appears between 21:53:10 and 21:53:35 UT. From the estimated error ($1/\sqrt{M}$ for M sub-intervals) both peaks are significant, and it is clear that during the first interval, no signature of the 8 Hz peak is present, whilst during the second interval, the clear signature of the 4 Hz peak disappear.

In the diamagnetic cavities of comet 67P, high-frequency waves in the water-group ion acoustic wave range (Gunell et al., 2017) have been observed, and in regions with increased ion densities, as would be expected to exist in the ion pile-up region in the DCBL, waves in the LHF range have been observed during cometary missions (see e.g. Savin et al. (1986), and Karlsson et al. (2017)). However, low-frequency peaks similar to those depicted in Figure 4.17 have, to the author's knowledge, never been observed within the

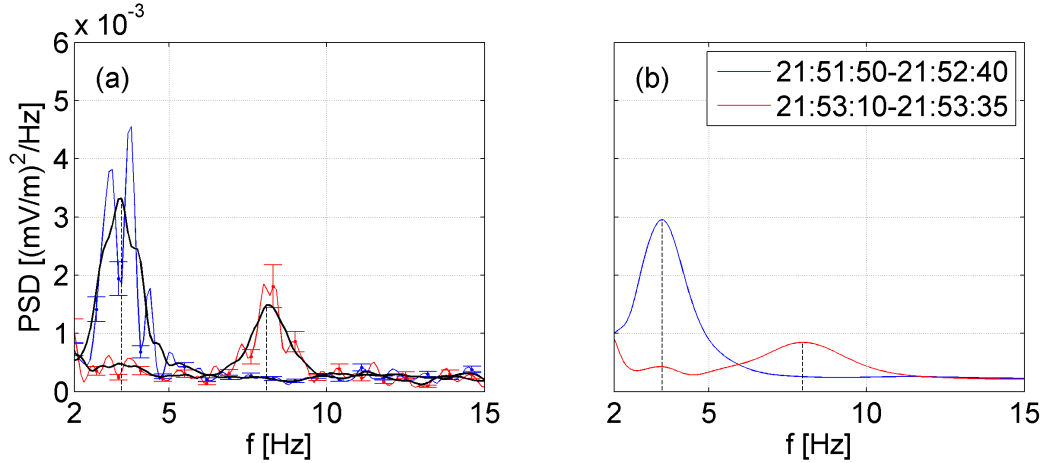


Figure 4.17. Averaged electric field PSDs computed with the (a) Fourier method and (b) Morlet wavelet method, during two time intervals with low-frequency peaks inside the M15 cavity. Note that the y-axis and color coding are the same for both plots.

cometary diamagnetic cavity itself. Moreover, other RPC-instruments were not able to pick up signals in the same range either due to the temporal resolution, bandwidth or amount of available data during the event. A full analysis of the nature of the power intensifications cannot be carried out with only one event and no supporting instruments. However, a few suggestions as to the origin of the wave signatures will be discussed in the following, noting first that the candidates for causing the signatures are the methods, the spacecraft and its instruments, or a plasma physical phenomena at the DCBL and cavity regions.

Method-caused

As seen by the effect of signal data gaps, trends and discontinuous sub-interval edges, the method can introduce un-physical signatures in the analysis. To test whether this is the case for the M15 low-frequency cavity peaks, the power and peak frequency of the Fourier and Morlet wavelet methods are compared in this section.

To evaluate the power P of each peak, the PSDs are summed over frequency (see Eq. (3.36)) and corrected by subtracting the background power. The background PSD is computed as the average in the frequency range 10 – 15 Hz of the PSDs in Figure 4.17(a) and the 21:51:50 - 21:52:40 UT PSD in Figure 4.17(b). From this it is found that averaged background PSD is $PSD_{BG} = 0.268 \times 10^{-3} \text{ (mV/m)}^2/\text{Hz}$. Hence, the total power of the background signal from 2 – 15 Hz is $P_{BG} = PSD_{BG} \times 14 \text{ (mV/m)}^2$. The power of the peaks are computed for both the Fourier and Morlet wavelet spectra that are interpolated on a grid from 2 – 15 Hz with a frequency-resolution of 0.1 Hz. This is done to simplify the computation of the power in the Morlet wavelet spectra which has a non-evenly spaced frequency resolution. The power in each peak is then computed as

$$P = \frac{1}{10} \sum_{i=1}^N PSD_i - P_{BG} \quad (4.4)$$

where i runs over N frequency steps between 2 and 15 Hz. The fraction in front of the sum corrects for the fact that the frequency resolution is 0.1 Hz. The resultant powers in the two low-frequency peaks are shown in Table 4.7 along with the peak frequencies for both methods.

The averaged Fourier and Morlet wavelet electric field PSDs identifies the peaks at the same frequencies with roughly the same powers in each wave. The fact that the wave powers picked up by the methods

Table 4.7. Frequency and power of peaks seen in the averaged Fourier and Morlet wavelet PSDs of Figure 4.17 inside the M15 cavity.

Time [UT]	f_F [Hz]	P_F [(mV/m) ²]	f_M [Hz]	P_M [(mV/m) ²]
21:25:50 - 21:52:40	3.5	4.29×10^{-3}	3.5	5.01×10^{-3}
21:53:10 - 21:53:35	8.1	1.75×10^{-3}	8.0	1.84×10^{-3}

vary slightly is attributed to the frequency resolutions and accuracy of the methods. Additionally, filtering out the data gaps in the electric field mode shows similar results as in Figure 4.17. That the peaks are identified up by both the Fourier method and the Morlet wavelet method, and that the presence of data gaps does not seem to influence the results suggest that the observed features have physical origins and are not caused by the methods.

Spacecraft- and instrument-caused

On the spacecraft, the reaction wheels disturb the magnetic field estimates for frequencies above 3 Hz by causing persistent magnetic field wave signatures at 3.2 and 4.3 Hz during the M15 event (see Figure 4.9 and Figure 4.14(c)-(d)). A magnetic field disturbance in a plasma is likely to affect the electric field. However, the reaction wheel signatures are nearly constant in frequency throughout the entire M15 event, and no apparent change in the magnetic field spectra is related to the sudden appearance of the low-frequency electric field waves. It is therefore considered unlikely that the features observed within the M15 cavity are directly related to the reaction wheel signatures observed in the magnetic field.

Other error and disturbance sources on the spacecraft and its instrumentations might be held accountable for the cavity waves. As seen for the F16 events, the change in SAA that results in shadowing of LAP2 correlates with the appearance of harmonics in the low-frequency electric field. During the M15 cavity crossing, the SAA is, however, rather constant at roughly 114° throughout the event. This corresponds to both probes being illuminated, and no signs of the low-frequency harmonics are seen during this event.

Physical origin

The individual electric field PSDs before and after the M15 cavity of Figure 4.16 show that the observed cavity peaks are in the LHF range outside of the cavity. Without a mathematical argument, it is here suggested that the features seen within the cavity might be related to LH waves generated in the plasma outside the cavity. This signature is then thought to either propagate through or modulate the boundary at the LHF, which then might compress ion content within the diamagnetic cavity, causing waves at similar frequencies within the magnetic field-free cavity as in the surrounding environment. To test this hypothesis, it is suggested for a future theoretical and simulation study to demonstrate whether such a mechanism might be held accountable for the observed features inside the cavity.

4.3 Summary of the cavity signatures

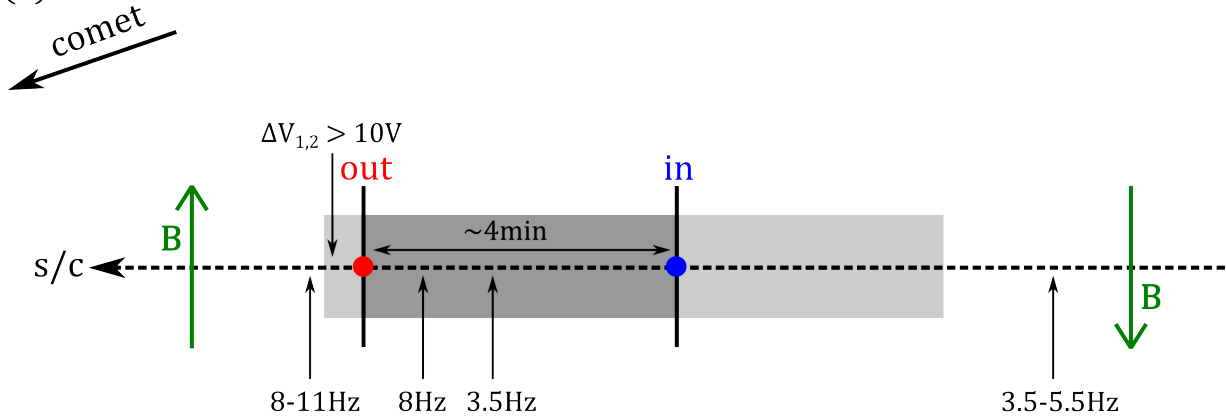
The studied cavities show some similar electric probe and field signatures albeit observed at times with different surrounding plasma environments. This is illustrated in Figure 4.18 that schematically summarizes the findings of this chapter. The cavity length scales and time locations observed in the electric fields are similar to those in the magnetic fields with long inbound and short outbound DCBLs

surrounding rather quiet cavities. An MVA and subsequent study of the mean magnetic field directions unravel that the M15 cavity exhibits signs of magnetic field draping, whilst the magnetic field seems to be deflected around the F16 cavities.

The F16 inbound DCBLs are subject to a probe potential increase of the order of 5 V, whilst all outbound boundaries are related to a sharp potential increase of more than 10 V. For the F16 events a comparison between the LAP potentials and MIP electron densities demonstrates that the potential increases at the inbound DCBLs are caused by increases in electron densities, whilst the outbound boundaries show signs of both electron density increases and heating.

Several wave signatures are observed close to and inside the M15 cavity. These are all in the LHF range outside the cavity, and the cavity signatures are suggested to be the result of modulation of waves generated in the surrounding plasma environment into the cavity. Wave signatures are not studied for the F16 events, even though a short signature at a frequency of roughly 12 Hz appears inside the F16a cavity. This is omitted due to the duration of the events and to the fact that the cavities are observed during a time interval where the electric field signal is disturbed by possibly harmonics of a 1 Hz source.

(a) M15



(b) F16

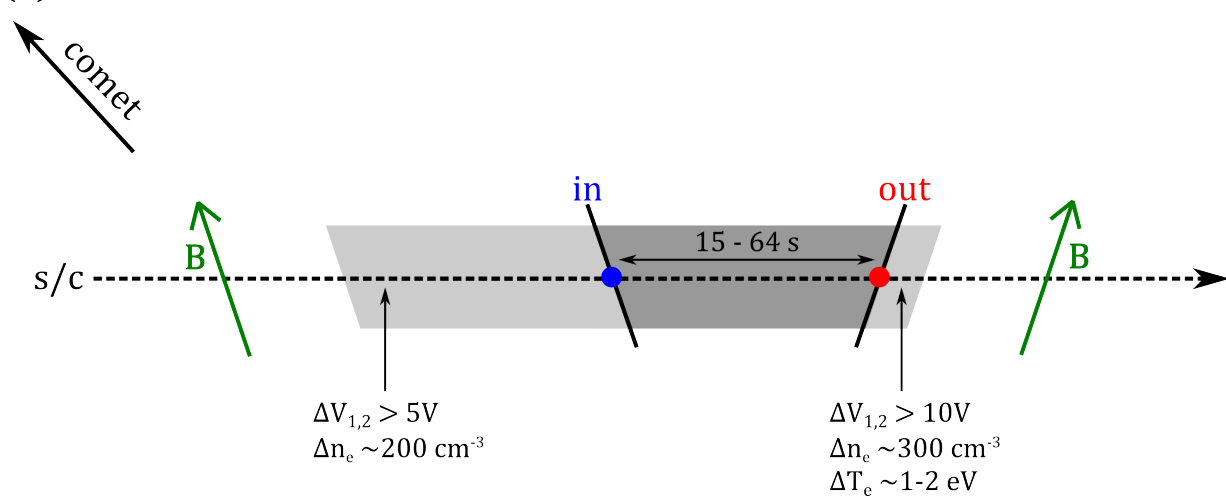


Figure 4.18. Schematic illustration of the findings for the M15 (a) and F16 (b) cavities. The F16 cavities show similar features and are therefore included in the same sketch.

CONCLUSION AND PERSPECTIVES

The diamagnetic cavity is the innermost region of the cometary plasma environment. It is characterized by an exclusion of the solar wind magnetic field that is stagnating upstream of the cavity boundary, called the contact surface. The contact surface stand-off distance is, in the current understanding, determined by a pressure balance between the solar wind magnetic field and cometary ion-neutral friction (Cravens, 1986), but instabilities triggered by, e.g., asymmetric comet outgassing and velocity shears at the boundary might cause a greatly varying cometocentric distance of the boundary (Goetz et al., 2016a). The diamagnetic cavity boundary layer (DCBL) is the region in which the magnetic field magnitude gradually decreases. It is both theoretically explained (Israelevich et al., 2003) and experimentally observed (Goetz et al., 2016b) that a boundary current exists within the DCBL, and that it might close within the cavity itself (Gunell et al., 2017).

During the Giotto flyby of comet 1P/Halley, a global diamagnetic cavity was observed at a stand-off distance of 4600 km (Cravens and Gombosi, 2004). The Rosetta mission to comet 67P/ChuryumovGerasimenko (67P) additionally provides observations of more than 600 cavity crossings with durations of 8 s – 40 min (Goetz et al., 2016b). These might be small-scale local structures on the global cavity, and, in the magnetic field measurements, they typically show magnetic field draping, a long inbound DCBL on the order of the cavity, and an abrupt outbound boundary layer.

In this work, the study of the electric field fluctuations during three of the observed diamagnetic cavities near comet 67P on May 28, 2015, (M15) and February 17, 2016, (F16) have shown that the electric field fluctuation level estimated from the Langmuir probes (LAP) of the Rosetta Plasma Consortium (RPC) qualitatively follows the behaviour of that of the magnetic field measurements by the RPC magnetometer (MAG), by picking up roughly the same temporal scales for the cavity and its DCBLs as picked up by the MAG instrument. The temporal location of the cavity and its boundary layers defined by the LAP instrument, however, vary slightly from those defined by MAG. This is attributed to the spatial positions of the instruments and the fact that LAP only estimates the electric field in one dimension, whilst MAG gives the three-dimensional magnetic field components and hence a more precise definition of the boundary locations.

During the F16 event, the spectra of the electric field fluctuations, estimated from the difference in the LAP probe potentials, are disturbed by peaks at every frequency step of 1 Hz. The nature of these features is still not understood, but they seem to be related to the change in the solar aspect angle (SAA) for

$SAA < 107^\circ$ that causes full or partial shadowing of LAP2. The shadowing of LAP2 is suggested to result in a poorer coupling to the plasma. This, however, has to be studied in detail for other events where such features appear.

In the LAP electric field mode, the probe potentials show weak increases at the beginning of the inbound DCBLs and more drastic increases at the outbound transitions. Since the probe potentials give an estimate of the negative of the spacecraft potential that is dependent on the electron density and temperature, the fluctuations in the probe potentials might be related to electron density or temperature variations, or both. For the F16 events the LAP potential increases are indeed shown to correspond to increases in the electron density estimated by the MIP instrument. This might be the case for the M15 event, as well, but cannot be tested due to unavailability of MIP data on this date. The comparative study between the MIP electron density and LAP probe potentials during the F16 events, additionally shows that the sharp outbound boundaries might be related to electron temperature increases of the order of $1 - 2\text{ eV}$. The RPC ion composition analyser (ICA) observations suggest that the increase in electron temperature might be related to an ion bulk velocity increase, as well, but that this increase might be caused by an increase in the magnitude of the spacecraft potential. However, the time resolution of the ICA instrument is on the order of the cavity, and is hence too poor for a detailed ICA study during the considered events.

Inspired by the temperature profile estimated from the study between LAP and MIP during the F16 events, it is suggested as a further work to comparatively study the MIP electron densities with the single-probe floating-bias or bias-sweep modes of the LAP instrument during other diamagnetic cavity events. Such studies might conclude whether the increase in the absolute value of the spacecraft potential at the outbound DCBL is a persistent feature of the observed cavities at comet 67P, and whether it is related to both electron density increases and heating.

Inside the M15 cavity unexpected time-localized low-frequency peaks occur at 3.5 Hz and 8 Hz for time intervals of 50 s and 25 s, respectively. These are visible in both the Fourier and Morlet wavelet spectrograms, indicating that they might not be caused by the analysis method. Candidates for generating these are the spacecraft reaction wheels that are easily detected in the spectrograms of the three magnetic field components. It is argued that the cavity waves are unlikely to be caused by this source, since the low-frequency cavity waves are short transient events with different characteristic frequencies, whilst no variation in the reaction wheel-interference was detected. Instead it is suggested that the low-frequency cavity peaks might be related to waves that are observed at similar frequencies in the lower hybrid frequency (LHF) range in the plasma environment surrounding the cavity. However, no modelling approach to study this hypothesis is carried out in this work, and it is left for a later study to investigate whether a mechanism propagating the LH waves into the cavity is physically possible.

Due to a small number of cavity crossings at comet 67P coinciding with the LAP instrument in electric field mode, it is not possible to make statistical studies of the electric field behaviour inside the diamagnetic cavities. However, an additional cavity at about 21:10:15 - 21:10:50 UT on May 28, 2015, was recently discovered by inspection of the LAP electric field mode, supporting that the electric field and probe potential features are characteristic for cavity crossings at comet 67P. The MAG team has confirmed that this new event does indeed show the magnetic field characteristics of cavities crossed by the Rosetta spacecraft and will add this event to the already extensive list of cavity crossings. In the electric field, this cavity, in addition, seems to show transient wave signatures at low-frequencies. A full analysis of the electric field spectra, therefore, has to be carried out to study whether the nature and origin of the M15

signatures might be linked to the features in the newly discovered cavity.

In addition, experimental studies of the cavity observations of low-frequency electric field waves near the water-group ion LHF range in the surrounding medium might be reproduced by an AMPTE gas release-like mission in near-Earth space. It is suggested that one spacecraft (s/c1) of a dual-spacecraft mission releases a sufficient amount of water-group neutrals into the solar wind at a heliocentric distance of about 1 AU. The second spacecraft (s/c2) is stationary relative to s/c1 and located upstream of the gas-release. As the water-group neutrals are ionized and interact with the solar wind, a diamagnetic cavity is expected to be formed. Upstream of the gas-release, s/c2 measures the three-component magnetic field and Langmuir probe-estimated electric field as the cavity boundaries cross over the spacecraft. This, in addition to simulations and theoretical work, will add information about the nature of waves near the boundary regions of diamagnetic cavities and hence provide insight into the possible behaviour of the translation of waves generated in a magnetized plasma into an unmagnetized plasma.

This study has, hence, provided new information on the electric fingerprints of cometary diamagnetic cavities at comet 67P and has, in addition to supporting findings by other RPC instruments, provided detection of priorly unobserved electric field waves within the cavity. The nature and origin of these might be explained by suggested future studies.



BIBLIOGRAPHY

- Alfvén, H. *Existence of electromagnetic-hydrodynamic waves*. Nature, 150, 405–406, 1942.
- Alfvén, H. *On the theory of comet tails*. Tellus, 9, 1957.
- Alfvén, H. *Collision between a Nonionized Gas and a Magnetized Plasma*. Reviews of Modern Physics, 32, 710–713, 1960.
- Alfvén, Hannes. *On the origin of the solar system*. The international series of monographs on physics. Oxford University Press, 1954.
- Bale, S. D., Kellogg, P. J., Mozer, F. S., Horbury, T. S., and Reme, H. *Measurement of the Electric Fluctuation Spectrum of Magnetohydrodynamic Turbulence*. Physical Review Letters, 94(21), 2005.
- Balsiger, H., Altwegg, K., Buhler, F., Geiss, J., Ghielmetti, A. G., Goldstein, B. E., Goldstein, R., Huntress, W. T., Ip, W.-H., Lazarus, A. J., Meier, A., Neugebauer, M., Rettenmund, U., Rosenbauer, H., Schwenn, R., Sharp, R. D., Shelly, E. G., Ungstrup, E., and Young, D. T. *Ion composition and dynamics at comet Halley*. Nature, 321, 330–334, 1986.
- Balsiger, H., Altwegg, K., Arijis, E., Bertaux, J.-L., Berthelier, J.-J., Bochslers, P., Carignan, G. R., Eberhardt, P., Fisk, L. A., Fuselier, S. A., Ghielmetti, A. G., Gliem, F., Gombosi, T. I., Kopp, E., Korth, A., Livi, S., Mazelle, C., Rème, H., Sauvaud, J. A., Shelley, E. G., Waite, J. H., Wilken, B., Woch, J., Wollnik, H., Wurz, P., and Young, D. T. *Rosetta orbiter spectrometer for ion and neutral analysis-rosina*. Advances in Space Research, 21, 1527–1535, 1998.
- Markus Bauer, *Rosetta arrives at comet destination*, 2014. http://www.esa.int/Our_Activities/Space_Science/Rosetta/Rosetta_arrives_at_comet_destination. Accessed: March 13, 2017.
- Baumjohann, Wolfgang and Treumann, Rudolf A. *Basic Space Plasma Physics*. Imperial College Press, London, 1996.
- Behar, E., Lindkvist, J., Nilsson, H., Holmström, M., Stenberg-Wieser, G., Ramstad, R., and Götz, C. *Mass-loading of the solar wind at 67P/Churyumov-Gerasimenko. Observations and modelling*. Astronomy and Astrophysics, 596, A42, 2016.

- Biermann, L., Brosowski, B., and Schmidt, H. U. *The interactions of the solar wind with a comet*. Solar Physics, 1, 254–284, 1967.
- Bingham, R., Shapiro, V. D., Gil’Man, M., Tsytovich, V. N., and de Angelis, U. *Theory of wave activity occurring in the AMPTE artificial comet*. Physics of Fluids B, 3, 1728–1738, 1991.
- Bittencourt, J. A. *Fundamentals of Plasma Physics*. Springer, 2004.
- Blandford, Roger D. and Thorne, Kip S. *Applications of classical physics*. Caltech, Pasadena, 2013.
- Boyd, T. J. M. and Sanderson, J. J. *The Physics of Plasma*. ISBN: 0-521-45290-2. Cambridge University Press, 2003.
- Brenning, N. *Review of the CIV phenomenon*. Space Science Reviews, 59, 209–314, 1992.
- Burch, J. L., Goldstein, R., Cravens, T. E., Gibson, W. C., Lundin, R. N., Pollock, C. J., Winningham, J. D., and Young, D. T. *RPC-IES: The ion and electron sensor of the Rosetta Plasma Consortium*. Space Science Reviews, 128, 697–712, 2006.
- Carbone, V. and Pouquet, A. An Introduction to Fluid and MHD Turbulence for Astrophysical Flows: Theory, Observational and Numerical Data, and Modelling. In Loukas Vlahos and Peter Cargill, editor, *Turbulence in Space Plasmas, Lect. Notes Phys.* 778, pages 71–128. 2009.
- Carr, C., Cupido, E., Lee, C. G. Y., Balogh, A., Beek, T., Burch, J. L., Dunford, C. N., Eriksson, A. I., Gill, R., Glassmeier, K. H., Goldstein, R., Lagoutte, D., Lundin, R., Lundin, K., Lybekk, B., Michau, J. L., Musmann, G., Nilsson, H., Pollock, C., Richter, I., and Trotignon, J. G. *RPC: The Rosetta Plasma Consortium*. Space Science Reviews, 128, 629–647, 2007.
- Chen, Francis F. Electric Probes. In Richard H. Huddleston and Stanley L. Leonard, editor, *Plasma Diagnostic Techniques*, chapter 4, pages 113–200. 1965.
- Chun-Lin, Liu. *A Tutorial of the Wavelet Transform*, February 2010.
- Coates, A. J. *Ionospheres and magnetospheres of comets*. Advances in Space Research, 20, 255, 1997.
- Coates, A. J. and Jones, G. H. *Plasma environment of Jupiter family comets*. Planetary Space Science, 57, 1175–1191, 2009.
- Coates, A J, Burch, J L, Goldstein, R, Nilsson, H, Wieser, G Stenberg, Behar, E, and RPC team,. *Ion pickup observed at comet 67P with the Rosetta Plasma Consortium (RPC) particle sensors: similarities with previous observations and AMPTE releases, and effects of increasing activity*. Journal of Physics: Conference Series, 642(1), 012005, 2015.
- Cravens, T. E. The physics of the cometary contact surface. In B. Battick, E. J. Rolfe, and R. Reinhard, editors, *ESLAB Symposium on the Exploration of Halley’s Comet*, volume 250 of *ESA Special Publication*, December 1986.
- Cravens, T. E. *Theory and observations of cometary ionospheres*. Advances Space Research, 7, 147–158, 1987.
- Cravens, T. E. *Cometary plasma boundaries*. Advances in Space Research, 9, 293–304, 1989.

- Cravens, T. E. *A magnetohydrodynamical model of the inner coma of Comet Halley*. Journal of Geophysics Research, 94, 15025–15040, 1989.
- Cravens, T. E. and Gombosi, T. I. *Cometary magnetospheres: a tutorial*. Advances in Space Research, 33, 1968–1976, 2004.
- Crovisier, J. *Photodestruction rates for cometary parent molecules*. Journal of Geophysics Research, 99, 3777–3781, 1994.
- Davidson, P. A. *An Introduction to Magnetohydrodynamics*. Cambridge University Press, 2001.
- Deca, Jan, Divin, Andrey, Henri, Pierre, Eriksson, Anders, Markidis, Stefano, Olshevsky, Vyacheslav, and Horányi, Mihály. *Electron and Ion Dynamics of the Solar Wind Interaction with a Weakly Outgassing Comet*. Phys. Rev. Lett., 118, 205101, 2017.
- Dickeli, Guillaume. Statistical analysis of the electric field measurements from the Rosetta spacecraft in the plasma environment of comet 67P/Churyumov-Gerasimenko. Master thesis, KTH Royal Institute of Technology, Department of Space and Plasma Physics, Stockholm, Sweden, Dec 2016.
- Edberg, N. J. T., Eriksson, A. I., Odelstad, E., Henri, P., Lebreton, J.-P., Gasc, S., Rubin, M., André, M., Gill, R., Johansson, E. P. G., Johansson, F., Vigren, E., Wahlund, J. E., Carr, C. M., Cupido, E., Glassmeier, K.-H., Goldstein, R., Koenders, C., Mandt, K., Nemeth, Z., Nilsson, H., Richter, I., Wieser, G. S., Szego, K., and Volwerk, M. *Spatial distribution of low-energy plasma around comet 67P/CG from Rosetta measurements*. Geophysics Research Letters, 42, 4263–4269, 2015.
- Eriksson, A. I., Boström, R., Gill, R., Åhlén, L., Jansson, S.-E., Wahlund, J.-E., André, M., Mälkki, A., Holtet, J. A., Lybekk, B., Pedersen, A., and Blomberg, L. G. *RPC-LAP: The Rosetta Langmuir Probe Instrument*. Space Science Reviews, 128, 729–744, 2007.
- Eriksson, A. I., Hanberg, C., and Sjogren, A. Modelling of spacecraft potential measurements on Rosetta. 11th Spacecraft Charging Technology Conference (SCTC-11), Albuquerque, USA, NASA, 2010.
- Eriksson, A. I., Engelhardt, I. A. D., André, M., Beström, R., Edberg, N. J. T., Johansson, F. L., Odelstad, E., Vigren, E., Wahlund, J.-E., Henri, P., Lebreton, J.-P., Miloch, W. J., Paulsson, J. J. P., Simon Wedlund, C., Yang, L., Karlsson, T., Broiles, T., Mandt, K., Carr, C. M., Galand, M., Nilsson, H., and Norberg, C. *Cold electrons at comet 67P*. Astronomy & Astrophysics, 2017.
- Eriksson, Anders I. Spectral Analysis. In Götz Paschmann and Patrick W. Daly, editor, *Analysis Methods for Multi-Spacecraft data*, pages 5–42. 2000.
- ESA:flickr, *European Space Agency's flickr, Galerie de ESA Espace. Mission Rosetta*. <https://www.flickr.com/photos/europeanspaceagency/11206647984/in/photostream/>. Accessed: March 11, 2017.
- Farge, M. *Wavelet transforms and their applications to turbulence*. Annual Review of Fluid Mechanics, 24, 395–457, 1992.
- Formisano, V., Galeev, A. A., and Sagdeev, R. Z. *The role of the critical ionization velocity phenomena in the production of inner coma cometary plasma*. Planetary and Space Science, 13, 1982.
- Uriel Frisch, editor. *Turbulence: The Legacy of A. N. Kolmogorov*. Cambridge University Press, 1995.

- Fuselier, S. A., Shelley, E. G., Balsiger, H., Geiss, J., Goldstein, B. E., Goldstein, R., and Ip, W.-H. *Cometary H^{2+} and solar wind He^{2+} dynamics across the Halley cometopause*. Geophysics Research Letters, 15, 549–552, 1988.
- Galand, M., Héritier, K. L., Odelstad, E., Henri, P., Broiles, T. W., Allen, A. J., Altwegg, K., Beth, A., Burch, J. L., Carr, C. M., Cupido, E., Eriksson, A. I., Glassmeier, K.-H., Johansson, F. L., Lebreton, J.-P., Mandt, K. E., Nilsson, H., Richter, I., Rubin, M., Sagnières, L. B. M., Schwartz, S. J., Sémon, T., Tzou, C.-Y., Vallières, X., Vigren, E., and Wurz, P. *Ionospheric plasma of comet 67P probed by Rosetta at 3 au from the Sun*. Monthly Notices of the RAS, 462, S331–S351, 2016.
- Galeev, A. A. *Spectra of plasma turbulence, particle acceleration and heating by plasma waves in the interacting plasma*. American Geophysical Union Geophysical Monograph Series, 53, 1–12, 1989.
- Galeev, A. A., Gribov, B. E., Gombosi, T., Gringauz, K. I., Klimov, S. I., Oberz, P., Remizov, A. P., Riedler, W., Sagdeev, R. Z., Savin, S. P., Sokolov, A. Yu., Shapiro, V. D., Shevchenko, V. I., Szego, K., Verigin, M. I., and Yeroshenko, Ye. G. *Position and structure of the comet Halley bow shock: Vega-1 and Vega-2 measurements*. Geophysical Research Letters, 13(8), 1986.
- Galeev, A. A., Gringauz, K. I., Klimov, S. I., Remizov, A. P., and Sagdeev, R. Z. *Critical ionization velocity effects in the inner coma of Comet Halley - Measurements by Vega-2*. Geophysics Research Letters, 13, 845–848, 1986.
- Galeev, A. A., Gringauz, K. I., Klimov, S. I., Remizov, A. P., Sagdeev, R. Z., Savin, S. P., Sokolov, A. Y., Verigin, M. I., Szegö, K., Tátrallyay, M., Grard, R., Yeroshenko, Y. G., Mogilevsky, M., Riedler, W., and Schwingenschuh, K. *Physical processes in the vicinity of the cometopause interpreted on the basis of plasma, magnetic field, and plasma wave data measured on board the Vega 2 spacecraft*. Journal of Geophysics Research, 93, 7527–7531, 1988.
- Gibney, E. *Mission accomplished: Rosetta crashes into comet*. Nature, 538, 13–14, 2016.
- Glassmeier, K.-H. and Neubauer, F. M. *Low-frequency electromagnetic plasma waves at comet P/Grigg-Skjellerup: Overview and spectral characteristics*. Journal of Geophysics Research, 98, 20, 1993.
- Glassmeier, Karl-Heinz. *Interaction of the solar wind with comets: a Rosetta perspective*. Philosophical Transactions of the Royal Society of London A: Mathematical, Physical and Engineering Sciences, 375 (2097), 2017.
- Glassmeier, Karl-Heinz, Tsurutani, Bruce T., and Neubauer, Fritz M. *Adventures in parameter space: a comparison of low-frequency plasma waves at comets*. In T. Hada and H. Matsumoto, editor, *Nonlinear Waves and Chaos in Space Plasmas*, 1997.
- Glassmeier, Karl-Heinz, Richter, Ingo, Diedrich, Andrea, Musmann, Gü., Auster, Uli, Motschmann, Uwe, Balogh, Andre, Carr, Chris, Cupido, Emanuele, Coates, Andrew, Rother, Martin, Schwingenschuh, Konrad, Szegö, Karoly, and Tsurutani, Bruce. *RPC-MAG: The Fluxgate Magnetometer in the ROSETTA Plasma Consortium*. Space Science Reviews, 128, 649–670, 2006.
- Goetz, C., Koenders, C., Richter, I., Altwegg, K., Burch, J., Carr, C., Cupido, E., Eriksson, A., Güttler, C., Henri, P., Mokashi, P., Nemeth, Z., Nilsson, H., Rubin, M., Sierks, H., Tsurutani, B., Vallat, C., Volwerk, M., and Glassmeier, K.-H. *First detection of a diamagnetic cavity at comet 67P/Churyumov-Gerasimenko*. Astronomy and Astrophysics, 2016a.

- Goetz, C., Koenders, C., Hansen, K. C., Burch, J., Carr, C., Eriksson, A., Frühauff, D., Güttler, C., Henri, P., Nilsson, H., Richter, I., Rubin, M., Sierks, H., Tsurutani, B., Volwerk, M., and Glassmeier, K. H. *Structure and evolution of the diamagnetic cavity at comet 67P/Churyumov-Gerasimenko*. Monthly Notices of the RAS, 462, S459–S467, 2016b.
- Goldstein, B. E., Altwegg, K., Balsiger, H., Fuselier, S. A., and Ip, W.-H. *Observations of a shock and a recombination layer at the contact surface of Comet Halley*. Journal of Geophysics Research, 94, 17251–17257, 1989.
- Gombosi, T. I. *The plasma environment of comets*. Reviews of Geophysics Supplement, 29, 976–984, 1991.
- Gombosi, T. I. Physics of Cometary Magnetospheres. In A. Keiling, C. M. Jackman, and P. A. Delamere, editors, *Magnetotails in the Solar System*, volume 207 of *American Geophysical Union Geophysical Monograph Series*, pages 169–188, January 2015.
- Grard, R., Laakso, H., Pedersen, A., Trotignon, J. G., and Mikhailov, Y. *Observations of the plasma environment of comet Halley during the Vega flybys*. Annales Geophysicae, 7, 141–150, 1989.
- Gunell, H., Goetz, C., Eriksson, A., Nilsson, H., Simon Wedlund, C., Henri, P., Maggiolo, R., Hamrin, M., Glassmeier, K.-H., Keyser, J. De, Rubin, M., Wieser, G., Stenberg, Cessateur, G., Dhooghe, F., and Gibbons, A. Plasma waves confined to the diamagnetic cavity at comet 67P/Churyumov-Gerasimenko. accepted in MNRAS, 2017.
- Gurnett, D. A., Anderson, R. R., Ma, T. Z., Haerendel, G., and Paschmann, G. *Waves and electric fields associated with the first AMPTE artificial comet*. Journal of Geophysics Research, 91, 10013–10028, 1986.
- Haas, F. A. Turbulence in fluids and plasmas. In R. O. Dendy, editor, *Plasma Physics: An Introductory Course*, pages 103 – 128. 1993.
- Hansen, K. C., Altwegg, K., Berthelier, J.-J., Bieler, A., Biver, N., Bockelée-Morvan, D., Calmonte, U., Capaccioni, F., Combi, M. R., de Keyser, J., Fiethe, B., Fougere, N., Fuselier, S. A., Gasc, S., Gombosi, T. I., Huang, Z., Le Roy, L., Lee, S., Nilsson, H., Rubin, M., Shou, Y., Snodgrass, C., Tennishev, V., Toth, G., Tzou, C.-Y., Simon Wedlund, C., and Rosina Team,. *Evolution of water production of 67P/Churyumov-Gerasimenko: An empirical model and a multi-instrument study*. Monthly Notices of the RAS, 462, S491–S506, 2016.
- Haser, L. *Distribution d'intensité dans la tête d'une comète*. Bulletin de la Société Royale des Sciences de Liège, 43, 740–750, 1957.
- Hastie, R. J. Plasma particle dynamics. In R. O. Dendy, editor, *Plasma Physics: An Introductory Course*, pages 5 – 28. 1993.
- Heinzel, G., Rüdiger, A., and Schilling, R. *Spectrum and spectral density estimation by the Discrete Fourier transform (DFT), including a comprehensive list of window functions and some new flat-top windows*, Max-Planck-Institut für Gravitationsphysik (Albert Einstein-Institut), Feb 2002.
- Hopcraft, K. I. Magnetohydrodynamics. In R. O. Dendy, editor, *Plasma Physics: An Introductory Course*, pages 77 – 102. 1993.

- Ip, W.-H. Global solar wind interaction and ionospheric dynamics. In G. W. Kronk, editor, *Comets II*, 2004.
- Israelevich, P. L. and Ershkovich, A. I. *A Giotto/cometary interaction event near the diamagnetic cavity boundary*. Journal of Geophysics Research, 99, 17, 1994.
- Israelevich, P. L., Ershkovich, A. I., Gombosi, T. I., Neubauer, F. M., and Cohen, O. *Fine structure of the diamagnetic cavity boundary in comet Halley*. Journal of Geophysical Research (Space Physics), 108, 1097, 2003.
- Jenkins, Gwilym M. and Watts, Donald G. *Spectral analysis and its applications*. Holden-Day, 1968.
- Johlander, Andreas. Photoemission on the Rosetta spacecraft. Master's thesis, Swedish Institute of Space Physics, Uppsala, Nov 2012.
- Karlsson, T., Eriksson, A. I., Odelstad, E., André, M., Dickeli, G., Kullen, A., Lindqvist, P.-A., Nilsson, H., and Richter, I. *Rosetta measurements of lower hybrid frequency range electric field oscillations in the plasma environment of comet 67P*. Geophysical Research Letters, 44, 2017.
- Koenders, C., Glassmeier, K.-H., Richter, I., Motschmann, U., and Rubin, M. *Revisiting cometary bow shock positions*. Planetary Space Science, 87, 85–95, 2013.
- Koenders, C., Glassmeier, K.-H., Richter, I., Ranocha, H., and Motschmann, U. *Dynamical features and spatial structures of the plasma interaction region of 67P/ChuryumovGerasimenko and the solar wind*. Planetary and Space Science, 105, 101 – 116, 2015.
- Krankowsky, D., Lammerzahl, P., Herrwerth, I., Woweries, J., Eberhardt, P., Dolder, U., Herrmann, U., Schulte, W., Berthelier, J. J., Illiano, J. M., Hodges, R. R., and Hoffman, J. H. *In situ gas and ion measurements at comet Halley*. Nature, 321, 326–329, 1986.
- Kreyszig, Erwin. *Advanced Engineering Mathematics*. Wiley, 10th edition, 2011.
- Laframboise, J. G. *Theory of spherical and cylindrical Langmuir probes in a collisionless, Maxwellian plasma at rest*. Tech. Rep. UTIAS report 100, Institute for Aerospace Studies, University of Toronto, 1966.
- Lai, Shu T. *A Review of Critical Ionization Velocity*. Reviews of Geophysics, 39(4), 471–506, 2001.
- Lai, Shu T. *Fundamentals of Spacecraft Charging: Spacecraft Interactions with Space Plasmas*. Princeton University Press, 2011.
- Langmuir, I. *Oscillations in Ionized Gases*. Proceedings of the National Academy of Sciences, 14, 627–637, 1928.
- Lay, David. *Linear Algebra and Its Applications*. Pearson, 2014.
- Lee, M. A. *Ultra-low frequency waves at comets*. Washington DC American Geophysical Union Geophysical Monograph Series, 53, 13–29, 1989.
- Leis, John W. *Digital Signal Processing Using MATLAB for students and researchers*. ISBN: 978-0-470-88091-3. Wiley, 2011.

- Li, Hui, Gary, S. Peter, and Stawicky, Olaf. *On the Dissipation of Magnetic Fluctuations in the Solar Wind*. Geophysical Research Letters, 28, 1347–1350, 2001.
- Mandt, K. E., Eriksson, A., Edberg, N. J. T., Koenders, C., Broiles, T., Fuselier, S. A., Henri, P., Nemeth, Z., Alho, M., Biver, N., Beth, A., Burch, J., Carr, C., Chae, K., Coates, A. J., Cupido, E., Galand, M., Glassmeier, K.-H., Goetz, C., Goldstein, R., Hansen, K. C., Haiducek, J., Kallio, E., Lebreton, J.-P., Luspay-Kuti, A., Mokashi, P., Nilsson, H., Opitz, A., Richter, I., Samara, M., Szego, K., Tzou, C.-Y., Volwerk, M., Simon Wedlund, C., and Stenberg Wieser, G. *RPC observation of the development and evolution of plasma interaction boundaries at 67P/Churyumov-Gerasimenko*. Monthly Notices of the RAS, 462, S9–S22, 2016.
- Morlet, J., Arens, G., Forgeau, I., and Giard, D. *Wave Propagation and Sampling Theory*. Geophysics, 47, 203–236, 1982.
- Narita, Yasuhito. *Plasma Turbulence in the Solar System*. Springer, 2012.
- NAVCAM, *European Space Agency's archive image browser*. <http://imagearchives.esac.esa.int/index.php?/category/9>. Accessed: March 11, 2017.
- Nemeth, Z., Burch, J., Goetz, C., Goldstein, R., Henri, P., Koenders, C., Madanian, H., Mandt, K., Mokashi, P., Richter, I., Timar, A., and Szego, K. *Charged particle signatures of the diamagnetic cavity of comet 67P/Churyumov-Gerasimenko*. Monthly Notices of the RAS, 462, S415–S421, 2016.
- Neubauer, F. M. *Giotto magnetic-field results on the boundaries of the pile-up region and the magnetic cavity*. Astronomy and Astrophysics, 187, 73–79, 1987.
- Neubauer, F. M., Glassmeier, K. H., Pohl, M., Raeder, J., Acuna, M. H., Burlaga, L. F., Ness, N. F., Musmann, G., Mariani, F., Wallisparallel, M. K., Ungstrup, E., and Schmidt, H. U. *First results from the Giotto magnetometer experiment at comet Halley*. Nature, 321, 352–355, 1986.
- Nilsson, H., Lundin, R., Lundin, K., Barabash, S., Borg, H., Norberg, O., Fedorov, A., Sauvaud, J.-A., Koskinen, H., Kallio, E., Riihelä, P., and Burch, J. L. *RPC-ICA: The Ion Composition Analyzer of the Rosetta Plasma Consortium*. Space Science Reviews, 128, 671–695, 2007.
- Nilsson, H., Stenberg Wieser, G., Behar, E., Simon Wedlund, C., Gunell, H., Yamauchi, M., Lundin, R., Barabash, S., Wieser, M., Carr, C., Cupido, E., Burch, J. L., Fedorov, A., Sauvaud, J.-A., Koskinen, H., Kallio, E., Lebreton, J.-P., Eriksson, A., Edberg, N., Goldstein, R., Henri, P., Koenders, C., Mokashi, P., Nemeth, Z., Richter, I., Szego, K., Volwerk, M., Vallat, C., and Rubin, M. *Birth of a comet magnetosphere: A spring of water ions*. Science, 347(1), 2015.
- Nilsson, H., Stenberg Wieser, G., Behar, E., Simon Wedlund, C., Kallio, E., Gunell, H., Edberg, N. J. T., Eriksson, A. I., Yamauchi, M., Koenders, C., Wieser, M., Lundin, R., Barabash, S., Mandt, K., Burch, J. L., Goldstein, R., Mokashi, P., Carr, C., Cupido, E., Fox, P. T., Szego, K., Nemeth, Z., Fedorov, A., Sauvaud, J.-A., Koskinen, H., Richter, I., Lebreton, J.-P., Henri, P., Volwerk, M., Vallat, C., and Geiger, B. *Evolution of the ion environment of comet 67P/Churyumov-Gerasimenko. Observations between 3.6 and 2.0 AU*. Astronomy and Astrophysics, 583, A20, 2015.
- NIST. <http://webbook.nist.gov/cgi/cbook.cgi?ID=C7732185&Mask=20>. Accessed: May 25, 2017.

- Odelstad, E., Eriksson, A. I., Edberg, N. J. T., Johansson, F., Vigren, E., André, M., Tzou, C.-Y., Carr, C., and Cupido, E. *Evolution of the plasma environment of comet 67P from spacecraft potential measurements by the Rosetta Langmuir probe instrument*. Geophysics Research Letters, 42, 10126–10135, 2015.
- Odelstad, E., Stenberg-Wieser, G., Wieser, M., Eriksson, A. I., Nilsson, H., and Johansson, F. L. Measurements of the electrostatic potential of Rosetta at comet 67P. 14th Spacecraft charging technology conference, ESA/ESTEC, April 2016.
- Olofsson, Peter and Andersson, Mikael. *Probability, Statistics, and Stochastic Processes*. Wiley, 2012.
- Oppenheim, Alan V. and Willsky, A. S. *Signals and Systems*. Prentice Hall, 1982.
- Oppenheim, Alan V., Schaffer, Ronald W., and Buck, John R. *Discrete-Time Signal Processing*. Prentice Hall, 1999.
- PDS, NASA Planetary Data System, Instrument information, RPC-LAP. https://pds.jpl.nasa.gov/ds-view/pds/viewInstrumentProfile.jsp?INSTRUMENT_ID=RPCLAP&INSTRUMENT_HOST_ID=R0. Accessed: March 11, 2017.
- Hans L. Pécseli, *Waves and Oscillations in Plasmas*. University of Oslo, Norway, 2014.
- Pröls, Gerd W. *Physics of the Earth's Space Environment - An introduction*. Springer, 2010.
- PSA, European Space Agency's Planetary Science Archive. <https://archives.esac.esa.int/psa/>. Accessed: February 14, 2017.
- Reitz, J.R., Milford, F.J., and Christy, Robert W. *Foundations of electromagnetic theory*. Addison-Wesley, 4 edition, 2008.
- Richter, I., Koenders, C., Auster, H.-U., Frühauff, D., Götz, C., Heinisch, P., Perschke, C., Motschmann, U., Stoll, B., Altwegg, K., Burch, J., Carr, C., Cupido, E., Eriksson, A., Henri, P., Goldstein, R., Lebreton, J.-P., Mokashi, P., Nemeth, Z., Nilsson, H., Rubin, M., Szegö, K., Tsurutani, B. T., Vallat, C., Volwerk, M., and Glassmeier, K.-H. *Observation of a new type of low-frequency waves at comet 67P/Churyumov-Gerasimenko*. Annales Geophysicae, 33, 1031–1036, 2015.
- Savin, S., Avanesova, G., Balikhin, M., Klimov, S., Sokolov, A., Oberc, P., Orlowski, D., and Krawczyk, Z. ELF waves in the plasma regions near the comet. In B. Battrock, E. J. Rolfe, and R. Reinhard, editors, *ESLAB Symposium on the Exploration of Halley's Comet*, volume 250 of *ESA Special Publication*, December 1986.
- Schmude, Richard. *Comets and how to observe them*. Springer, 2010.
- Schott, L. Electrical Probes. In W. Lochte-Holtgreven, editor, *Plasma Diagnostics*, chapter 11, pages 668–731. 1968.
- Simon Wedlund, C., Kallio, E., Alho, M., Nilsson, H., Stenberg Wieser, G., Gunell, H., Behar, E., Pusa, J., and Gronoff, G. *The atmosphere of comet 67P/Churyumov-Gerasimenko diagnosed by charge-exchanged solar wind alpha particles*. Astronomy and Astrophysics, 587, A154, 2016.

- Simon Wedlund, Cyril, Alho, M., Gronoff, G., Kallio, E., Gunell, H., Nilsson, H., Lindkvist, J., Behar, E., Wieser, G. Stenberg, and Miloch, W. J. *Hybrid modelling of cometary plasma environments: Impact of photoionisation, charge exchange and electron ionisation on bow shock and cometopause at 67P/Churyumov-Gerasimenko*. Astronomy & Astrophysics, 2017.
- Sonnerup, B. U. O. and Cahill, L. J.Jr. *Magnetopause Structure and Attitude from Explorer 12 Observations*. Journal of Geophysics Research, 72, 171, 1967.
- Sonnerup, Bengt U. Ö. and Screible, Maureen. Minimum and Maximum Variance Analysis. In Götz Paschmann and Patric W. Daly, editor, *Analysis Methods for Multi-Spacecraft data*, pages 185–220. 2000.
- Spicher, Andres. Spectral Analysis of the Electron Density Fluctuations Measured by the ICI-2 Sounding Rocket. Master thesis, University of Oslo, Department of Physics, Norway, Mai 2013.
- Spicher, Andres, Miloch, W. J., and Moen, J. I. *Direct evidence of double-slope power spectrain the high-latitude ionospheric plasma*. Geophysical Research Letters, 41, 1406–1412, 2014.
- Spiegel, Murray R., Lipschutz, Seymour, and Lui, Joh. *Mathematical Handbook of Formulas and Tables*. Schaum's outlines. McGraw-Hill, 3 edition, 2009.
- Sturrock, Peter A. *Plasma Physics: An Introduction to the Theory of Astrophysical, Geophysical & Laboratory Plasmas*. Cambridge University Press., 1994.
- Thorne, R. M. and Tsurutani, B. T. *Resonant interactions between cometary ions and low frequency electromagnetic waves*. Planetary Space Science, 35, 1501–1511, 1987.
- Torrence, C. and Compo, G.P. *A Practical Guide to Wavelet Analysis*. Bulletin of the American Meteorological Society, 79, 61–78, 1998.
- Trotignon, J. G., Michau, J. L., Lagoutte, D., Chabassière, M., Chalumeau, G., Colin, F., Décréau, P. M. E., Geiswiller, J., Gille, P., Grard, R., Hachemi, T., Hamelin, M., Eriksson, A., Laakso, H., Lebreton, J. P., Mazelle, C., Randriamboarison, O., Schmidt, W., Smit, A., Telljohann, U., and Zamora, P. *RPC-MIP: the Mutual Impedance Probe of the Rosetta Plasma Consortium*. Space Science Reviews, 128, 2007.
- Tsurutani, B. T. and Smith, E. J. *Hydromagnetic waves and instabilities associated with cometary ion pickup - ICE observations*. Geophysics Research Letters, 13, 263–266, 1986.
- Tsurutani, B. T., Glassmeier, K.-H., and Neubauer, F. M. *An intercomparison of plasma turbulence at three comets: Grigg-Skjellerup, Giacobini-Zinner, and Halley*. Geophysics Research Letters, 22, 1149–1152, 1995.
- Wyckoff, S., Tegler, S., Wehinger, P. A., Spinrad, H., and Belton, M. J. S. *Abundances in Comet Halley at the time of the spacecraft encounters*. Astrophysical Journal, 325, 927–938, 1988.
- Young, D. T., Crary, F. J., Nordholt, J. E., Bagenal, F., Boice, D., Burch, J. L., Eviatar, A., Goldstein, R., Hanley, J. J., Lawrence, D. J., McComas, D. J., Maier, R., Reisenfeld, D., Sauer, K., and Weins, R. C. *Solar wind interactions with Comet 19P/Borrelly*. Icarus, 167, 80–88, 2003.

A

MATLAB SCRIPTS

Here a selection of MATLAB functions implemented for the analysis of this work is presented. Everything is coded and commented by the author, but pre-coded MATLAB functions are included whenever used. Scripts modelling and generating plots for the theory and method chapters are left out. Text-reading scripts and plotting methods are also excluded from this appendix.

Least-squares method

```
function [b1,b2] = LeastSquaresFit(X,Y)

%Find slope and intersection with y-axis of linear fit to data X-Y using
%the least-squares method

%Input: data vectors X and Y
%Output: slope b1 and y-axis intersection value b2 of linear regression

n = length(X);

X_sum = 0;
Y_sum = 0;
XY_sum = 0;
X_sqrt_sum = 0;
for i = 1:n
    X_sum = X_sum + X(i);
    Y_sum = Y_sum + Y(i);
    XY_sum = XY_sum + X(i) * Y(i);
    X_sqrt_sum = X_sqrt_sum + X(i) * X(i);
end

b1 = (n*XY_sum-X_sum*Y_sum)/(n*X_sqrt_sum-X_sum*X_sum); %slope
b2 = (Y_sum-b1*X_sum)/n; %intersection with y-axis
```

Probe calibration

```
function [V2_10] = ProbeCalibration(V1,V2)

%Calibration of LAP probe potentials
%This is done by dividing V2 with const b1 and subtract const a2 to make
%linear regression of V1-V2-plot have slope 1 that cross (0,0) using the
%least-suares method

%Inputs: Uncalibrated probe potentials V1 and V2
%Output: Calibrated probe potential V2_10
%(V1 is not changed in the calibration)

% Find slope b1 of uncalibrated V1-V2
[b1,b2] = LeastSquaresFit(V1,V2);
V2_10 = V2./b1;
%Find y-axis intersection with semi-calibrated V1-V2
[a1,a2] = LeastSquaresFit(V1,V2_10);
V2_10 = V2_10 - a2;
```

Transformation of magnetic field components to electric field coordinate system

```
function [B1,B2,B3] = Transform2Efield(Bx,By,Bz)

% Translate magnetic field components (Bx,By,Bz) in s/c coordinates
% to magnetic field components (B1,B2,B3) in E-field coordinates
% The E-coordinates defined and normalized and defined such that
% Ecoord is parallel to E-field estimate, whilst E2 and E3 are
% perpendicular and completes the system

% Inputs: calibrated magnetic field components in s/c coordinate system
% Outputs: magnetic field components in E-field coordinate system

x1 = [1,0,0]; % Used in the computation of E2 (and E3)
P1 = [-1.19, 2.43, 3.88]; % Position of LAP1 in s/c coordinate system
P2 = [-2.48, 0.78, -0.65]; % Position of LAP2 in s/c coordinate system

% Generation and normalization of E-field coordinate vectors in s/c system
Ecoord = P2-P1; Ecoord = Ecoord./norm(Ecoord); Ecoord = Ecoord';
E2 = cross(x1,Ecoord); E2 = E2./norm(E2); E2 = E2';
E3 = cross(Ecoord,E2); E3 = E3./norm(E3); E3 = E3';

% Transformation matrix and its inverse
P = [Ecoord E2 E3];
Pinv = inv(P);

% Transformation of (Bx,By,Bz) to (B1,B2,B3)
Bxyz = [Bx';By';Bz'];
B123 = Pinv*Bxyz;
B1 = B123(1,:); B2 = B123(2,:); B3 = B123(3,:);
```

Symmetric matrix for minimum variance analysis (MVA)

```
function [M_B] = compute_sym_var_matrix(B)

% Computes symmetric variance matrix used in the minimum variance analysis

% Input: Magnetic field vector
% Output: symmetric variance matrix

N = length(B);
M_B = 0;

for i=1:3
    for j=1:3
        BiBj_avg = 0;
        Bi_avg = 0;
        Bj_avg = 0;
        for n=1:N
            BiBj_avg = BiBj_avg + B(n,i)*B(n,j);
            Bi_avg = Bi_avg + B(n,i);
            Bj_avg = Bj_avg + B(n,j);
        end
        BiBj_avg = BiBj_avg/N;
        Bi_avg = Bi_avg/N;
        Bj_avg = Bj_avg/N;
        M_B(i,j) = BiBj_avg - Bi_avg*Bj_avg;
    end
end
```

Minimum variance analysis (MVA)

```
function [B_1,B_2,B_3,B123,V,D] = MVA(Bx,By,Bz)

% Minimum variance analysis of magnetic field components

% Inputs: Magnetic field components (Bx,By,Bz)
% Outputs: Magnetic field components (B_1,B_2,B_3) in MVA system, magnetid
% field magnitude B123 and MVA vectors V and variance D

Bxyz(:,1) = Bx; Bxyz(:,2) = By; Bxyz(:,3) = Bz;
N = length(Bxyz);
% Find symmetric variance matrix:
[M_B] = compute_sym_var_matrix(Bxyz);

[V,D] = eig(M_B); V_inv = inv(V); %V: Eigenvectors in same coordinates as B
                                %D: corresponding eigenvalues

% Translate B to MVA system:
B_new = 0;
for n=1:N
    for i=1:3
        B_new(n,i) = 0;
```

```

        for j=1:3
            B_new(n,i) = B_new(n,i) + V_inv(i,j)* Bxyz(n,j);
        end
    end
end
% New magnetic coordinates %
B_1 = B_new(:,1); B_2 = B_new(:,2); B_3 = B_new(:,3);
B123 = sqrt(B_1.*B_1 + B_2.*B_2 + B_3.*B_3);

```

Computing temperature profile

```

function [Te] = ComputeT(tLAP,V1,tMIP,ne)

% Compute temperature profile from LAP probe potentials and MIP electron
% densities at the time resolution of MIP

% Inputs: LAP time vector tLAP and probe potential V1, MIP time vector tMIP
% and electron density ne
% Outputs: estimated electron temperature Te (in eV) following tMIP

syms T
K = 0.0211;    % Estimated constant
T0 = 5;        % Initial temperature guess
frac = 0.9;    % Fraction of spacecraft potential picked up p LAP1

V1_resamp = interp1(tLAP,V1,tMIP); % Resample V1 to tMIP

Te = [];
for i=1:length(V1_resamp) % Solve equation for T over entire time interval
    Te(i) = vpasolve(V1_resamp(i) - frac.*T.*log(K.*ne(i).*sqrt(T)) == 0,T,T0);
end

```

Computation of Fourier power spectral density

```

function [f,psd] = Calc_PSD(t,X,Fs,length_int,num)

% Computes power spectral density psd and corresponding frequency f using
% the Fourier method and fast Fourier transform (FFT)
% A Hanning-window is applied to the time data if num = 1

% Inputs: time vector t, signal vector X, sampling frequency Fs (in Hz),
% interval length length_int (in s) and value num determining whether a
% Hanning-window should be applied to signal (num = 1 gives
% Hanning-windowed signal)
% Outputs: power spectral density psd and relates frequency f (in Hz)

X = X - mean(X); % Remove mean from signal
N = Fs*length_int; % Length of interval
f = 0/N:Fs/N:Fs/2; % Frequency vector

```

```

% Apply Hanning window is num = 1
if num == 1
    L = length(t);
    window = hann(L,'periodic');
    W_ss = sum(window.^2)/L;    % For loss-correction os PSD
    X = (X).*window;
end

% Compute power spectral density, psd:
xdft = fft(X,N); % Fast Fourier transform
xdft = xdft(1:(N/2 + 1));
psd = (1/(N*Fs)) * abs(xdft).^2;
if num == 1                % Correct for symmetry
    psd(2:end-1) = 2*psd(2:end-1)./W_ss; % If window applied, loss-correct PSD
else
    psd(2:end-1) = 2*psd(2:end-1);
end

```

LAP electric field power spectral density between data gaps

```

function [f,psd,datagap] = PSDbetweenDatagaps(t,E)

% Compute electric field sub-PSDs between data gaps
% For every sampling of ~31 s, 5 sub-PSDs are generated from intervals of
% roughly 10 s and with a 50 % overlap

% Inputs: time vector t, (possibly detrended) electric field vector E
% Outputs: frequency vector f, power spectral density matrix psd, and data
% gap vector

Fs = 57.8; % Sampling frequency of LAP electric field mode

% Create data gap vector:
% The elements of the vectors are the indices of the points right before
% and right after the data gaps
% In the data gaps vector, the first relevant element is datagap(3).
% That element contains the index of the first element after the first data
% gap.
datagap = 0;
for i=2:1:length(t)
    if ((t(i) - t(i-1)) > 0.1)
        % Since the sampling frequency of the electric field mode is 57.8 Hz,
        % the sampling period is less than 0.02 s. Hence, data points separated
        % by more than 0.1 s are separated by a data gap
        datagap = [datagap i-1];
        datagap = [datagap i];
    end
end
num_gaps = (length(datagap)-1)/2; % Number of data gaps

```

```

% Compute Fourier PSDs using only data between data gaps:
fx = []; psd = [];
for i=1:(num_gabs-1)
% Number of intervals is one less than number of data gaps
    ti = datagap(i*2+1); % First element after chosen data gap
    tf = datagap(i*2+2); % Last element before next data gap
    dt = ((tf - ti));
    t2 = int32(ti + dt/6); t3 = int32(ti + 2*dt/6);
    t4 = int32(ti + 3*dt/6); t5 = int32(ti + 4*dt/6);
    dts = dt/(Fs*3);
    [f1,psd1] = Calc_PSD(t(ti:t2),E(ti:t2),Fs,dts,1);
    [f2,psd2] = Calc_PSD(t(t2:t3),E(t2:t3),Fs,dts,1);
    [f3,psd3] = Calc_PSD(t(t3:t4),E(t3:t4),Fs,dts,1);
    [f4,psd4] = Calc_PSD(t(t4:t5),E(t4:t5),Fs,dts,1);
    [f5,psd5] = Calc_PSD(t(t5:tf),E(t5:tf),Fs,dts,1);
    fx = [fx; f1; f2; f3; f4; f5];
    psd = [psd; psd1'; psd2'; psd3'; psd4'; psd5'];
end
psd = psd';
f = fx(1,:); % Make frequency matrix to vector since all frequencies are
              % generated in same way in Cal_PSD function

```

Power spectral density of LAP high-frequency electric field

```

function [f,psd] = HighFreqPSD(t,V1,V2,time1,time2)

% Inputs: time vector t, probe potentials V1 and V2, and time interval
% [t1,t2], where t1 and t2 are second of day
% Output: high-sampling frequency power spectral density vector psd and
% related frequency vector

% Mode information
int = 32; % sec between data
samples = 432; % number of samples per sampling
Fs = 18750; % sampling frequency
time_int = samples/Fs; % total time of sampling
t_step = 1/Fs; % sampling period

% Change length of vectors'
t_start = t(1);
tp_start = time1 - t_start;
tp_end = time2 - t_start;
x1 = int32((tp_start/int))*samples + 1;
x2 = int32((tp_end/int))*samples;
t = t(x1:x2); V1 = V1(x1:x2); V2 = V2(x1:x2);

% compute PSDs for each sampling interval
f = 0; psd = 0;
num_int = (x2-x1)/samples; % number of sampling intervals in picked data
for i=1:(num_int-1) % i runs over all sampling intervals

```

```

t_temp = t((i*samples +1):((i+1)*samples));
V1_temp = V1((i*samples +1):((i+1)*samples));
V2_temp = V2((i*samples +1):((i+1)*samples));
[V2_temp] = ProbeCalibration(t_temp,V1_temp,V2_temp); % Probe calibration
E_temp = (V2_temp - V1_temp)./(5.0).*1000; % Compute E
[f_temp,psd_temp] = Calc_PSD(t_temp,E_temp,Fs,time_int,1); % Compute PSD
for j=1:length(f_temp) % Add PSD and
    f(i,j) = f_temp(j);
    psd(i,j) = psd_temp(j);
end
end

```

Power-law relation

```

function [X,Y,b1,b2,R2] = PowerLawSlope(f,psd,f1,f2)

% Computes the exponent b1 of the power-law relation in the frequency range
% from f1 to f2 along with the linear regression Y = b1*X + b2 in log-log
% scale and R-squared value of the linear regression

% Inputs: frequency f, power spectral density psd, start and end
% frequency-indices f1 and f2 of f (i.e. [f(f1);f(f2)] gives the frequency
% range of the power-law computation)

% Find slope of data in log-log scale:
num = f2 - f1;
X1 = 0; X2 = 0;
for i=1:num
    j = i + f1;
    X1(i) = log(f(j));
    X2(i) = log(psd(j));
end
[b1,b2] = LeastSquaresFit(X1,X2); % Linear regression

% Linear regression data in linear scale:
X = exp(X1);
Y_temp = b1*X1 + b2; Y = exp(Y_temp);

% Compute R-squared:
mean_Y = mean(psd(f1:f2));
nom = 0; denom = 0;
for i=1:num
    j = i + f1;
    nom = nom + (psd(j) - Y(i))*(psd(j) - Y(i));
    denom = denom + (psd(j) - mean_Y)*(psd(j) - mean_Y);
end
R2 = 1 - nom/denom;

```

B**PROBE CALIBRATION**

The LAP probe calibrations used for the estimations of the low-frequency LAP electric field estimates are presented in the figures below. Each plot shows the time interval, over which the calibration is done, and the slope b_1 and the V_2 -value, b_2 , for $V_1 = 0$ of the least-squares method linear regression of the uncalibrated probe potentials. The 2015-10-25 calibration is used for the Section 3.3.3 reproduction of the electric field fluctuations studied by Karlsson et al. (2017), and is also presented in Figure 3.7 to exemplify the calibration method. The 2015-05-28 and 2016-02-17 figures give the probe calibrations during the cavity crossing events studied in Chapter 4. The two calibration intervals on 2016-02-17 are caused by the shadowing of LAP2. The probe calibrations for time intervals in May 2016 are used in the estimation of the electric fields in Appendix F.

The probe calibrations of the high-frequency electric field signals presented in Section 4.2.1 are not included in the appendix, since the calibration of the high-frequency sampling are done for every sampling interval, causing numerous calibrations for the considered time intervals.

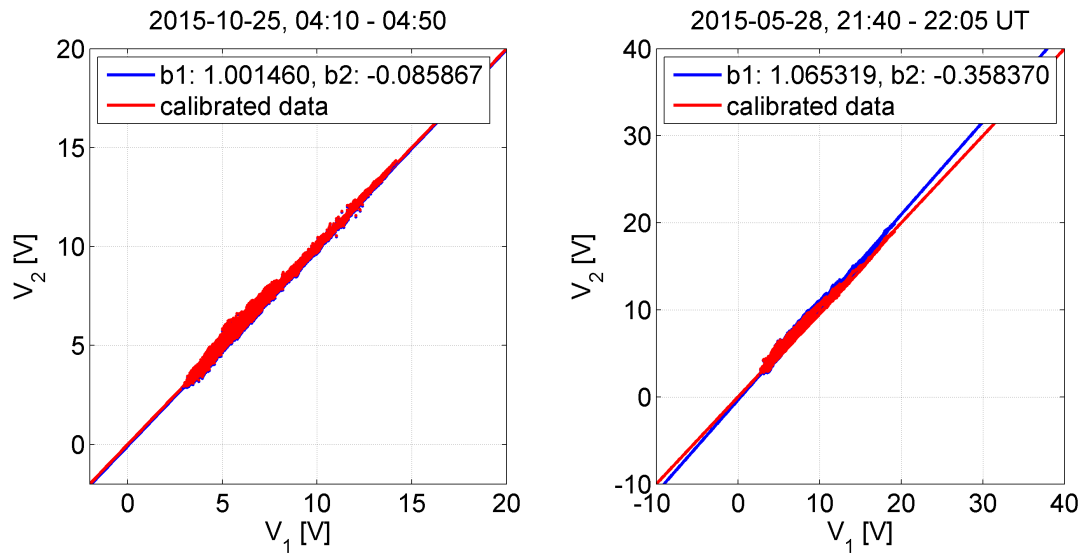


Figure B.1. Probe potential calibration during the intervals 04:10 - 04:50 UT on October 15, 2015, and 21:40 - 22:05 UT on May 28, 2015.

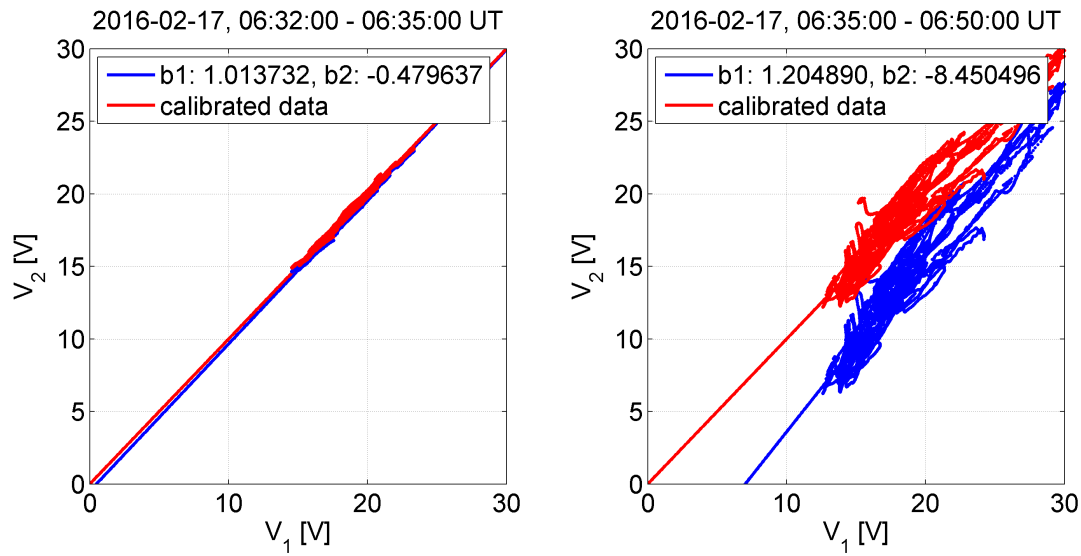


Figure B.2. Probe potential calibration during the intervals 06:32-06:35 UT and 06:35 - 06:50 UT on February 17, 2016.

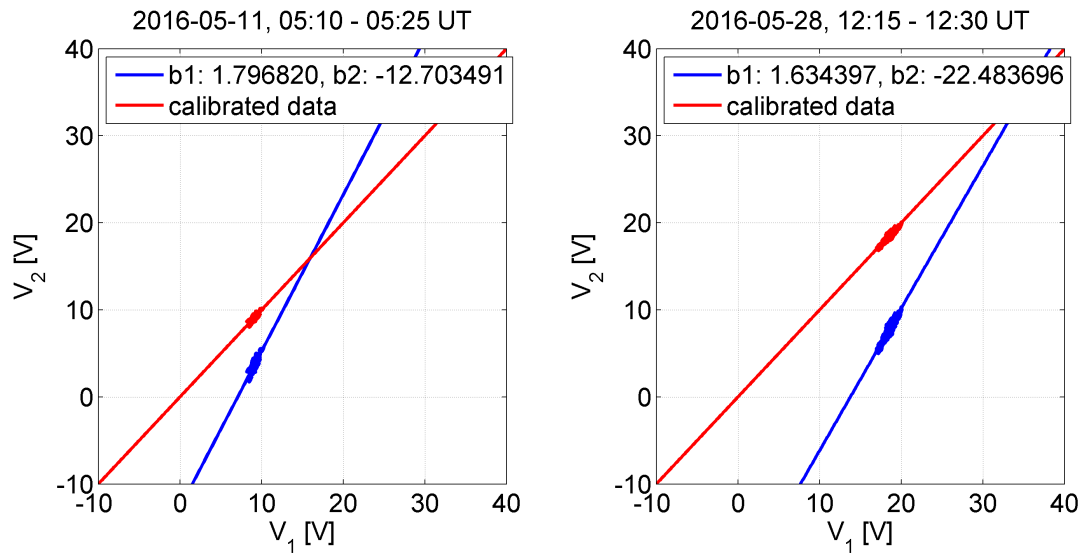


Figure B.3. Probe potential calibration during the intervals 05:10 - 05:25 UT on May 11, 2016, and 12:15 - 12:30 UT on May 28, 2016.

C

IES ION AND ELECTRON ENERGY SPECTROGRAMS

The figures below give the IES ion and electron energy-per-charge spectrograms for time spans over the studied cavity events. For May 2015, the vertical red lines limit the region outside the ion-neutral collisionopause defined by Mandt et al. (2016), and for both events, the vertical black lines mark the approximate temporal positions of the cavity observations. The spectrograms are discussed in Section 4.1.3 of the results and discussion chapter, and are included here to support the discussed statements.

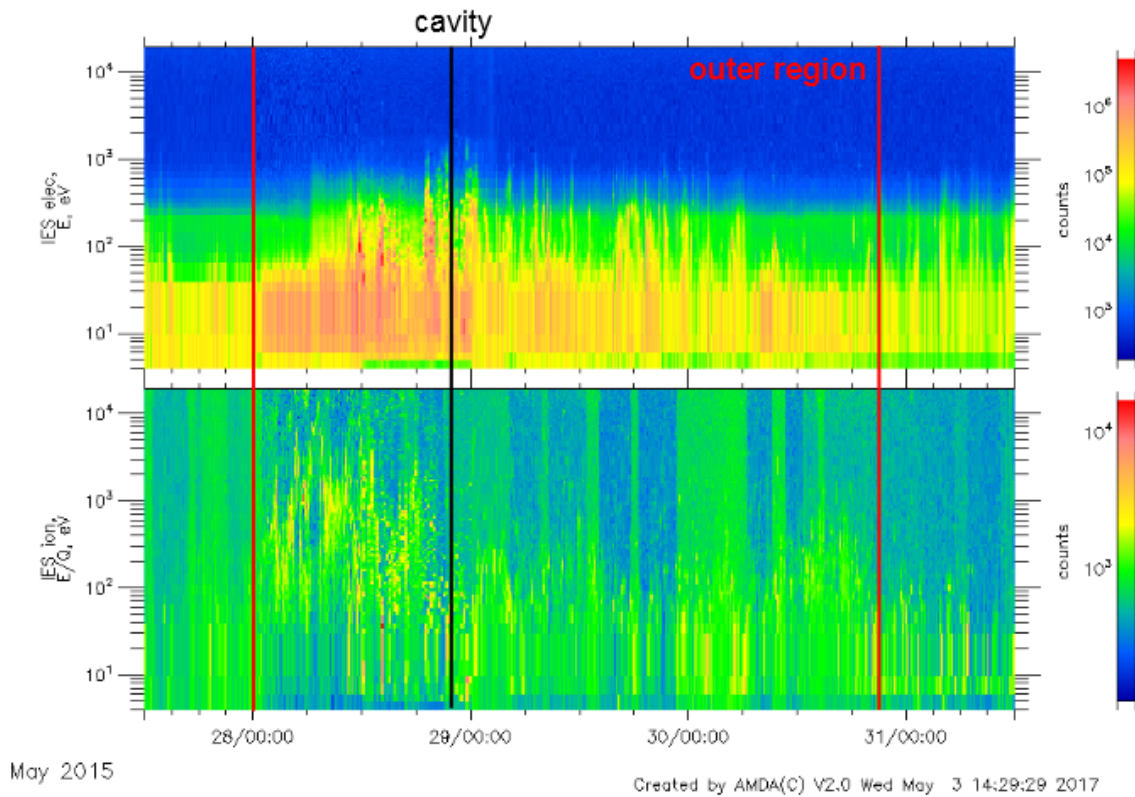


Figure C.1. Electron and ion energy-per-charge spectrograms from 12:00 UT on May 27, 2015, to 12:00 UT on May 31, 2015. The vertical red lines limit the "outer" region determined by Mandt et al. (2016), whilst the vertical black line gives the approximate time for the cavity crossing at 21:50 - 21:54 UT on May 28, 2015.

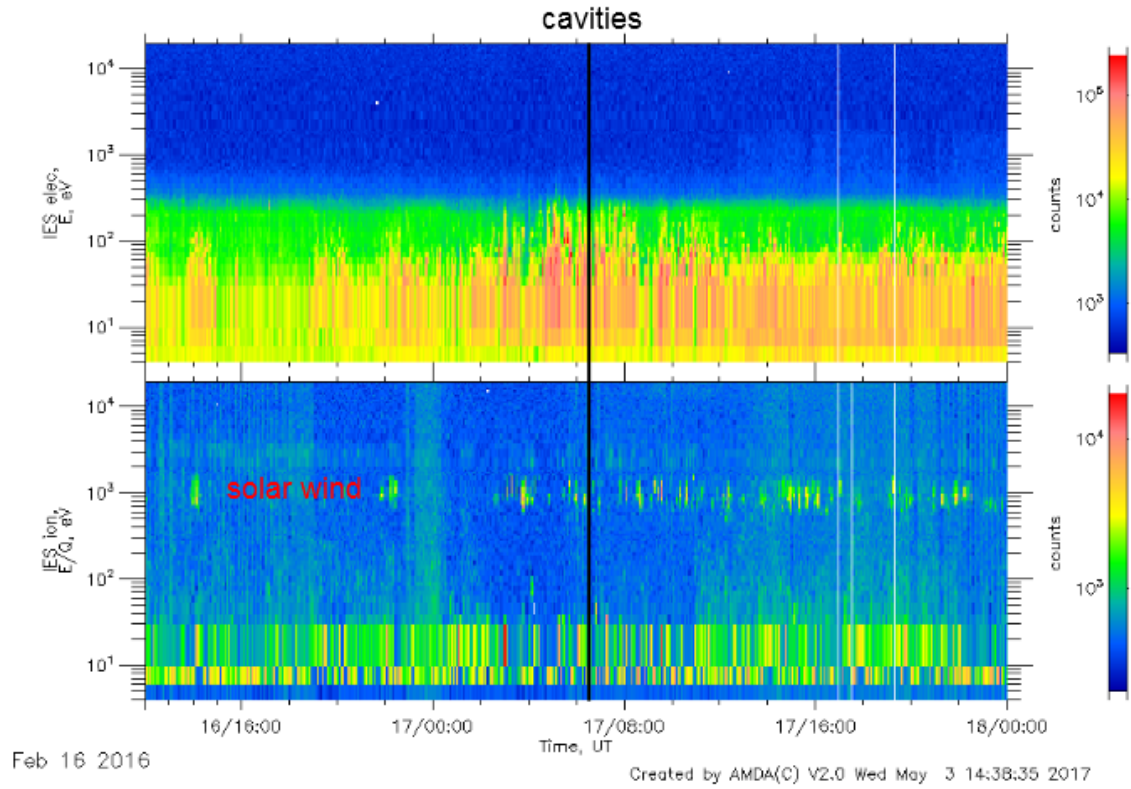
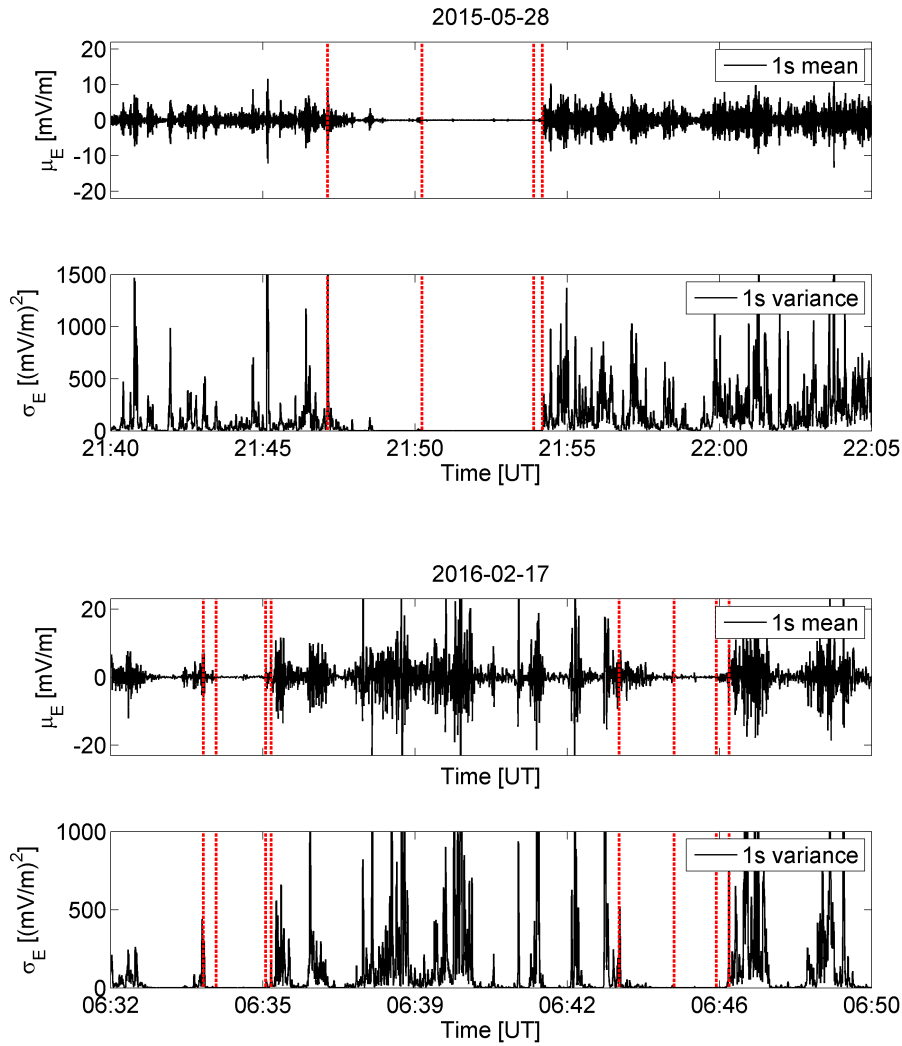


Figure C.2. Electron and ion energy-per-charge spectrograms from 12:00 UT on February 16, 2016, to 00:00 UT on February 18, 2016. The vertical black line gives the approximate time for the cavities observations at 06:35 UT and 06:46 UT on February 17, 2016.

D

DEFINING CAVITY BOUNDARIES FROM ELECTRIC FIELD ESTIMATES

The figures below give the 1 s mean μ_E and variance σ_E^2 of the LAP electric field estimate during the studied cavity crossings, presented in Section 4.1.4. The dashed red lines give the temporal position of the beginning of the inbound DCBLs, the in- and outbound contact surfaces, and the end of the outbound DCBLs determined by eye from the statistical properties of the electric field estimate.



ZOOM-INS ON CAVITIES

The figures below give the cavity-calibrated magnetic field components, calibrated probe potentials, moving average-detrended electric field estimates, and Fourier and Morlet wavelet spectrograms during the low-frequency wave signatures in the LAP electric field estimate during the cavity crossing on May 28, 2015. These low-frequency wave signatures are further studied in Section 4.2.2. Vertical lines are superimposed on the plots to indicate the location of the low-frequency peaks in the spectrograms. The electric field has been detrended by subtracting a moving average spanning over 27 data points, corresponding to roughly 0.5 s. This detrending suppresses signatures below 2 Hz, making the peaks more easily detectable.

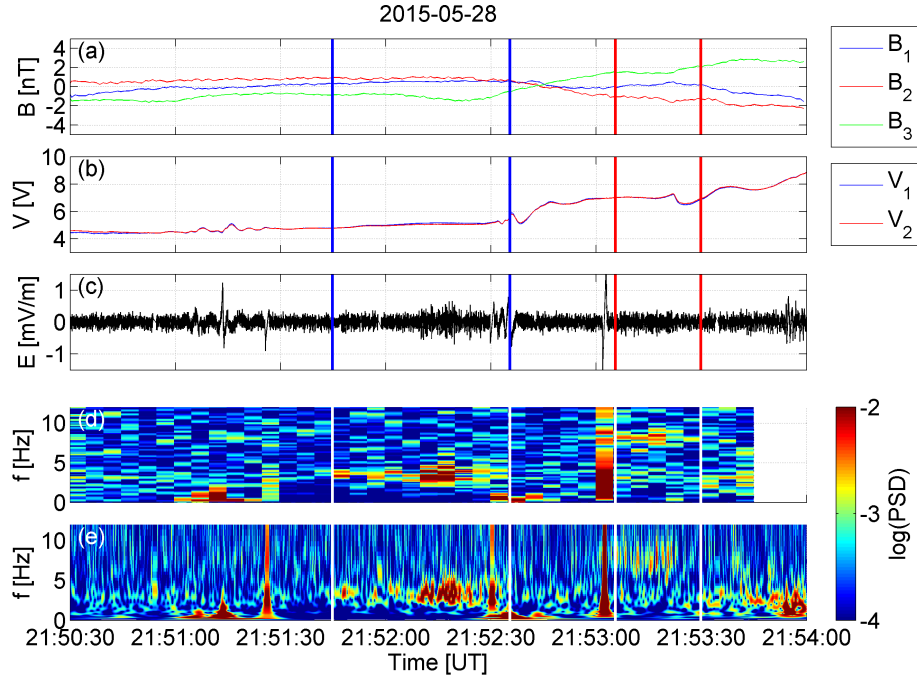


Figure E.1. (a) Cavity-calibrated magnetic field components, (b) calibrated probe potentials, (c) moving average-detrended electric field estimates and (d) Fourier and (e) Morlet wavelet spectrograms of the cavity crossing on May 28, 2015.

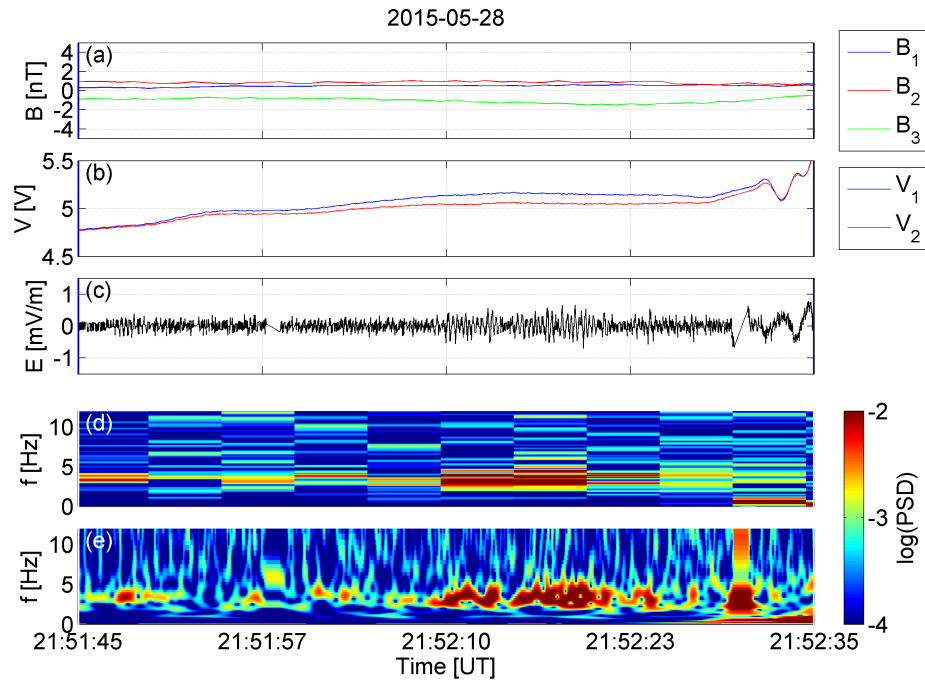


Figure E.2. Zoom-in on the 3.5 Hz peak. (a) Cavity-calibrated magnetic field components, (b) calibrated probe potentials, (c) moving average-detrended electric field estimates and (d) Fourier and (e) Morlet wavelet spectrograms.

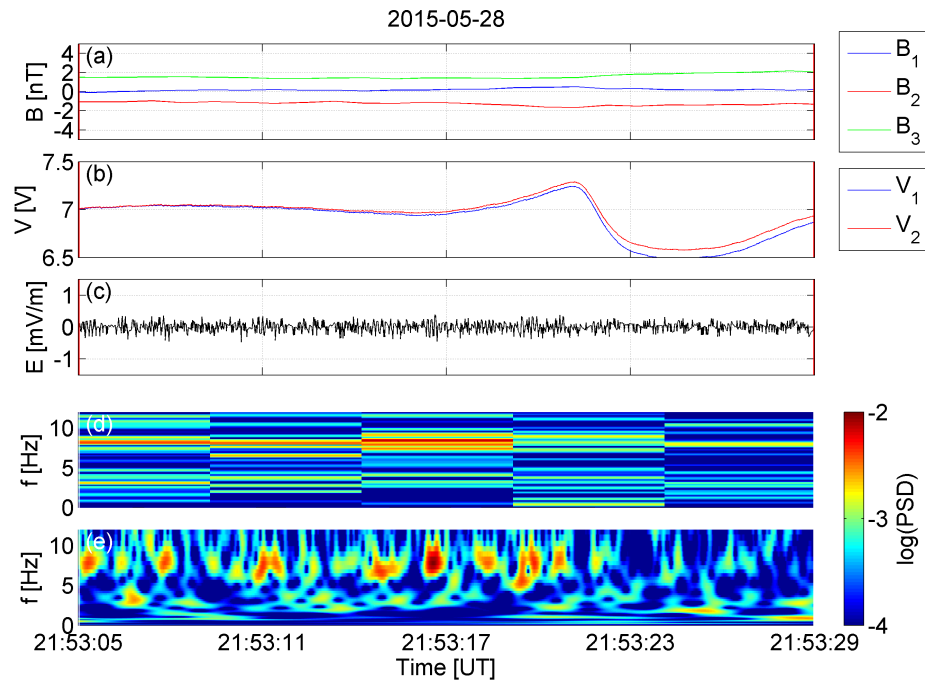


Figure E.3. Zoom-in on the 8 Hz peak. (a) Cavity-calibrated magnetic field components, (b) calibrated probe potentials, (c) moving average-detrended electric field estimates and (d) Fourier and (e) Morlet wavelet spectrograms.

HORIZONTAL LINE SIGNATURES

The table shows the frequency and power of peaks seen in the averaged electric field Fourier PSD on February 17, 2016 (see Figure 4.11(a)), and are included here to validate that the horizontal line peaks are seen in the Fourier spectrogram for roughly every 1 Hz with decreasing power for increasing frequencies, suggesting that they might be harmonics of a 1 Hz signal. The frequencies that also appears in the averages of the Morlet wavelet spectra are marked in bold.

Table F.1. Frequency and power of the peaks observed in the averaged electric field Fourier PSD on February 17, 2016, of Figure 4.11(a). The peaks marked in bold are observed in both the Fourier and Morlet wavelet methods.

Peak #	f [Hz]	$P \pm 30\%$ [(mV/m) ²]
1	2.0	1.2×10^{-1}
2	3.0	2.9×10^{-2}
3	4.0	1.8×10^{-2}
4	5.0	2.5×10^{-2}
5	6.0	5.0×10^{-2}
6	8.0	2.4×10^{-2}
7	9.0	9.9×10^{-3}
8	9.9	9.1×10^{-3}
9	11	2.8×10^{-3}
10	12	5.2×10^{-3}
11	13	7.7×10^{-3}

The figures below give the solar aspect angles (SAA), calibrated probe potentials, detrended electric fields, data gap-filtered Fourier spectrograms and the Morlet wavelet spectrograms for two days in May 2016, when the SAA is below 107°, causing a shadowing of LAP2 and ultimately the appearance of horizontal lines in the spectrograms. Similar horizontal lines appear in the electric field spectrogram on February 17, 2016, when LAP2 is shadowed (see Section 4.2). The fact that the horizontal lines are detected on multiple days when LAP2 is shaded, supports the claim that the appearance of the peaks is related to the shadowing of LAP2. The Morlet spectrograms, additionally, shows vertical lines caused by the electric field sampling mode data gaps. These are filtered out in the Fourier spectrograms.

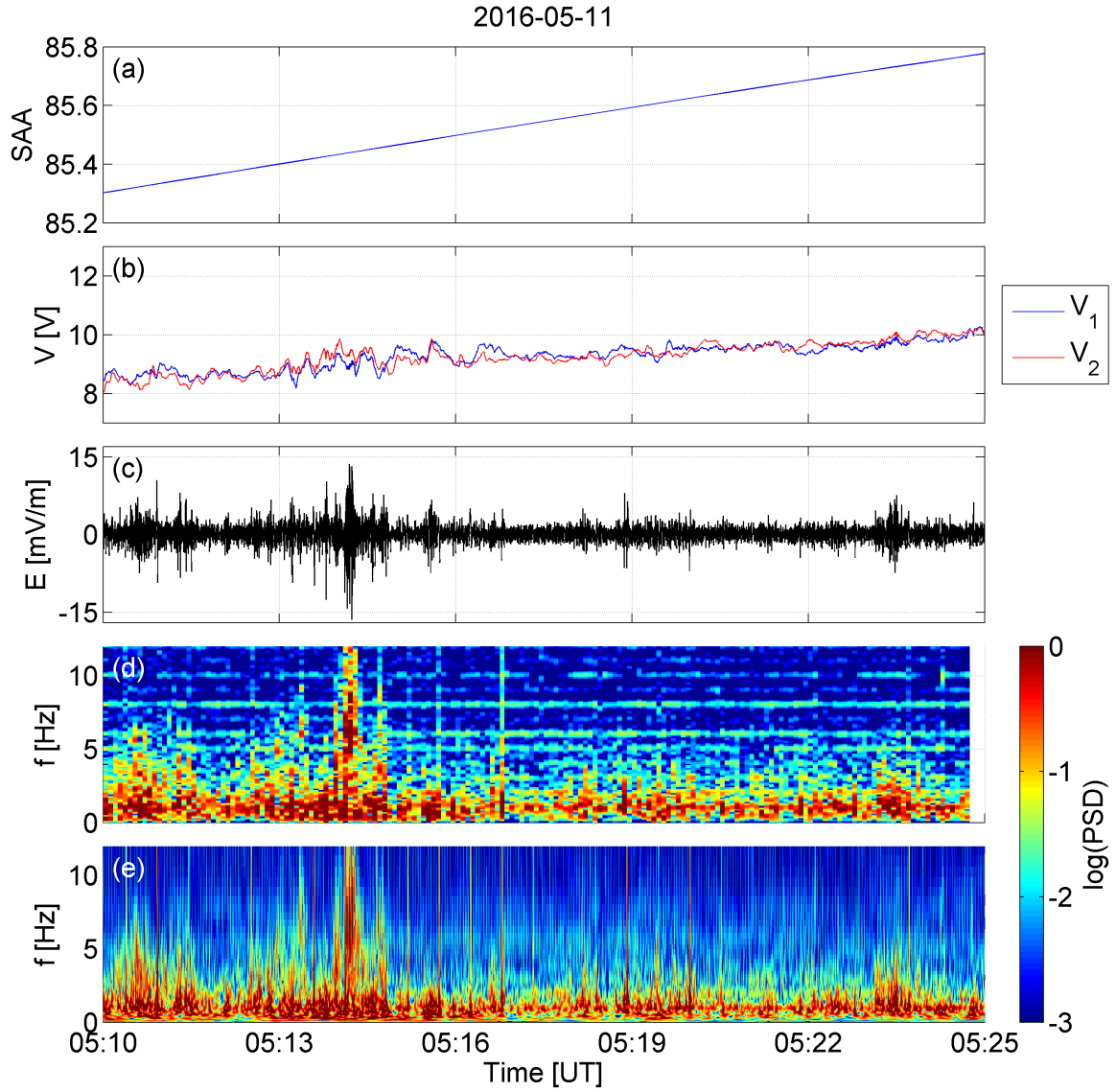


Figure F.1. (a) Solar aspect angle (SAA), (b) calibrated probe potential, (c) detrended electric field, (d) Fourier spectrogram and (e) Morlet wavelet spectrogram for a time interval from 05:10 UT to 05:25 UT on May 11, 2016, when horizontal lines appear in the spectrograms.

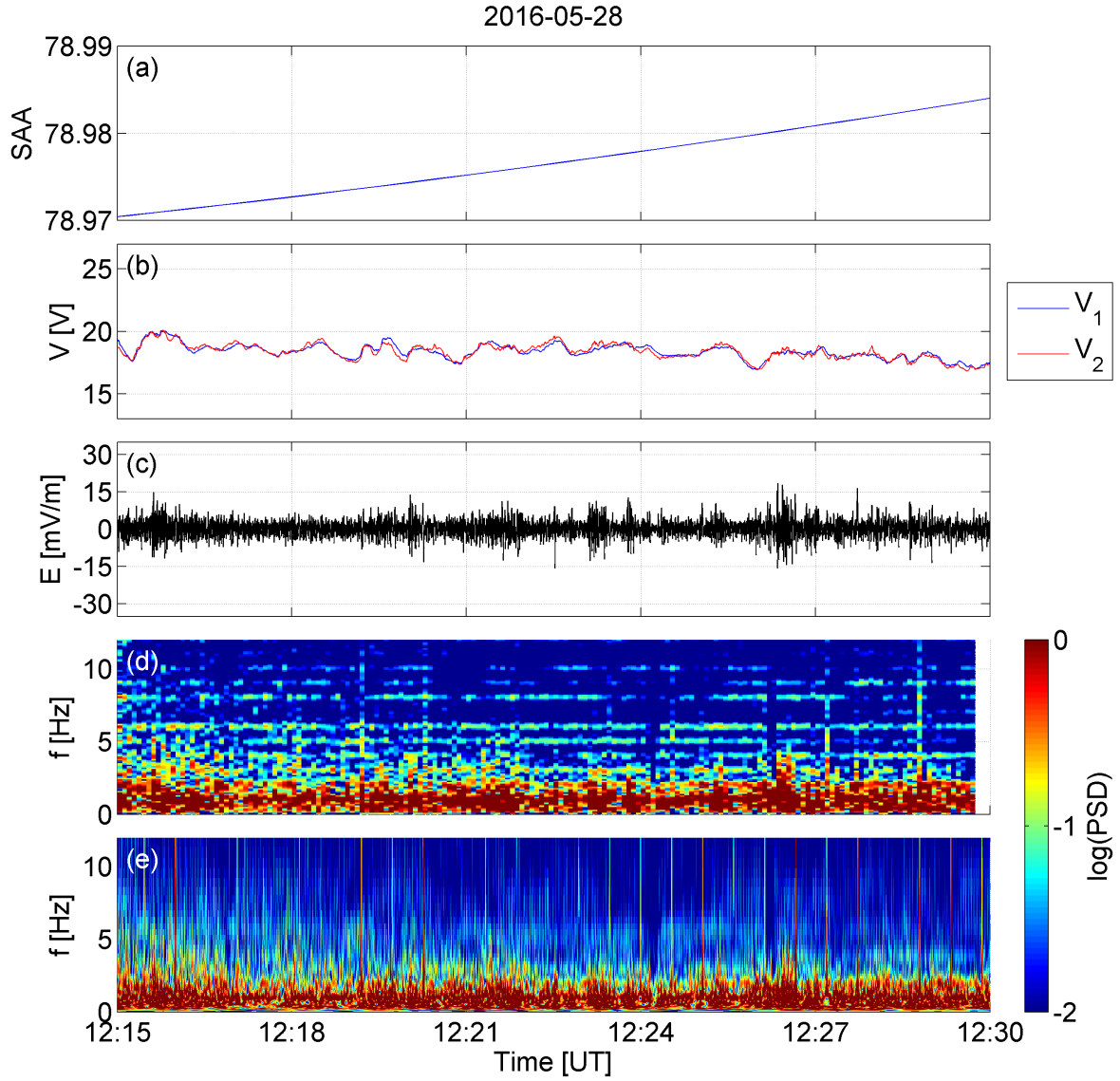


Figure F.2. (a) Solar aspect angle (SAA), (b) calibrated probe potential, (c) detrended electric field, (d) Fourier spectrogram and (e) Morlet wavelet spectrogram for a time interval from 12:15 UT to 12:30 UT on May 28, 2016, when horizontal lines appear in the spectrograms.